Hypersonic Nonequilibrium Flow over An Ablating Teflon Surface

by

Dong Joo Song

Dissertation submitted to the Faculty of the

Virginia Polytechnic Institute and State University

in partial fulfillment of the requirements for the degree of

Doctor of Philosophy

in

Aerospace Engineering

APPROVED:

C. H. Lewis, Chairman

J. A. Schetz

A. K. Jakubowski

W. L. Neu

D. T. Mook

May, 1986

Blacksburg, Virginia

Hypersonic Nonequilibrium Flow over An Ablating Teflon Surface

by

Dong Joo Song

C. H. Lewis, Chairman

Aerospace Engineering

(ABSTRACT)

A complex chemical system of teflon/air mixture over an axisymmetric decoy at hypersonic reentry flight conditions has been analyzed by using the nonequilibrium viscous shock-layer method. The equilibrium catalytic wall boundary condition was used to obtain the species concentration at the wall. The species conservation equation for binary mixture (air/teflon) was solved to obtain the concentration of freestream air at the wall. Two test cases were chosen to demonstrate the capability of the current code. Due to lack of experimental or theoretical data, the surface-measurable quantities from the current code(VSLTEF) were compared with the equivalent air injection and no-mass injection data obtained from VSL7S code. The current code predicts a higher total heat-transfer rate than that predicted by the seven species nonequilibrium air code (VSL7S) with the same injection rate due to the high diffusional heat-transfer rate. The wall pressure was not affected by blowing, while the skin-friction coefficient was decreased (i.e., 43 % reduction for teflon ablation case ; 53 % for nonequilibrium air injection case at 125 kft) when compared with that of no-mass injection case. A shock-layer peak temperature drop ($1512°R$ for 125 kft altitude and $848°R$ for 175 kft altitude) was observed at both cases. The temperature drops were chiefly due to endothermic reactions (dissociation) of the teflon ablation species. Due to large blowing of teflon, the average molecular weight increased substantially and resulted in a reduction of the specific heat ratio γ and an increase in the Prandtl number at the wall. The impurity of sodium was the major source of free electrons near the wall at the end of the vehicle at 125 kft altitude; however, at 175 kft altitude NO^+ was the major source of free electrons over the entire body. The peak concentration of Na^+ increased along the body, but that of NO^+ decreased at both altitudes. While the chemical reaction rate data used is believed to be the best currently available, uncertainties in

this data as were cited by Cresswell et al.(1967) may lead to quantitative changes in the above teflon ablation results.

Acknowledgements

The author wishes to thank Dr. C. H. Lewis who served as the chairman of his advisory committee and who guided this research effort through technical advice and support.

The author also wishes to thank Dr. J. A. Schetz, Dr. A. K. Jakubowski, Dr. D. T. Mook and Dr. W. L. Neu for serving on the advisory committee and for their helpful comments and suggestions on this thesis.

Special thanks are given to the author's wife for her patience and moral support throughout this research work. The support from the author's family was vital to this research work.

Table of Contents

List of Illustrations

List of Tables

Nomenclature

$A_0 - A_5$ .....coefficients of partial differential equations

$\bar{A}_j, \bar{B}_j, \bar{C}_j, \bar{D}_j$ .....coefficients of a finite-difference equation

CA .....axial force coefficient

CFS .....skin-friction coefficient in the streamwise direction

CH .....film coefficient, $q_c/(H_r - h_w)$, $lbm/ft^2/$ sec

CI .....denotes C_i

C_i .....concentration of species i, ρ_i/ρ

Cp .....constant pressure specific heat

Cv .....constant volume specific heat

D_{ij} .....diffusion coefficient

E_j, F_j .....coefficients of the solution

E-/CC .....electron number density per cubic centimeter

ECW .....equilibrium catalytic wall

FCW .....fully catalytic wall

H .....stagnation enthalpy , H^*/U^2_{inf}

h .....Planck's constant, 6.625×10^{-34} $J.sec$

h_1, h_2, h_3 .....shape factors for a general orthogonal coordinate system

H_r .....recovery enthalpy, Btu/lbm

J_i .....diffusion mass flux term , $\frac{\mu \mathrm{Le}}{\mathrm{Pr}} \frac{\partial C_i}{\partial \eta}$

k .....thermal conductivity

L .....total axial length of body

Le .....Lewis number, $\rho C p D_{ij}/k$

k_b, k_f .....backward and forward reaction rate constants

k_c .....equilibrium reaction constant

$\dot{m}$ .....mass-transfer rate, $(\rho v)_w/(\rho U)_\infty$

M_i ..... molecular weight of specie i

$\overline{M}$ .....mixture molecular weight

$\bar{N}$ .....Avogadro number

NCW .....noncatalytic wall

NEQ .....finite rate nonequilibrium chemical reactions

NJ .....number of species plus catalytic third bodies, NS + NZ

NR .....number of chemical reactions

NS .....number of species

NSH .....shock standoff distance, n_{sh}

PINF .....freestream pressure, P_∞

PW .....wall pressure

p .....pressure, $p^*/\rho_\infty U_\infty^2$

q_c .....convective heat flux, $Btu/ft^2 - \sec$

q_w .....heat-transfer rate at the wall

R .....gas constant, $ft^2/\sec^2 - R$

R_u.....universal gas constant, $ft^2/\sec^2 - R$

Re .....Reynolds number

Rn* .....nose radius, ft

RN .....denotes Rn*

SP .....denotes species

s/Rn .....nondimensionalized streamwise distance by Rn*

s, n, φ.....nondimensional surface-normal coordinate system

T .....temperature, T^*/T^*_{ref}

T_{ref} ..... U^2_∞/Cp

U_∞ .....freestream velocity, ft/sec

u,v,w .....velocity components

or, u, v, w

W .....dependent variables $\bar{u}$, v, T, $\bar{p}$, C_i, etc.

x, X .....axial length

X_r .....effectiveness of reaction r in producing certain chemical species $= L_{fr} - L_{br}$

y/Rn .....nondimensional distance normal to body

α .....angle of attack, deg

α_{ri}, β_{ri} .....stoichiometric coefficients of reaction r

γ.....specific heat ratio, $\frac{Cp}{Cv}$

γ_i .....molar concentration of species i, $\frac{C_i}{M_i}$

δ .....boundary layer thickness

ε .....Reynolds number parameter, $(\rho_{ref} U_\infty Rn/\mu)^*\frac{1}{2}$; potential energy

μ .....viscosity , μ^*/μ^*_{ref}

ν .....wave frequency

ξ, η, ζ .....normalized surface-normal coordinates

ρ .....density, ρ^*/ρ^*_{ref}

σ .....mean diameter of non-reacting rigid spheres

τ .....skin friction force

$\psi(r)$ .....potential energy of interaction

Ω_v .....collisional cross-section

Superscripts

$()^*$ .....dimensional variable

$\overline{()}$ .....normalized variable

$\hat{(\,)}$ .....tabulated value

Subscripts

e .....boundary-layer edge conditions

eq .....equilibrium conditions

i .....species i

ref .....dimensional reference conditions

sh .....shock conditions

w .....wall conditions

∞ .....dimensional freestream conditions

o .....stagnation conditions

1.0 INTRODUCTION

While supersonic and hypersonic flows over blunt bodies have been of interest in fluid dynamics for many years, recent developments in aerodynamics and space flight have generated significant renewed interest in nonequilibrium viscous flowfield analyses of blunt multiconic reentry vehicles. A major motivation for this study has been the recent interest in decoy vehicles which use low temperature ablators as a thermal protection system from moderate to high altitude up to high angles of attack (approaching 35 degrees). At such altitudes, the characteristic reaction time is much longer than the characteristic flow time, and the vehicle is in the chemical nonequilibrium flow regime for most of its flight time. A critical element of the design analysis of decoy vehicles is the prediction of aerodynamic and aerothermodynamic performance. In addition to such decoy applications, the presence of ionized species in the shock layer has a significant impact on the transmission of electromagnetic signals to and from a reentry vehicle. The temperatures encountered during reentry are very high and cause a significant amount of ionization and dissociation of the air molecules within the shock layer.

Furthermore, low temperature ablators such as teflon and hydrocarbon compounds decompose and dissociate into many complex chemical species. Complex surface heterogeneous reactions occur simultaneously with dissociation. Also, the impurity of alkali materials existing in ablation materials can cause a significant source of electrons in the shock layer. The shock-layer properties

directly influence the gas chemistry in the wake, which in turn has an important bearing on the detection of a reentry vehicle. These requirements, and more, necessitate the development of the capability of a three-dimensional nonequilibrium flowfield analysis for multiconic reentry vehicles with surface ablation.

Hypersonic reentry flows are, in general, characterized by low Reynolds numbers. Due to such typically low Reynolds number flows, the application of boundary-layer methods has encountered significant difficulties (such as displacement-thickness interaction, streamline tracking, determination of edge conditions, etc.). The nonequilibrium laminar boundary-layer analysis method of Blottner et al.(1971) is a particular example of such solution methods. The viscous shock-layer (VSL) methods, on the other hand, have shown great potential for analyzing such nonequilibrium viscous reentry flows.

The perfect gas VSL equations were originally derived from the full Navier-Stokes equations by Davis(1970a). The VSL equations were subsequently modified by Davis (1970b) to include a chemically reacting binary gas mixture. Moss(1971) further extended the VSL scheme to study a five species (O, O_2, N, N_2, and NO) gas model. However, these studies were restricted only to analytic bodies such as hyperboloids. Miner and Lewis(1975) extended the VSL scheme to study the axisymmetric flow around non-analytic (sphere-cones) reentry vehicles using the seven species (O, O_2, N, N_2, NO, NO^+, and e^-) model of Blottner et al.(1971).

Swaminathan et al.(1983a) extended the axisymmetric VSL equations, for a seven-species reacting gas mixture, to study the three-dimensional nonequilibrium viscous flows around multiconic reentry vehicles. They used a body-normal coordinate system (as shown in Fig. 1) and also coupled the solutions of the first-order continuity equation and the first-order normal momentum equation, resulting in increased stability of the VSL solution scheme(Waskiewicz, 1978). The subsequent work of Swaminathan et al.(1983b, 1984) involved an extension of their earlier work to study the effects of wall and/or shock-slip, fully-catalytic wall conditions, noncatalytic wall conditions, and an eleven species gas model.

Kim et al.(1983) extended the nonequilibrium VSL solution scheme to include a non-orthogonal coordinate system and studied the flowfield around the space shuttle orbitor. Their

studies focused attention on the three-dimensional nature of the actual flowfield, as opposed to the "equivalent axisymmetric body method." Investigators have also studied and shown that (depending upon the flight altitude) the finite-catalytic wall boundary conditions can significantly influence the wall heat transfer(Kim, 1983). The nonequilibrium VSL solution schemes noted are applicable for conditions where the surrounding fluid consists of a reacting, ionizing and dissociating mixture of air species.

In earlier work Leibowitz(1973) and Tiwari and Szema (1979) used a two-temperature model for hydrogen-helium mixtures, and found that the electron temperature was much lower than the heavy particle temperature in the region near the shock. Recently, Swaminathan et al.(1984) further extended the nonequilibrium VSL solution scheme to include a two-temperature model for the electrons and heavier gas particles. Due to the difference in mass, the energy transfer during the electron and heavy particle collision was much slower than the energy transfer during the electron-electron collision. Consequently, a different temperature was assigned to the heavier particles and electrons separately. However, during hypersonic reentry applications and for AOTV applications, the shock-layer temperature is very high and produces a significant amount of surface heating. This in turn can result in appreciable ablation of the surface material. When an ablator is used to protect the surface of a vehicle from a high temperature environment, gaseous species are injected into the flowfield as the ablator is thermally degraded. If the ablation products are in significant amounts, the gas chemistry in the shock layer can also be affected. Especially because of the different specific heats of the ablation products and their subsequent reactions with the surrounding gas species, the shock-layer temperature distribution can be quite different. Variations occur in the shock-layer heat transfer, the gas chemistry, the ionization and dissociation levels of the surrounding gases, electron concentration profiles, etc.

For many reasons carbon (graphite) is one of the most common thermal protection materials used especially in the nose region of conventional reentry vehicles. The two important ablation products from graphites, with moderate surface temperature at high altitudes and/or at conditions where ablation is due to chemical reactions between the carbon surface and the environmental gases(i.e., oxidation reactions), are carbon monoxide (CO) and carbon dioxide (CO_2). However,

at lower altitudes, where heating is more severe, carbon ablation is due to sublimation and prominent ablation products are carbon vapor speciesC_1, C_2, C_3, C_4,C_5, etc.. Scala and Gilbert(1963) studied the hypersonic laminar stagnation heat transfer in gas mixtures with varying proportions of CO_2 and CO , using a boundary-layer approach. Their study shows that depending upon the enthalpy content, these ablation products had an appreciable affect on the local temperature distribution. Although their study concentrated on the wake properties, the qualitative aspect of their results can also be applied to the shock-layer flow.

Song and Lewis(1986) applied the nonequilibrium chemically reacting Viscous Shock-Layer method to hypersonic flow over an ablating carbon surface. A semi-empirical ablation model based on the quasi-equilibrium one-dimensional steady heat transfer analysis of Hecht and Nestler (1978) was used in their study. They used an equilibrium catalytic wall condition, which was obtained from Gibbs free-energy minimization technique of Gordon and McBride (1976). A significant shock-layer temperature drop (over 600 K) was observed when compared with nonequilibrium air injection cases. However, they observed higher stagnation heat-transfer rate when compared with equivalent nonequilibrium air injection, which was chiefly due to the large specific heat and enthalpy of the C, CO, and CO_2.

During hypersonic reentry flight, heated and ionized wake trails may be observed from the ground by radar and optical detection systems. The electrical properties of the flowfield surrounding the vehicle chiefly generated by the low temperature ablator and nonequilibrium air can have appreciable impact on the detection of a reentry vehicle. Epoxy resins and teflon are the most commonly used materials except for the nose region which is usually carbon-carbon. The epoxy resins are hydrocarbon polymers, which in the process of degradation and oxidation(combustion) in the air system, can supply free electrons to the flow by chemi-ionization(Cresswell et al., 1967). Teflon, a flourocarbon polymer, degradates and decomposes to yield a considerable concentration of flourine atoms and molecules in the boundary layer and wake. These flourine atoms and molecules can react with free electrons to form negative flourine ions, thereby reducing the electron density in the flowfield(Cresswell et al.,1967).

In the present study, teflon has been analyzed by using a finite rate chemically reacting viscous shock-layer method.

As discussed earlier, the presence of CO and CO_2 ablation products can have an appreciable impact on the shock-layer temperature distribution. Thus for the teflon/air system, the results from the current analysis should be qualitatively similar to carbon/air system.

Cresswell et al.(1967) discussed the effects of ablation products on hypersonic boundary layers and wakes behind the conical vehicle. They extensively discussed the effects of ablation products of teflon and hydrocarbon compounds on the species concentration profile, electron density profile and its decay in the wake. Also the effect of sodium contamination on the electron density was investigated, and they showed that a major source of electrons comes from the sodium and not from the nonequilibrium NO^+. The non-catalytic wall condition used by Cresswell et al. (1967) assumed that pure C_2F_4 was injected at the wall. Even though they concentrated on the turbulent wake far from the body, the qualitative result can be the same in the boundary layer.

Catalytic wall boundary conditions were examined by Braun (1973) , in which he used equilibrium catalytic wall boundary conditions by solving element continuity equations and equilibrium constant equations. At a given local wall pressure, temperature and element compositions, he obtained the individual species composition by residual relaxation method. Due to different catalytic wall boundary conditions, major species in the boundary layer are quite different, which eventually results in a large difference in temperature, heat transfer and species concentrations.

The investigations by Cresswell et al.(1967) and Braun (1973) were limited to axisymmetric boundary-layer flow only, and thus their application was restricted to zero lift. Moreover, accurate determination of the edge boundary conditions (particularly for chemical species) was quite difficult.

Thus more powerful methods such as VSL and/or Parabolized Navier-Stokes (PNS) techniques must be used to obtain more general treatments of realistic reentry flowfields over ablating surface materials. Since the solution method of VSL is by iteration at each and every station until convergence is obtained and then marching to the next station with substantially less computing time than when using the full Navier- Stokes method, the VSL method will be used to obtain the solution over the nose region where the local Mach number is less than one as well as the solution

far downstream in the supersonic/hypersonic flow region. VSL can also provide the initial plane data to other marching methods such as the Parabolized Navier-Stokes method(Bhutta and Lewis,1985).

In Chapter II an analysis of the nonequilibrium viscous shock-layer method is given, describing the extensions to include the effects of teflon ablation on the thermochemistry of the VSL prediction technique. Various boundary conditions for species and flowfield variables are also discussed in Chapter II. Results and discussion of the effects of ablating teflon surfaces are presented in Chapter III. Conclusions of the study and future recommendations are given in Chapter IV and V, respectively. The derivations of boundary conditions with mass transfer, transport property calculations, mass-transfer distribution, and production terms in the species and energy equations are presented in Appendixes A, B, C, and D, respectively.

2.0 ANALYSIS

In this paper, we will analyze nonequilibrium viscous flows around seven-degree half-angle sphere-cone reentry vehicles with teflon (C_2F_4) ablation into the air mixture. A sphere-cone vehicle at zero angle of attack is studied under two different flight conditions. The first set of conditions corresponds to a flight altitude of 125 kft and velocity of 22400 ft/sec, whereas the second set of conditions corresponds to an altitude of 175 kft and a freestream velocity of 22400 ft/sec. The freestream conditions are given in Table 1.

The governing equations are derived from the steady Navier-Stokes equations for a reacting gas mixture as given by Bird et al.(1960), and they have been written in surface-normal coordinates (refer to Fig. 1). The s-coordinate is tangent to the body in the streamwise direction, n-coordinate is normal to the surface, and the φ- coordinate is the angle around the body measured from the windward streamline. The equations are first nondimensionalized by variables of order one at the body surface and then again normalized by variables of order one in the outer shock region. The VSL equations are consequently obtained by neglecting terms higher than second order (ε^2). Therefore, these equations are uniformly second-order accurate from the body to the shock. The viscous shock-layer equations are parabolic in the crossflow direction as well as in the streamwise direction.

The governing equations and the final form of viscous shock-layer equations for finite-rate chemically reacting viscous flows can be found from Song(1984). To enhance numerical stability, it is helpful to rewrite the rate of production term so that the species concentration appears as one of the unknowns for the species conservation equation, and the temperature appears as an unknown in the energy equation as shown in Appendix D. The detailed derivation of VSL equations for a chemically reacting air mixture was given by Swaminathan et al.(1983).

2.1 Solution Procedure

In the normalized surface-normal coordinate system, the equations are written in the standard parabolic form:

$$A_0\frac{\partial^2 W}{\partial \eta^2} + A_1\frac{\partial W}{\partial \eta} + A_2 W + A_3 + A_4\frac{\partial W}{\partial \xi} + A_5\frac{\partial W}{\partial \zeta} = 0 \qquad (1)$$

where W is the dependent variable.

The finite-difference algorithm used to solve the ξ -momentum, ζ-momentum, energy, and species equations is the tridiagonal solver as used by Murray and Lewis(1975). The continuity and normal momentum equations were coupled together by Waskiewicz (1978) to considerably enhance the overall numerical stability characteristics of the scheme. Before the coupling, the VSL scheme could not obtain the solution over a non-analytic blunt body.

The solution begins on the spherically blunted nose by obtaining an axisymmetric solution in the wind-fixed coordinate system. The axisymmetric solution is rotated into the body-fixed coordinates and is used as an initial data profile for the three-dimensional solution. As the VSL scheme is parabolic in the cross-flow direction, at each marching station the three-dimensional solution

begins in the windward plane and marches around the body to obtain the converged solution at each ζ-step. After completing the ζ -sweep at a ξ-station, the solution is stepped downstream to solve the next ξ-station, with ζ -sweep. However, due to the parabolic nature of VSL equations, one cannot obtain the solution at the point where cross-flow separation begins or in the cross-flow separated region as well as in the axial flow separated region.

The equations are solved for an axisymmetric case in the following sequence:

1. boundary condition for species equation (C_{i_w})

2. 19 species conservation equations (C_i),

3. energy (T),

4. ξ-momentum ($\overline{u}$),

5. integration of continuity equation for n_{sh},

6. the coupled normal momentum and continuity ($\overline{P}$ and v).

Figure 2 shows the flow diagram of the axisymmetric VSL method. The current axisymmetric VSL code can be easily extended to incorporate a three-dimensional capability by including the ζ − momentum equation. The shock-layer equations depend on the shock slope $\frac{\partial n_{sh}}{\partial \xi}$ and normal velocity gradient along the streamwise direction $\frac{\partial v}{\partial \xi}$, which introduce an elliptic effect into the equations. In the present code the shock slope ($\frac{\partial n_{sh}}{\partial \xi}$) is provided by an inviscid code externally, and the values of $\frac{\partial v}{\partial \xi}$ are calculated from a backward-difference formula.

Since a body-oriented orthogonal coordinate is used in this study, the geometry discontinuities must be treated separately. The forebody is treated as a sphere-cone and afterbody is treated separately with the initial data-plane profile obtained from the forebody. At an expansion corner, the solution procedure is marched on to an extension of the upstream geometry past the expansion discontinuity for a streamwise length of 0.6 nose radii. Then the profiles at these two station are

interpolated in a plane normal to the downstream conical surface to obtain the initial data-plane for marching downstream. The flow velocity components are then rotated through the expansion angle. At a compression corner, the solution procedure is marched up to the discontinuity. The profiles at the last two stations including the discontinuity point are used to compute the initial data-plane profiles for the downstream flowfield. The solutions are iterated until the largest error falls within acceptable limits.

2.2 *Boundary Conditions*

At the wall, the no-slip boundary conditions are used. The surface velocity conditions are

$$u = w = 0, \tag{2}$$

The mass injection rates $\dot{m}$ are given as an input, and the normal velocity at the wall can be obtained from the following expression

$$\frac{(\rho v)_w}{(\rho u)_\infty} \equiv \dot{m} \tag{3}$$

Thus $v_w = \frac{(\rho u)_\infty \dot{m}}{\rho_w}$. Since density at the wall ρ_w is not known a priori, the normal velocity at the wall initially must be assumed as an arbitrary value and be iterated until the value of ρ_w becomes converged. For the energy equation, the temperature boundary condition can be written as

$$T = T_w \tag{4}$$

where T_w is either a constant or a specified temperature variation. In this analysis, T_w has been fixed at $1800°R$.

Rankine-Hugoniot jump conditions were used to obtain the properties behind the shock. The normal and tangential components of the velocity were calculated by using the method of Rakich (1969).

The wall-slip, shock-slip and temperature jump boundary conditions at the wall for a rarefied gas flow were not considered in the present calculation.

Boundary condition for pressure at the wall P_w is obtained from the normal momentum equation. After nondimensionalizing and normalizing by the shock value, the normal pressure gradient can be expressed as follows

$$\left(\frac{\partial P}{\partial \eta}\right)_w = -\frac{\rho_{sh} u_{sh} n_{sh} \bar{\rho}\bar{u}}{P_{sh}} \frac{\partial v}{\partial \xi} - \frac{\rho_{sh}\bar{\rho}\bar{v}}{P_{sh}} \frac{\partial v}{\partial \eta} \tag{5}$$

$$- \frac{\rho_{sh} n_{sh} \bar{\rho}\bar{w}}{P_{sh} h_3} \frac{\partial v}{\partial \zeta} + \frac{\rho_{sh}\bar{\rho}}{P_{sh}} \left(u_{sh}^2 \bar{u}^2 \frac{\partial h_1}{\partial \eta} + \frac{\bar{w}^2}{h_3} \frac{\partial h_3}{\partial \eta}\right)$$

The normal pressure gradient $(\frac{\partial P}{\partial \eta})$ is provided into the coupled normal momentum and continuity equation as a boundary condition for pressure .

In the present study the effects of radiation from the hot surface to the gas and from the hot gas to the surface have been neglected. The heat of vaporization of the surface material also has been neglected. We assumed that teflon (C_2F_4) was completely burned at the wall, and produced CF_4, CF_2, COF_2, F, CO_2, CO, etc., even though teflon-air mixtures are finite-rate chemically reacting throughout the shock layer. Since we are dealing with gas-phase reactions at the wall, the effects of surface reactions (such as endothermic reactions) are not included in the present study.

However, it is entirely possible that practical problems arise in which both exothermic(combustion) and endothermic (dissociation) chemical reactions occur at the interface between the gas-layer species and the undersurface material over which the gas flows (burning at the interface). The undersurface can melt and vaporize at the interface with consequent mass-transfer effects, and heat can be conducted into the solid-state interior. The species boundary conditions are discussed in a later section.

2.3 *Wall Temperature and Mass Injection Rate*

Ablating mass transfer from the body surface occurs for most reentry-type vehicles in passive heat shield protection applications. Energy balancing at the surface can be used to obtain the surface mass-transfer rates and wall temperatures by correlating theoretical and experimental results for the blowing parameter (B') with the heat-transfer coefficient (C_H) . The quasi-equilibrium $\dot{m}_T$ and T_w for a carbon surface have been calculated with the code developed by Thompson (1983). The empirical and theoretical basis for mass-transfer models used in a previous study for carbon ablation by Song and Lewis (1986) was presented by Hecht and Nestler (1978) who used a three-dimensional integral boundary-layer method for the steady-state calculation of ablation.

The surface ablation model for teflon is empirical, and based on the heat of ablation concept given by Brant (1970) in the form

$$\dot{m}_T = \frac{C_{H_0}}{0.04594 - 0.0027P_e} \tag{6}$$

where the ablation temperature is set to $1800°R$ and units of P_e are in atmospheres. A detailed derivation to obtain C_{H_0} and $\dot{m}_T$ can be found in Appendix C.

Figure 3 shows the $\dot{m}_T$ distribution along the sphere-cone geometry. Over the cone region around s/Rn = 4 to 6 the procedure predicts approximately 0.4% mass injection rate and $1800°R$ for the 175 kft altitude case, and 0.17% mass-transfer rate at 1800 R for the 125 kft case.

2.4 *Catalytic Surface Condition*

The chemical kinetics of heterogeneous catalytic reactions are exceedingly complicated, and our knowledge of the details of the phenomena is inadequate. So usually the wall is assumed to be non-catalytic or fully catalytic, which gives the two extreme conditions for the species wall boundary conditions.

For a non-catalytic wall, the mass fluxes of all the species $\dot{m}_i$ are zero. The clear definition of a fully catalytic wall is not quite clearly given in the literature but can be such that every dissociated and ionized species that strikes the surface is converted into a molecular species due to heterogeneous reaction. For a low temperature wall, the above definition of a fully catalytic wall is nearly the same as that when the gas is undissociated or the gas composition corresponds to the equilibrium value at the surface temperature. But for a higher wall temperature, the equilibrium composition might be quite different from a fully catalytic wall (Song and Lewis, 1986).

The fully catalytic wall boundary conditions for nonequilibrium air species (VSL7S code) including the nonequilibrium air injection case can be expressed as follows,

$$C_{O_2} = 0.23456,\ C_{N_2} = 0.76544 \tag{7}$$

$$C_N = C_{NO^+} = C_O = C_{NO} = 0.0$$

For the equilibrium catalytic wall,

$$C_i = C_{i_{eq}}(T_w) \tag{8}$$

In the present study $C_{i_{eq}}$ have been obtained from the Gibbs free energy(G = H-TS) minimization technique and were provided as input data from the code developed by Gordon and McBride (1976) at a given wall pressure and weight ratio of teflon to total teflon/air mixture.

For the equilibrium wall species boundary condition there can be two approaches, one is by using the equilibrium constant method and the other is Gibbs free-energy minimization technique.

Braun (1973) used the former approach to obtain the equilibrium wall species. However, in the present study, the latter method used by Gordon and McBride (1976) is adopted. To use the latter method, we need percent teflon weight ratio to total mixture at a given temperature and pressure. The freestream species concept has been used to obtain the wall freestream species concentration. Baron (1960) and Mayne et al. (1969) discussed this method somewhat in detail.

As discussed by Baron, the net mass flux of the freestream species (nonequilibrium air) should be zero at the porous body surface rather than the false boundary condition that the concentration of the freestream species should be zero as Jaffe et al.(1967) used. Figure 4a shows the schematic drawing of the surface mass-flux phenomena. By solving the binary mixture species conservation equation for nonequilibrium air as one specie with the above boundary conditions, i.e., Eq. (A.1), we could obtain the wall freestream species concentration. By using freestream species concentration and P_w, we can use the Gibbs free-energy minimization technique of Gordon and McBride (1976) to find the equilibrium species concentration. The detailed derivation of binary mixture boundary conditions for the species conservation equations in a body-normal coordinate system can be found in Appendix A.

The table of equilibrium species was provided into the code calculated from the Gordon and McBride code for different teflon/air weight ratio and P_w. Second-order Lagrangian interpolation was used consecutively two times to obtain the equilibrium wall species concentrations for different weight ratios of teflon to total mixture, at varying pressures and at a temperature of $1800°R$

The equilibrium wall species concentration vs. teflon to total mixture weight ratio at pressures 0.001, 0.1, and 10 lbf/in^2 are shown in Figs. 5, 6 and 7. Figures 8, 9 and 10 show the equilibrium wall species concentration vs. pressure (lbf/in^2) at different fuel weight ratios, 0.1 %, 10 % and 30 % respectively.

The amount of sodium impurity in the ablated species was important, because sodium can be a significant source of free electrons as discussed by Cresswell et al. (1967). The concentration of sodium used in this study was 1.33×10^{-4} of $C_{C_2F_4}$ at the wall, which was obtained from the binary species conservation equation for air (refer to Appendix A). The above value was used by Cresswell et al. (1967) and Braun (1973).

The noncatalytic wall conditions are written as

$$\left(\frac{\partial C_i}{\partial \eta}\right)_w = 0 \tag{9}$$

Cresswell et al. (1967) specified all of the wall ablation species as C_2F_4.

For the boundary conditions of an ablating teflon surface in this study, only the equilibrium catalytic wall conditions have been used.

2.5 Species Considered

It is assumed that the chemical reactions proceed at a finite rate, and the rate of production $\dot{w}_i$ of the individual species is needed. For the present study, 21 species ($O, O_2, NO, N, NO^+, C, CO, CO_2, Na, Na^+, O^-, O_2^-, CF_4, CF_2, F_2, F, F^-, COF_2, C_2F_4, N_2$ and e^-) and 28 reaction rate equations were chosen to represent the flowfield over ablating carbon surfaces.

The chemistry of C_2F_4 oxidation and degradation is still speculative at this time. The possible outcomes from the elemental system F/C/O/N may introduce many species for consideration (Browne, 1965) due to degradation, combustion, and ionization. Degradation in high temperature air generates monomeric C_2F_4 as well as fragments such as C_2F_2, CF_4, CF_3, CF_2, CF, F_2, and$F$. Combustion of various fragments with air generates FO, FCN, COF_2, F_2O, FNO and intermediates FCO and FO_2. The ionization and electron attachment characteristics of the C_2F_4 /air system are of considerable interest. The high electron affinity of F, namely 3.448 ± 0.005 ev, conceivably may affect the free electron population in wakes as well as in boundary layer. Hence the species F^- is included in the present calculations. The ionization potentials of many of the flourine containing compounds are prohibitively high relative to ionization potential of the associative reaction of NO(2.76ev) in the air system; therefore, exclusion of ionized ablated species has been made.

The ionization potentials of $C_2F_4^+$, CF_3^+ are 9.3 and 8.6 ev, respectively. The ionization reaction of C_2F_4 and CF_3 are still not clear in the open literature. This can be further explained by the fact that the simple dissociation-recombination type of reaction

$$NO + M = NO^+ + e^- + M \quad (9.25ev)$$

is not the significant reaction which produces NO^+. In a noble gas such as Argon, this type of reaction with an electron serving as the catalytic third body M, is an important one (Petschek and Byron, 1957). For nitric oxide, however, because of its diatomic nature, the most important reaction is the associative reaction (Vincenti and Kruger, 1960)

$$N + O = NO^+ + e^- \quad (2.76ev).$$

The ionization potential of $C_2F_4^+$ *and* CF_3^+ is much higher than that of NO^+. Thus $C_2F_4^+$ *and* CF_3^+ have been eliminated from consideration. Also, C_2F_2, CF_3, CF, FO, FCN, F_2O, FNO, FCO and FO_2 have been omitted from consideration, since their molar concentrations at various equilibrium wall conditions have been far less than 0.5×10^{-5} and the reaction mechanisms were not known exactly.

To simulate the sodium contamination in the ablation products, Na and Na^+ were included in the calculation. The ionization potential of Na^+ is less than $NO^+(2.76ev)$, and a substantial part of the electron production may come from the ionization of the sodium.

As a whole, the exclusion of the aforementioned species has been made by consideration of the mole fractions of the neglected species at the equilibrium wall condition. Moreover, the species concentrations at the equilibrium wall condition were far less than 0.5×10^{-5}, and the reaction mechanisms are ambiguous at the present time in the open literature.

2.6 *Thermodynamic Properties*

The thermodynamic properties of the species O, O_2, NO, NO^+, N, N_2 and CO were obtained from the thermodynamic data of Browne (1962a, 1962b, 1962c). C and CO_2 data were obtained from Esch et al.(1970) and Gordon and McBride (1976) in the form of curve-fit relations. The curve-fit coefficients of C and CO_2 are tabulated in Table 2. However, due to lack of thermodynamic properties of CO_2 at very high temperatures (viz. above 10,000 K), we assumed a constant C_p above 10,000 K to calculate the enthalpy of CO_2. This is permitted because at a high temperature CO_2 is completely dissociated and has no contribution to either enthalpy or specific heat of the mixture.

The source of the other species over the full temperature range can be written as follows:

For Na, Na^+,

300 - 5000 K ; Curve fit equation from Gordon and McBride

5000 - 15000 K ; Tabulated data of Browne (1965).

15000 - 60000 K ; Assuming C_p constant, enthalpy was obtained from the Eq. (10).

For O^-,

100 - 15000 K ; From Gordon and McBride

15000 - 60000 K ; Same procedure as Na, Na^+

For $O_2^-, CF_2, CF_4, F, F_2, F^- \cdot C_2F_4, COF_2$,

100 - 15000 K ; From tabulated data of Browne (1965).

15000 - 60000 K ; Same procedure as Na, Na^+

The enthalpy of the individual species above 15000 K has been obtained by using the following expression by assuming the specific heat of the material is constant above 15000 K.

$$h_i(T) = \int_{T=15000}^{T} C_{p_i} dT + h_i(15000K) \tag{10}$$

Figures 11 and 12 shows the enthalpy of the nonequilibrium air/teflon species, $O, O_2, NO, N, NO^+, C, CO, CO_2$ and Na, and $Na^+, O^-, O_2^-, CF_4, CF_2, F_2, F, F^-, COF_2, C_2F_4$ and N_2, respectively.

In Figs. 13 and 14, the specific heat C_p of the nonequilibrium air/teflon species as shown in the enthalpy plots (Figs. 11 and 12) can be found, respectively.

A second-order Lagrangian interpolation was used to obtain the values of $\hat{H}_i$ and $\hat{C}_{p_i}$ from the tables. The species enthalpy and specific heat were obtained from the expressions

$$h_i = T\hat{H}_i + \Delta h_i^F \quad \left(\frac{ft^2}{\sec^2}\right) \tag{11}$$

and

$$C_{p_i} = \hat{C}_{p_i} \quad \left(\frac{ft^2}{\sec^2 - R}\right) \tag{12}$$

where Δh_i^F is the heat of formation of species i, which can be found in Table 3.

2.7 Transport Properties

The viscosity of each of the individual species was calculated from the curve-fit relation

$$\mu_i = e^{C_i T_k^{(A_i \ln T_k + B_i)}} \quad \left(\frac{gm}{cm - \sec}\right) \tag{13}$$

where A_i, B_i, and C_i are the curve-fit constants for the species i. The coefficients A_i, B_i and C_i for whole species are given in Table 4. The viscosity data of O, O_2, NO, N, NO^+ , and N_2 were obtained from Blottner (1970). The coefficients for C and CO were obtained from a different curve-fit relation

$$\mu = a_i + b_i T_k + c_i T_k^2 \quad (\frac{lbm}{ft - \sec}) \tag{14}$$

where a_i, b_i and c_i are curve-fit constants from Moss (1984) and are tabulated in Table 5.

From Svehla (1960) who used Lennard-Jones potential function (Fig. 15) the viscosity data of CO_2, Na, CF_2,CF_4, F, F_2,C_2F_4 were obtained from 300 - 5000 K. As discussed in Appendix B, by using the relation between collision cross-section and reduced temperature defined as $T^* = \frac{kT}{\varepsilon}$ we generated the viscosity data above 5000 K. The individual viscosity data of Na^+, F^-, O_2^-, O^- and COF_2 were obtained from Biolsi (1986). from 4000 K to 10000 K.

Transport properties for F^-,O_2^-, O^-, Na^+

The screened Coulomb potential has been used to calculate the transport collision integrals and properties for the ion-ion interaction. Since Coulomb interactions are strong long-range interactions, the usual first-order kinetic theory expressions for the transport properties are not satisfactory. Biolsi (1986) used the third approximation to obtain the transport properties of ionized species.

The COF_2 transport properties were calculated by using the peripheral force mode. The O-O and F-F interactions were taken from the work by Mason et al. (1970), and interactions involving C were ignored since the carbon atom is reasonably well " buried " in the molecule. The O-F interaction was obtained from a geometric mean of the O-O and F-F interactions. The atom-atom potential was orientation averaged, summed, and best fit with an exponential repulsive potential.

However, the data obtained from Biolsi were limited to a $4000°K - 10000°K$ temperature range. Thus, the lower temperature data for the ionized species have been extrapolated in the $In\, T(K)$ *vs.* $ln\, \mu\, (gm/cm/\sec)$ plane, and the curvefit constants were obtained by the quadratic

least-square method. The data above 10000°K were simply obtained from the above quadratic least squares curvefit. When we compare the known data such as CF_2, CF_4 etc.,the data behaved very similarly.

A viscosity data plot of O, O_2, NO, N, NO^+·C, CO, CO_2, and Na can be found in Fig. 16. And those of CF_4,CF_2,F_2, F, COF_2, C_2F_4 and N_2 can be seen in Fig. 17. Figure 18 shows the viscosity for ionized species Na^+, O^-, O_2^- and F^-. The quadratic least-square polynomial curve fit of $\ln \mu$ *vs.* $\ln T_k$ plots was used to obtain the same form used by Blottner (1970): The curve-fit constants are given in Table 4.

The thermal conductivity of the individual species was calculated from the Eucken semi-empirical formula using the species viscosity, molecular weight, and specific heat by the expression

$$k_i = \frac{\mu_i R}{M_i}\left(\frac{C_{p_i} M_i}{R} + \frac{5}{4}\right) \quad \left(\frac{lbf}{\sec R}\right) \tag{15}$$

After calculating the viscosities and conductivities of individual species, the viscosity and thermal conductivity of the mixture were calculated using Wilke's semi-empirical relations:

$$\mu = \sum_{i=1}^{NS} \left(\frac{X_i \mu_i}{\sum_{j=1}^{NS} X_i \varphi_{ij}}\right) \quad \left(\frac{lbf - \sec}{ft^2}\right) \tag{16}$$

$$k = \sum_{i=1}^{NS} \left(\frac{X_i k_i}{\sum_{j=1}^{NS} X_i \varphi_{ij}}\right) \quad \left(\frac{lbf}{\sec - R}\right) \tag{17}$$

where $X_i = C_i \frac{\overline{M}}{M_i}$, and

$$\varphi_{ij} = \left[1 + \left(\frac{\mu_i}{\mu_j}\right)^{\frac{1}{2}} \left(\frac{M_j}{M_i}\right)^{\frac{1}{4}}\right]^2 \times \left[\sqrt{8}\left(1 + \frac{M_i}{M_j}\right)^{\frac{1}{2}}\right]^{-1}$$

The diffusion model used in the present study is a limited binary diffusion model with binary diffusion coefficients specified by the Lewis number

$$\mathrm{Le} = \frac{\rho C_p D_{ij}}{k} = 1.4 \tag{18}$$

2.8 *Chemical System for Teflon and Air Mixture*

2.8.1 Chemical Reaction Model

It is assumed that the chemical reactions proceed at a finite rate, and the rate of production $\dot{w}_i$ of the individual species is necessary to solve the species conservation equations. For the present study, 21 species ($O, O_2, NO, N, NO^+, C, CO, CO_2, Na, Na^+, O^-, O_2^-, CF_4, CF_2, F_2, F, F^-, COF_2, C_2F_4, N_2$ and e^-) and 28 reaction equations were chosen to represent the flowfield over an ablating teflon surfaces. They are ,

$$O_2 + M_1 = O + O + M_1 \quad [1]$$

$$N_2 + M_2 = N + N + M_2 \quad [2]$$

$$N_2 + N = N + N + N \quad [3]$$

$$NO + M_3 = N + O + M_3 \quad [4]$$

$$O + NO = N + O_2 \quad [5]$$

$$O + N_2 = N + NO \quad [6]$$

$$O + N = NO^+ + e^- \quad [7]$$

$$N_2 + O_2 = NO + NO \quad [8]$$

$$CO + O + M_4 = CO_2 + M_4 \quad [9]$$

$$CO + M_5 = C + O + M_5 \quad [10]$$

$$CO + O = C + O + O \quad [11]$$

$$CO + O = CO_2 + h\nu \quad [12]$$

$$Na + O_2 = Na^+ + O_2^- \quad [13]$$

$$Na + O = Na^+ + O^- \quad [14]$$

$$Na + M_6 = Na^+ + e^- + M_6 \quad [15]$$

$$Na + e^- = Na^+ + e^- + e^- \quad [16]$$

$$Na^+ + e^- = Na \quad [17]$$

$$O + e^- + M_7 = O^- + M_7 \quad [18]$$

$$O_2 + e^- + M_7 = O_2^- + M_7 \quad [19]$$

$$C_2F_4 + M_6 = CF_2 + CF_2 + M_6 \quad [20]$$

$$C_2F_4 + O = COF_2 + CF_2 \quad [21]$$

$$CF_2 + O_2 = CO + F + F + O \quad [22]$$

$$CF_4 + M_6 = CF_2 + F + F + M_6 \quad [23]$$

$$COF_2 + M_6 = CO + F + F + M_6 \quad [24]$$

$$F_2 + M_6 = F + F + M_6 \quad [25]$$

$$F_2 + e^- = F + F^- \quad [26]$$

$$F^- + M_6 = F + e^- + M_6 \quad [27]$$

$$F + e^- \quad = \quad F^- + h\nu \qquad [28]$$

The whole reaction rate data and the catalytic third body efficiency matrix relative to Argon are given in Tables 6 and 8, respectively.

2.8.2 Nonequilibrium Air Reaction Equations

Reactions 1 through 7 correspond to the seven species model used by Blottner(1970), and Miner and Lewis (1975), and are based on the data proposed by Bortner (1963).

Reaction 8 is additional to the seven air species reactions, and this reaction was used by Cresswell et al. (1967) in their study of wake properties behind ablating vehicles.

The catalytic third body data for the nonequilibrium air species were chiefly obtained from Blottner (1970); however, part of the data (such as for teflon ablated species) were obtained from Cresswell et al. (1967).

2.8.3 Carbon Related Species Reactions

The reaction rate data for reaction 9 are based on the data recommended by Langen et al. (1965) who investigated the influences of the ablated species on wake ionization by using a nonequilibrium wake flowfield analysis.

Davies (1965) showed that the dissociation of CO_2 can be approximated through multi-step reactions. However, due to the difficulties in computer implementation and the various intermediate states of CO_2, the CO_2 dissociation mechanism is limited to a single step reaction as suggested by Langen et al.(1965).

The forward reaction-rate data for reactions 10 and 11 are based on the data recommended by Appleton et al. (1970); however, the backward reaction-rate constants are obtained from the equilibrium reaction constants given by Schofield (1973) as follows:

$$K_b = \frac{K_f}{K_c} \tag{19}$$

where K_c is the equilibrium reaction constant.

2.8.4 Sodium Related Species Reactions

Several factors that influence the ionization level of sodium include temperature, density and distance downstream from the stagnation point.

The dominant reaction which produces both sodium and electrons is the direct ionization reaction as used by Cresswell et al. (1967)(Reaction 15):

$$Na + M_6 \quad = \quad Na^+ + e^- + M_6$$

Two other reactions of lesser importance for producing Na^+ are reactions 12 and 14,

$$Na + O_2 \quad = \quad Na^+ + O_2^-$$

$$Na + O \quad = \quad Na^+ + O^-$$

The more important of these two is the first, because near the wall and near the shock a larger amount of molecular oxygen is available.

$$Na + O_2 \quad = \quad Na^+ + O_2^-$$

This reaction 13 is of some importance at higher altitudes and lesser important at the lower altitudes, because of burning the available O_2 supply near the peak temperature point. At the higher altitude, the temperature is virtually constant while at the lower altitude there is an appreciable temperature decrease.

2.8.5 Teflon Ablation Species Reactions

For low altitude cases, two endothermic reactions cause the temperature to drop. These two reactions are reactions (22) and (24), which were used by Cresswell et al. (1967).

$$CF_2 + O_2 \quad = \quad CO + F + F + O$$

$$COF_2 + M_6 \quad = \quad 2F + CO + M_6$$

The important reactions to be considered are the ion attachment to the flourine, which can be written in reaction 26 through 28 from Cresswell et al. (1967).

$$F_2 + e^- \quad = \quad F^- + F$$

$$F + e^- + M_6 \quad = \quad F^- + M_6$$

Data for reaction (20) were obtained from Modica and LaGraff (1965a), where they obtained the reaction rate constants by using the ultraviolet absorption and mass spectrometric observations of shocked 1 % C_2F_4 and 99 % Ar gas mixture between 1200 − 1800°K. A least squares fit to the experimental equilibrium constants using the integrated form of the van't Hoff equation is used as follows,

$$\log K_c = -\frac{69432.}{2.303RT} + 4.62 \qquad (K_c \text{ in moles/cc}) \tag{20}$$

Reaction rate data of reactions (22), (23), and (24) were obtained from Modica and LaGraff (1965b).

2.9 Chemical Reaction Parameters

A useful parameter to identify the relative importance of the various chemical reactions is the following :

$$X_r = \frac{\dot{w}_i}{[\rho M_i(\beta_{ri} - \alpha_{ri})]} = L_{f_r} - L_{b_r} \tag{21}$$

where the various quantities are defined in Appendix D. The above relation for X_r gives the effectiveness of reaction r in producing certain chemical species.

The production of species i from the various chemical reaction is obtained by multiplying X_r by $(\beta_{ri} - \alpha_{ri})$. The relative size of these terms determines which relations are important in the production of species i.

2.10 Electron Density

To obtain the electron number density from various chemical reactions, it is useful to determine the mass fraction of ionized species by the following relation:

$$N_e = \bar{\rho} N \gamma_{e^-} \tag{22}$$

where

$$\overline{\rho}(gm/cm^3) = 0.51536\rho(slug/ft^3)$$

$$\gamma_{e^-} = \sum_{j=1}^{NS} Z_j \gamma_j$$

The value of Z_j is determined from the linear dependence of the electrons on the NS chemical species and is based on charge conservation. When we notice the reactions (7), (13), (14), (15), (16) and (17), the presence of NO^+ and Na^+ will produce an equal molar amount of electron. However, as in reactions (18), (19), (26), (27) and (28), the electron is consumed the same molar amount as O^-, O_2^- and F^-. Thus

$$Z_{NO^+} = Z_{Na^+} = 1.0 \tag{23}$$

$$Z_{O^-} = Z_{O_2^-} = Z_{F^-} = -1.0$$

These values has been tabulated in the table of catalytic third body efficiency matrix relative to Argon.

2.11 *Surface Heat-Transfer Rate*

The surface heat transfer rate consists of three major phenomena, which are heat transfer due to conduction, heat transfer due to diffusion of species and heat transfer due to injection of mass with different enthalpy and specific heat into the boundary layer (Adams, 1970), where Dufour effect (usually considered small), and radiation are neglected. The heat-transfer due to radiation for AOTV application was reported to be less than 10 % of heat-transfer due to convection (see Scott

et al. 1984) at the stagnation point. Figure 4b is the schematic drawing which shows the contribution of various component of heat-transfer accompanying mass-transfer.

After nondimensionalizing by reference variables and normalizing by the shock values, we have the following expression

$$\begin{aligned} \dot{q}_{tot} &= \dot{q}_{\text{cond}} + \dot{q}_{\text{diffusion}} + \dot{q}_{\text{injection}} \\ &= -\varepsilon^2[\bar{k}k_{sh}\frac{\partial T}{\partial \eta}\frac{1}{n_{sh}} - \sum_{i=1}^{NS} J_i h_i]_w + \dot{m}\sum_{i=1}^{NS}[C_i h_i - C_{i\_} h_{i\_}]_w \end{aligned} \tag{24}$$

where

$$J_i = -\frac{\mu \text{Le}}{\text{Pr}}\frac{\partial C_i}{\partial \eta}$$

3.0 Results and Discussion

In order to predict the decoy flowfield, two test cases were chosen, and the freestream conditions for the altitudes of 125 kft and 175 kft are tabulated in Table 1.

The vehicle geometries of the 7-deg half-angle spherically blunted cone are shown in Fig. 19. Figure 19a shows the 7-deg cone vehicle with 5-ft slant length as used by Cresswell et al. (1967). Figures 19b and 19c show the spherically blunted cone with the same base diameter and a nose radius of 1 inch and 2 inches, respectively.

In this study, 7 deg sphere-cone with a one inch nose radius at 125 kft is referred to as case A, and with a two inch nose radius at 175 kft as case B. By using nondimensional length the total body length of vehicle A is 52.3 s/Rn, and that of vehicle B is 22.3 s/Rn. The inviscid shock shapes for the present calculations have been externally provided by the NOL3D code (Solomon et al., 1977). In order to enhance the accuracy of the nonequilibrium viscous shock-layer solution, a global iteration was performed by using the viscous output shock as an input.

Since little theoretical or experimental analysis has been performed for the low-temperature ablation materials in realistic reentry environment, no comparisons with any experimental or theoretical data were made in this study. However, data from the current analysis of teflon were compared with the data of the equivalent nonequilibrium air injection and no-mass injection cases.

Both nonequilibrium air calculations were made by using the seven species code (VSL7S) of Swaminathan et al. (1983a) with fully catalytic surface boundary conditions.

The results consist of three parts. The results of case A are discussed in part 1, and those of case B are discussed in part 2. Computing times for case A and case B were presented in part 3. The species profile and flowfield variables such as $\frac{u}{u_\infty}$, $\frac{v}{u_\infty}$, $\frac{\rho}{\rho_\infty}$, $T(R)$, $\frac{p}{p_\infty}$ were compared with the equivalent nonequilibrium air injection and the no-mass injection cases.

Also, the profiles of the average molecular weight ($\overline{M}$), Prandtl No. (Pr), and specific heat ratio (γ) were compared at two different locations, in terms of 7 deg. cone wetted length along the surface, at 2.28 ft and 5 ft or for case A, at s/Rn = 19.70 and 52.3 and for case B, at s/Rn = 6 and 22.3. The body end was specially chosen to provide accurate species concentration profiles to a wake analysis program.

3.1 Part 1

3.1.1 Freestream Species and Equilibrium Wall Species Concentrations

The results obtained from the binary species conservation equation (refer to Appendix A) is shown in Fig. 20 for case A. As discussed by Mayne et al. (1970), the freestream mass flux (or equivalently air) at the beginning of the injection is the major composition at the wall, but decreases gradually downstream. The freestream air concentration decreases from 0.9 at stagnation point to a value of 0.53 at the body end.

The equilibrium wall species concentrations were interpolated from the table obtained from Gordon and McBride (1976) with a three-point Lagrangian interpolation. Figures 21 and 22 show

the equilibrium wall species concentrations along the body. Since the concentration of teflon increases as it goes downstream, the concentrations of CF_4, COF_2, CO and Na increase accordingly; however, the concentrations of N_2, O_2, and NO decrease substantially.

At s/Rn = 21.7, O_2 disappears completely at the wall, because O_2 is depleted by the dissociation and oxidation reaction. C_{CO_2} increases to a peak value of 0.135 at s/Rn = 10 and then decreases gradually. The major species at the equilibrium wall in the region of interest (approximately s/Rn 10-52.3) are N_2, CF_4, COF_2, CO_2, and CO. The concentration of sodium is approximately 5×10^{-5}, and that of F is zero over the entire body for case A.

3.1.2 Nonequilibrium Air Species Profiles

Figure 23 shows the composition of the nonequilibrium air species (O, O_2, NO, N, N_2) profiles at s/Rn = 19.7 between the results obtained from the teflon code (VSLTEF) and those from the nonequilibrium seven species code (VSL7S). C_O and C_N increase from zero at the wall to a peak value at y/Rn = 0.24-0.36 where the temperature drops to a minimum (4460°R) between two temperature peaks (5360°R and 5142°R). (Hereafter we will call this minimum temperature point the saddle point.) Dissociation of O_2 and N_2 becomes maximum at the saddle point and consumes a lot of energy; thus, it leads to a big temperature drop to the minimum.

For the nonequilibrium seven species case, $C_{O_{2w}} = 0.23456$, and $C_{O_{2at\ saddle\ point}} = 0.11 \times 10^{-4}$. Thus, O_2 dissociates almost completely and N_2 dissociates to a minimum value at the saddle point. However, for the teflon case, N_2 monotonically increases from 0.42789 at the wall to 0.76544 at the shock, which is the opposite of the nonequilibrium seven species air case. An interesting difference in the NO profile is that for the nonequilibrium seven species case, C_{NO} reaches a peak near the wall and decreases to a minimum value near the saddle point and then reaches another maximum value and decreases to zero. However, NO for the teflon blowing case decreases near the wall and again increases to a peak at the same location as the nonequilibrium seven species cases.

Figure 24 shows the nonequilibrium air species concentration profile at s/Rn = 52.3. O, O_2, N and N_2 behave similarly with respect to the case at s/Rn = 19.7. The NO profile for the teflon case is different from that at s/Rn = 19.7 in that NO reaches a maximum from zero at the wall and decreases to zero at the shock.

3.1.3 Teflon Ablation Species Profiles

Figures 25 and 26 show the species concentration profiles of $C, CO, CO_2, Na, CF_4, CF_2, F_2, F$, and COF_2 at s/Rn = 19.7 and at 52.3 respectively. The major species at the wall are CF_4(0.3056), COF_2(0.11308), CO_2(0.0903), and N_2(0.4006); CF_4 and CO increase downstream; however, the concentration of CF_4, COF_2, and CO_2 monotonically decrease due to diffusion and convection the farther they go away from the wall.

$CF_2, F, C,$ and F_2 reach their maximum through the endothermic reactions near the wall where the local temperature reaches a maximum, $T = 5548°R$ at s/Rn = 19.7 and $6175°R$ at s/Rn = 52.3, and decrease monotonically to zero.

3.1.4 Electron Number Density

Figures 27 and 28 show the electrons number density profile at s/Rn = 19.7 and 52.3, respectively.

The peak electron number density stays at about $9.6 - 9.9 \times 10^{11}$ electrons/cm^3. However, there are qualitative differences between the two plots; that is, at the former location, the major electron density concentration comes from NO^+, but at s/Rn = 52.3, the majority of the electrons comes from Na^+ near the wall. Approximately 70 % of the free electrons come from Na^+. This

phenomenon can be clearly seen in Figs.29 and 30. Figure 29 shows that major ionized species throughout the shock-layer was NO^+ at s/Rn = 19.7. Na^+ reaches a maximum near the first peak temperature, but the concentration of Na^+ is one order of magnitude lower than that of NO^+ value and decreases rapidly. At s/Rn = 52.3, the major ionized species which produce free electrons is Na^+, not NO^+.

The concentration of Na^+ monotonically decreases from the peak point going away from the wall. O^- is much more important than O_2^- through the viscous layer, since the concentration of O^- is much higher than that of O_2^-. On the other hand, F^- does not play an important role in reducing the free electron number density as much as it does in the wake analysis case of Cresswell et al.(1967). The peak concentrations distribution of the ionized species NO^+, Na^+, O^-, O_2^- and F^- along the vehicle were compared in Fig. 31. The concentration of NO^+ decreased; however, that of Na^+ increased along the body. At near the end of vehicle, the peak concentration of Na^+ was approximately the same as that of NO^+.

3.1.5 Velocity, Density, and Pressure profiles

The profiles of flow field variables $\frac{u}{u_\infty}$, $\frac{v}{u_\infty}$, $\frac{\rho}{\rho_\infty}$, and $\frac{p}{p_\infty}$ are shown in Figs. 32 - 39. Boundary layer thickness $\delta(y_{\frac{u}{u_e}=0.99})$, is $\frac{\delta}{n_{sh}}$ = 0.6731 at s/Rn = 19.7 as shown in Fig. 32; thus viscous flow dominates 67 % of the shock-layer. However, at s/Rn = 52.3, δ becomes $\frac{\delta}{n_{sh}}$ = 0.3871, at which point the viscous region is confined to a narrow region near the wall (Fig. 33).

The mass-transfer through the surface reduces the velocity gradient at the wall, and it results in a low skin friction force ($\tau_w = \mu\frac{\partial u}{\partial y}$)(see Figs. 32 and 33).

Since the density at the wall for the teflon injection case is much higher than that of none-quilibrium injection case (refer to Figs. 34 and 35), the normal velocity at the wall v_w becomes

smaller ($(\frac{v}{u_\infty})_w$ = 0.00019 at s/Rn = 19.7 and 0.00016 at s/Rn = 52.3) in the teflon case than in the nonequilibrium air injection case ($(\frac{v}{u_\infty})_w$ = 0.000262 at s/Rn = 19.7 and 0.00022 at s/Rn = 52.3), as shown in Figs. 36 and 37. Figure 37 shows that the normal velocity becomes negative earlier than that of the nonequilibrium air blowing case.

Figures 38 and 39 show the pressure profile across the shock layer. The pressure gradient near the wall is nearly constant throughout the boundary layer. At s/Rn = 52.3, overexpansion occurred near the shock and then slightly recompressed as opposed to the monotonic decrease in pressure at s/Rn = 19.7.

3.1.6 Temperature Profiles

The temperature profile at s/Rn = 19.7 (Fig. 40) shows interesting double temperature peaks near the wall region. The first peak temperature (6665 R) for the nonequilibrium air injection case is higher than the second peak temperature (5207 R), and the effect of teflon ablation was enormous in reducing the first peak temperature to 5360 R. Moreover, at s/Rn = 52.3 the peak temperature drops 1512 R due to teflon blowing. As discussed in Chapter 2, the endothermic reaction (22) for CF_2, (24) for COF_2, (9) for CO_2 and the dissociative reaction(23) for CF_4, the heat capacity of ablation species and decreased viscous dissipation due to boundary layer blowing cause the temperature drop. Furthermore, the concentrations of CF_4, COF_2 and CO_2 at the wall are enough to cause a significant change in the temperature profile.

When we investigated the species concentration at the saddle point between the two temperature peaks as shown in Fig. 23, the maximum concentration of O and N which were dissociated from O_2 and N_2, respectively, occurred at the saddle point.

$$O_2 + M_1 = O + O + M_1 \quad (5.12ev) \qquad [1]$$

$$N_2 + M_2 = N + N + M_2 \quad (9.76ev) \qquad [2]$$

Reactions (1) and (2) are endothermic reactions which require a great deal of dissociation energy, and particularly, N_2 dissociation which requires much more energy than O_2 dissociation does.

O_2 was almost completely dissociated, while N_2 was substantially dissociated. At the saddle point, those dissociation reactions took energy from the flowfield, resulting in a temperature drop (2351 R for the no-injection case, 2173 R for the nonequilibrium air injection case and 951 R for the teflon injection case). The concentrations of the teflon ablation species were almost negligible at the saddle point, since their concentrations were much less than 0.01. Above the saddle point, O and N recombined and released energy, resulting in an appreciable temperature increase (500 R from its minimum temperature 4409 R for the teflon case, and the other cases were similar).

However, the double temperature peaks disappeared completely at s/Rn = 52.3 due to much less dissociation of N_2 at that position than at s/Rn = 19.7. In addition, this lower dissociation of N_2 raised the temperature peak (7792 R for the no-mass injection case) higher than that at s/Rn = 19.7 (6806 R for the no-mass injection case). In Fig. 41, blowing at the wall pushed the peak temperature point away from the wall: values of y/Rn of 0.2087 in the nonequilibrium case, 0.2050 for the teflon injection case , and 0.1487 for the no-mass injection case.

3.1.7 Molecular Weight, Prandtl No., and Specific Heat Ratio Profiles

Figures 42 and 43 show the average molecular weight profile which is defined as

$$\overline{M}^* = \frac{1}{\sum_{i=1}^{NS} \frac{C_i}{M_i^*}}$$

where M_i^* is the molecular weight of the individual species and NS is the number of species.

Due to teflon ablation through the wall, the average molecular weight increased to 41.458 from 28.878 for the nonequilibrium air value at the body surface. It is interesting to note that at s/Rn = 19.7, the minimum of $\overline{M}$ occurred at the saddle point between the temperature peaks, whereas

at s/Rn = 52.3, it occurred at slightly above the peak temperature where C_N and C_O were at their maximum. The Prandtl number ($\mathrm{Pr} = \frac{\mu C_p}{k}$) at the wall increased to 0.80146 from 0.761245 (see Figs. 44 and 45).

The specific heat ratio was calculated by using its definition:

$$\gamma = \frac{C_p}{C_v} = \frac{C_p}{C_p - \frac{R_u}{\overline{M}}}$$

where Cp is the specific heat of the mixture and R_u is a universal gas constant. Since $\overline{M}$ at the wall for the teflon injection case (Figs. 42 and 43) is much larger than that of either the nonequilibrium air injection or the no-mass injection cases, the specific heat ratio γ decreased to a value of 1.2096 in the teflon injection case (Figs. 46 and 47).

3.1.8 Surface-Measurable Quantities

Figures 48-51 show the surface-measurable quantities. Figure 48 shows the surface pressure distribution, wherein the agreement between mass injection and no-mass injection was quite good.

The surface heat-transfer distribution is shown in Fig. 49. A significant increase in the diffusional heat-transfer rate due to teflon ablation (see Table 10) along the vehicle raised the total heat-transfer rate above that of the equivalent nonequilibrium air injection case despite the reduction in the conduction heat-transfer rate. The increase in diffusional heat-transfer rate came from a strong concentration gradients of the species, such as O, N_2 (positive concentration gradients with positive enthalpy), and CO, CO_2, CF_4, COF_2 (negative concentration gradients with negative enthalpy) as shown in Table 11.

Table 10 shows a comparison of heat-transfer rate in case A between at s/Rn = 19.7 and at s/Rn = 52.3. There was a higher diffusional heat-transfer rate in the teflon case (

$-29.71\ Btu/ft^2/\text{sec}$) than in the no-mass injection case($-19.34\ Btu/ft^2/\text{sec}$), and this reduced the effect of the blowing, which, in turn, reduced the conduction heat-transfer rate. The convection heat-transfer rate ($1.788 Btu/ft^2/\text{sec}$) reduced the total heat-transfer rate by less than 4 %.

Since the region of interest was far downstream from the nose region, the heat-transfer rate comparison was not made in the nose region where the diffusional heat-transfer rate was quite large. When the total heat-transfer rate at s/Rn = 52.3 was observed, it was found that the overall heat-transfer rate of teflon ablation was 20 % less than that of no-mass injection case, and the overall heat-transfer rate for the nonequilibrium air injection case was 54% less than that of the no-mass injection case. Figure 50 shows the distribution of skin-friction coefficient (C_{f_s}) along the body. Blowings of teflon and nonequilibrium air reduced skin-friction coefficient by 43% and 54%, respectively.

When peak temperatures were compared among teflon, air injection, and no-mass injection in Fig. 51, it was found that the overall temperature difference between teflon and air injection or no-mass injection was more than 1500 R.

The axial force coefficients (CA) are tabulated in Table 9. The axial force coefficient at s/Rn = 52.3 due to the pressure drag was much higher than that due to the skin-friction drag. Since the pressure drags were almost identical, the differences in CA were less than 6%. The CA distribution comparison is shown in Fig. 52.

3.2 Part 2

3.2.1 Freestream Species and Equilibrium Wall Species Concentration

Figure 53 shows the concentration of freestream species (viz. nonequilibrium air) at the wall. Figures 54 and 55 show the equilibrium species concentration at the wall. F appeared near the nose region only; however, the other species were similar to Case A.

3.2.2 Species Profiles

The species profiles of O, O_2, NO, N and N_2 are very similar to those of case A (Figs. 56 and 57). Figures 58 and 59 show the species profiles of C, CO, CO_2, Na, CF_4, CF_2, F_2, F, and COF_2 at s/Rn = 6, and at s/Rn = 22.3, respectively. The concentration of carbon at s/Rn = 6 is one order of magnitude higher than that of carbon at s/Rn = 19.7 of case A, and at s/Rn = 22.3 C_C is two orders of magnitude higher than that of C_C at s/Rn = 52.3 of case A. C_F is four orders of magnitude less than C_C at s/Rn = 22.3; C_C, however, is one order of magnitude less than C_F in case A at s/Rn = 52.3.

3.2.3 Electron Density Profiles

The peak electron density at s/Rn = 6.0 and at s/Rn = 22.3 are 1.8×10^{12} and 3.1×10^{11} electrons/ cm^3 , respectively, as shown in Figs. 60 and 61. The major source of free electrons for

case B comes from NO^+ (refer to Figs. 62 and 63). The peak concentration distribution of ionized species is compared in Fig. 64. The concentration of NO^+ was decreased along the body, but the major source of free electrons was NO^+ over all the vehicle.

3.2.4 Temperature Profiles

In Fig. 65 the temperature decrease (438°R) due to the teflon ablation at s/Rn = 6.0 was less than that of case A (1305°R) at s/Rn = 19.7, while Fig. 66 shows the temperature decrease of 748°R at s/Rn = 22.3 as opposed to that of 1512°R for case A at s/Rn = 52.3. It was very hard to compare the two conditions exactly, since the flight conditions were different and also the vehicle lengths were different even though they were the same actual location on the 7-deg. cone vehicle (Fig. 2).

The second peak temperature (6787°R) was higher than that of the first peak (6284°R) at s/Rn = 6 for the nonequilibrium air injection or no-mass injection cases, both in opposition to case A (Fig. 40).

3.2.5 Surface-Measurable Quantities

Since no significant differences in profiles of pressure, density, average molecular weight, Pr, and γ were observed in case B, the comparisons are not shown. Figures 67, 68 and 69 show the heat-transfer rate, skin friction coefficient, and axial force coefficient distributions along the body, respectively. The skin-friction coefficient was reduced due to teflon blowing and air injection from that of the no-mass injection case by 45 % and 51.8 %, respectively.

Figure 70 shows the peak temperature comparison along the body. There was a very small difference in peak temperature up to s/Rn = 8.0, because the second peak temperature, which was not affected by blowing, was the highest peak temperature. But the peak temperature difference became large further downstream, and the difference between teflon blowing and no-mass injection at the body end (s/Rn = 22.3) was 848°*R* which was much lower than the difference of 1512 R in case A.

3.3 Computing Times

The computing time required for each test case on the IBM 3084 (with H-compiler and OPT = 2 optimization) is shown in Table 12. The computing time of the no-mass injection case was taken as a reference at each test case, and the relative time ratios for each test case are tabulated in Table 12.

When an input shock is not accurate, a global iteration is generally required, thus consuming more computing time than the value shown in the table. The CPU time required per grid point for case A was much higher than the time required for case B, since we used a profile weighting over the nose region due to a convergence problem in species concentration profiles at 125 kft altitude.

4.0 Conclusions

A complex chemical system of teflon/air mixture over an axisymmetric sphere-cone decoy at hypersonic flight conditions has been analyzed by using the nonequilibrium viscous shock-layer method.

Due to lack of experimental or theoretical data, the surface- measurable quantities from the current code (VSLTEF) were compared with the equivalent nonequilibrium air injection and no-mass injection data obtained from VSL7S code. The current code predicts a higher heat-transfer rate than that predicted by the seven species nonequilibrium code with the same injection rate due to the high diffusional heat-transfer rate. The wall pressure distribution was not affected by the blowing, while the skin friction was decreased substantially by teflon and air injection (i.e., 43 % reduction for teflon blowing; 53 % for the nonequilibrium air injection in case A).

A shock-layer peak temperature drop (1512°R for 125 kft and 848°R for 175 kft) was observed at both altitudes. The temperature drop was chiefly due to endothermic reactions and the heat capacity of teflon ablation species and due to decreased viscous dissipation.

Due to the blowing of teflon, the average molecular weight increased substantially and resulted in a reduction of specific heat ratio γ and an increase in the Prandtl number at the wall.

The impurity of sodium was the major source of electrons near the wall at the end of the vehicle at 125 kft altitude; however, at 175 kft altitude, NO^+ was the major source of free electrons

all along the body. The peak concentration of sodium ion (Na^+) increased downstream; however, that of NO^+ decreased at both altitudes.

While the chemical reaction rate data used is believed to be the best currently available, uncertainties in this data as were cited by Cresswell et al.(1967) may lead to quantitative changes in the above teflon blowing results.

In conclusion, a method has been developed for analyzing nonequilibrium finite-rate chemically reacting flows over multiconic geometries with ablating teflon surfaces.

5.0 Future Recommendations

The following are suggested for further study;

1. Additional calculations should be made with higher wall mass-transfer rates, because the mass addition rate is a very important parameter.

2. Effects of teflon blowing on a three-dimensional lifting body should be investigated.

3. Since sodium supplied a large amount of the free electrons, the effects of different sodium levels should be studied.

4. Since the rate data of the chemical reactions are in some doubt, the effects of variation in the rate constants, especially on the electron concentration, should be investigated.

References

Appleton, J. P., Steinberg, M., and Liquornik, D. J. (1970), "Shock-Tube Study of Carbon Monoxide Dissociation Using Vacuum-Ultraviolet Absorption," *Journal of Chemical Physics,* Vol. 52, pp. 2205-2221.

Baron, J. R. (1956), " The Binary Boundary Layer Associated with Mass Transfer Cooling at High Speeds," TR 160, Naval Supersonic Lab.,Masschusetts Institute of Technology.

Bhutta, B. A., and Lewis, C. H. (1985), " An Implicit Parabolized Navier-Stokes Scheme for High Altitude Reentry Flows, " AIAA Paper No. 85-0036.

Biolsi, L.(1986), Private Communication.

Bird, R. B., Stewart, W. E. and Lightfoot, E. N. (1960), *Transport Phenomena,* John Wiley and Sons, Inc., New York, NY.

Blottner, F. G., Johnson, M., and Ellis, M. (1971), "Chemically Reacting Viscous Flow Program for Multi-Component Gas Mixtures," Sandia Laboratories, Albuquerque, NM, SC-RR-70-754.

Brant, D. N. (1973), "Investigation of Teflon Performance on the MK 12 Nosetip ," GE-RESD PIR-9151-AE-104.

Browne, W. G. (1962a), "Thermodynamic Properties of Some Atoms and Atomic Ions," General Electric Co., Philadelphia, Pa., MSD Engineering Physics TM2.

Browne, W. G. (1962b), "Thermodynamic Properties of Some Diatomic and Linear Polyatomic Molecules," General Electric Co., Philadelphia, Pa., MSD Engineering Physics TM3.

Browne, W. G. (1962c), "Thermodynamic Properties of Some Diatomic and Diatomic Ions at High Temperatures," General Electrical Co., Philadelphia,Pa., MSD Advanced Aerospace Physics TM8.

Browne, W. G., and Miller, Jeanne (1965), " Thermodynamic Properties of Some Ablation Products From Teflon Heat Shields in Air," General Electrical Co., Philadelphia, No. 65SD5315.

Browne, W. G.(1986), Private Communication.

Chapman, S., and Cowling, T. G.(1939), *The Mathematical Theory of Nonuniform Gases,* Cambridge University Press, New York.

Cresswell, J., Kaplan, B., Porter, R., and Sarcos, C. (1967), " Material Effects of Low Temperature Ablators on Hypersonic Wake Properties of Slender Bodies," General Electrical Co., Valley Forge, PA, Rept. TIS 67SD255.

Davies, W. O. (1965), "Carbon Dioxide Dissociation at 6000 K to 11000 K," *Journal of Chemical Physics,* Vol. 43, pp. 2809-2818.

Davis, R. T. (1970a), "Numerical Solution of Hypersonic Viscous Shock-Layer Equations, " *AIAA Journal,* Vol. 8, pp. 843- 851.

Davis, R. T. (1970b), "Hypersonic Flow of Chemically Reacting Binary Mixture Past a Blunt Body, " AIAA Paper No., 70-805.

Esch, D. D., Siripong, A, and Pike, R. W., (1970), "A Technical Report on Thermodynamic Properties in Polynomial Form for Carbon, Hydrogen, Nitrogen, and Oxygen systems From 300 to 15000 K," NASA-RFL-TR-70-3.

Fay, J. A., and Riddell, F. R. (1958), "Theory of Stagnation Point Heat Transfer in Dissociated Air," *Journal of the Aeronautical Sciences,* Vol. 25, pp. 73-85.

Gordon.,S., and McBride, B. J. (1976), "Computer Program for calculation of Complex Chemical Equilibrium Compositions, Rocket Performance, Incident, and Reflected Shocks, and Chapman-Jouguet Detonations," NASA SP-273.

Hecht, A. M. and Nestler, D. E. (1978), "A Three Dimensional Boundary-Layer Computer Program for Sphere-Cone type Reentry Vehicles, Vol. I, Engineering Analysis and Code Description," Wright Patterson AFB, OH, AFFDL-TR-78-67.

Jaffe, N. A., Lind, R. C., and Smith, A. M. O. (1967), " Solution to the Binary Diffusion Laminar Boundary-Layer Equations with Second-Order Transverse Curvature," *AIAA Journal,* Vol. 5, pp. 1563-1569.

Kim, M. D., and Lewis, C. H. (1983), "Three-Dimensional Nonequilibrium Viscous Flow over the Shuttle with Surface Catalytic Effects," AIAA Paper No. 83-1426.

Kiyama, R., and Makita, T. (1952), " The Viscosity of Carbon Dioxide, Ammonia, Acetylene, Argon, and Oxygen under High Pressures," *Rev. Phys. Chem.(Japan),* Vol. 22, pp. 49-58.

Langan, W. T., Cresswell, J. D., and Browne, W. G. (1965), "Effects of Ablation Products on Ionization in Hypersonic Wakes," General Electric Co., Valley Forge, Pa., TIS 65SD208.

Lees, L. (1956), "Laminar Heat Transfer Over Blunt-Nosed Bodies at Hypersonic Flight Speeds," Jet Propulsion, pp. 259-269

Leibowitz, P. L. (1973), " Measurements of the Structure of an Ionizing Shock Wave in Hydrogen-Helium Mixture," *The Physics of Fluids,* Vol. 16, pp. 59-68.

Mayne, A. W., Gilley, G. E., and Lewis, C. H. (1969), "Binary Boundary Layers on Sharp Cones in Low Density Supersonic and Hypersonic Flow," AEDC- TR-68-275.

McCoubrey, J. C., and Singh, N. M. (1957), " Intermolecular Forces in Quasi- Spherical Molecules," *Trans. Faraday Soc.,* Vol. 53, pp. 877-883.

Miner, E. W., and Lewis, C. H. (1975), "Hypersonic Ionizing Air Viscous Shock-Layer Flows Over Nonanalytic Blunt Bodies," NASA CR-2550.

Modica, A. P. and LaGraff, J. E. (1965a), "Thermal Decomposition of C_2F_4 behind Shock Waves, I. Kinetics and Equilibria of $C_2F_4 - CF_2$ Reaction,", AVCO RAD-TM-65-3.

Modica, A. P. and LaGraff, J. E. (1965b), "Shock Tube Kinetic Studies of the Tetrafluoroethylene-Oxygen System, " AVCO RAD-TM-65-29.

Moss, J. N. (1971), "Solutions for Reacting and Nonreacting Viscous Shock Layers with Multi-component Diffusion and Mass Injection," PhD Dissertation, VPI & SU, Blacksburg, Va..

Moss, J. N. (1984), private communication.

Murray, A. L. and Lewis, C. H. (1978a), "Hypersonic Three Dimensional Viscous Shock-Layer Flow over blunt bodies," *AIAA Journal,* Vol. 16. pp. 64-69.

Murray, A. L. and Lewis, C. H. (1978b), "Three Dimensional Fully Viscous Shock-Layer Flows Over Sphere-Cones at High Altitudes and High Angles of Attack," Virginia Polytechnic Institute & State University, Blacksburg, Va., VPI-AERO-078.

Neufeld P. D., Janzen, A. R. and Aziz, R. A. (1972), " Empirical Equations to Calculate 16 of the Transport Collision Integrals $\Omega^{(l,s)^*}$ for the Lennard-Jones (12-6) potentials, " *Journal of Chemical Physics,* Vol.57, pp. 1100- 1102.

Petschek, H. and Byron, S. (1957), " Approach to Equilibrium Ionization behind Strong Shock Waves in Argon," *Ann. Phys.*, Vol. 1, pp. 270.

Rakich, J. V.(1969), *A Method of Characteristics for Steady 3-D Supersonic Flow with Application to Inclined Bodies of Revolutions,* NASA Tn D-5341.

Reid, R. C., Prausnitz, J. M., and Sherwood, T. K. (1977), *The Properties of Gases and Liquids,* McGraw-Hill Book Co., New York.

Scala, S. M., and Gilbert, L. M. (1963), "Theory of Hypersonic Laminar Stagnation Region Heat Transfer in Dissociating Gases," General Electric Co., Valley Forge, Pa.,TIS R63SD40.

Schofield, K. (1973), "Evaluated Chemical Kinetic Rate Constants for Various Gas Phase Reactions," *Journal of Phys. Chem. Ref. Data,* Vol. 2, pp. 25-84.

Scott, C. D., Ried, R. J., Li, M. C., and Derry, S. M.(1984), " An AOTV Aeroheating and Thermal Protection Study," AIAA Paper No. 84-1710.

Solomon, J. M., Ciment, M., Furguson, R. E., Bell, J. B. and Wardlow, Jr.,A. B. (1977), "A Program for Computing Steady Inviscid Three-Dimensional Supersonic Flow on Reentry Vehicles, Vol. 1, Analysis and Programming," Naval Surface Weapons Center, White Oak, MD, Report No. NSWC/WOL/TR 77-28.

Song, D. J. (1984), " Hypersonic Finite-Rate Chemically Reacting Viscous Flows over an Ablating Carbon Surface ", MS thesis, Virginia Polytechnic Institute and State University, Blacksburg, Va.

Song, D. J., and Lewis, C. H. (1986), " Hypersonic Finite-Rate Chemically Reacting Viscous Flows over an Ablating Carbon Surface ", *Journal of Spacecraft and Rocket,* Vol. 23, pp. 47-54.

Svehla, R. A. (1962), " Estimated Viscosities and Thermal Conductivities of Gases at High Temperature," NASA TR-132.

Swaminathan, S., Kim, M. D., and Lewis, C. H. (1983a), "Nonequilibrium Viscous Shock-Layer Flows Over Blunt Sphere-Cones at Angles-of-Attack," *Journal of Spacecraft and Rocket,* Vol. 20, pp. 331-338.

Swaminathan, S., and Lewis, C. H. (1983b), "Effects of Chemical Modelling on Three-Dimensional Nonequilibrium Viscous Shock-Layer Flows," AIAA Paper No. 83-1425.

Swaminathan, S., Kim, M. D., and Lewis, C. H. (1984), "Three-Dimensional Viscous Shock-Layer Flows Over Complex Geometries," *AIAA Journal,* Vol. 22, pp. 754-755.

Swaminathan, S., Song, D. J., and Lewis, C. H. (1984), "High Altitude Effects on Three-Dimensional Nonequilibrium Viscous Shock-Layer Flows," AIAA Paper No. 84-0304.

Thompson, R. A. (1983), "Viscous Shock Layer Flows over Multiconic Reentry Vehicles," MS Thesis, Virginia Polytechnic Institute & State University, Blacksburg, Virginia.

Tiwari, G. P., and Szema, K. Y. (1979), " Effects of Precursor Heating on Radiative and Chemically Reacting Viscous Flow around a Jovian Entry Body, " NASA CR-3186.

Vincenti, W. G. and Kruger, C. H. Jr. (1967), *Introduction to Physical Gas Dynamics,* Wiley, New York.

Figures

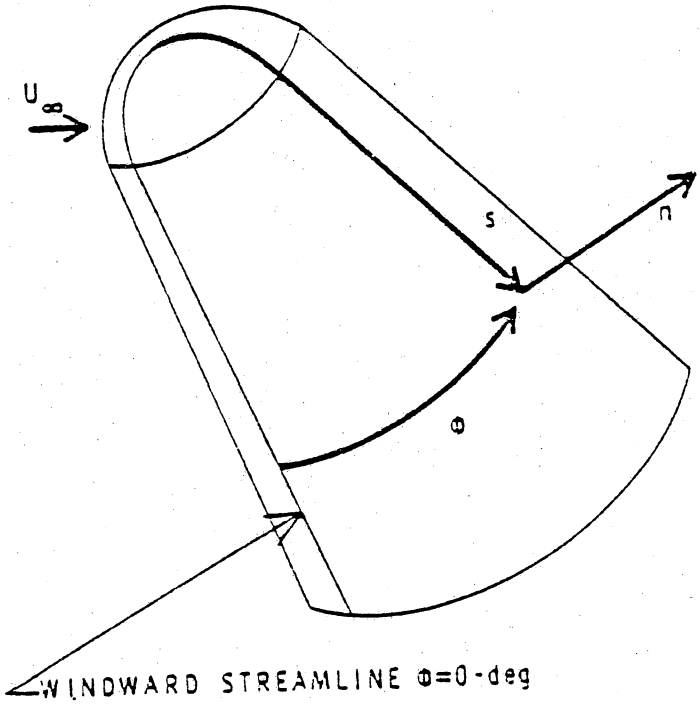

Figure 1. Body-normal coordinate system used in Viscous Shock-Layer code

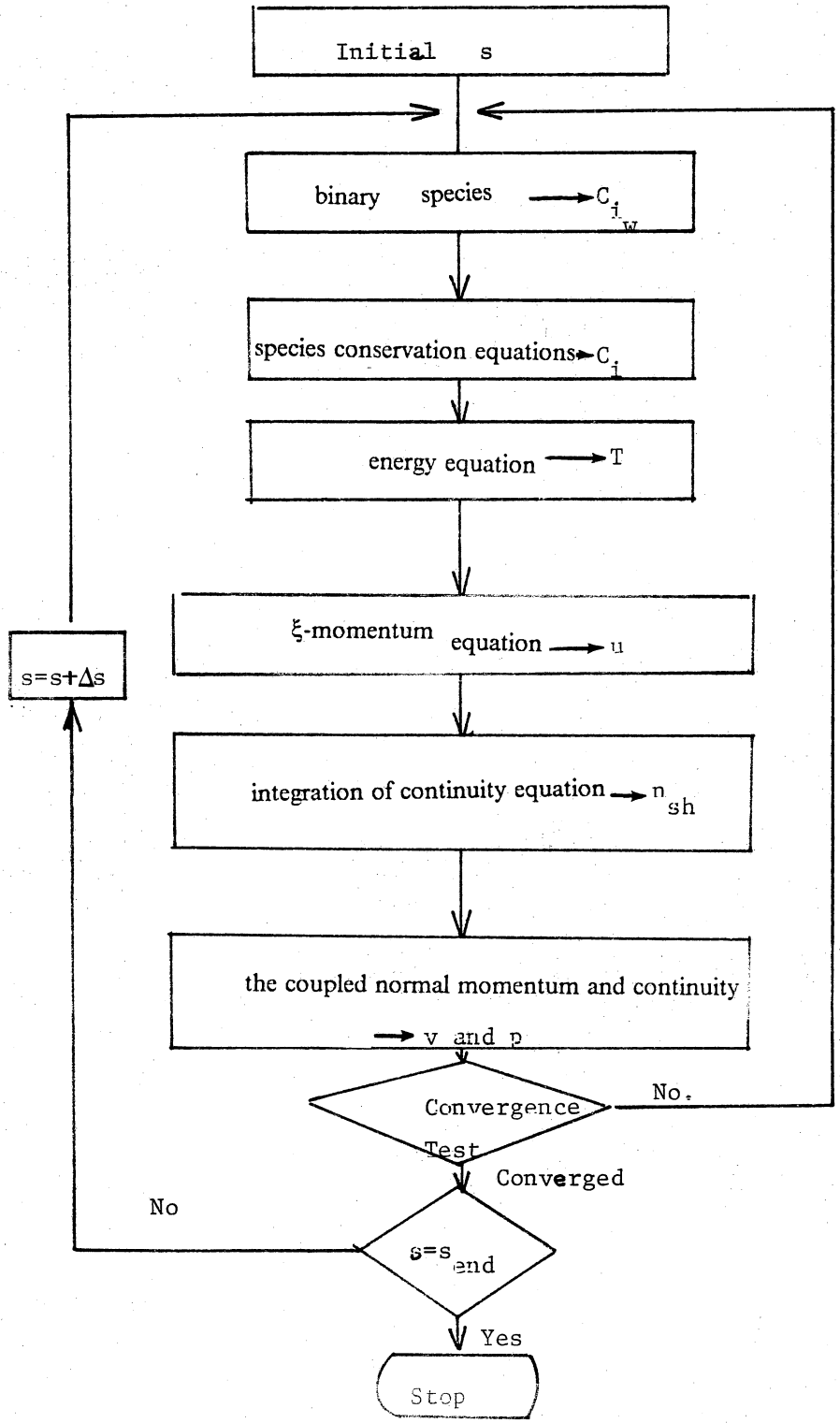

Figure 2. Flow diagram of axisymmetric Viscous Shock-Layer code with ablating teflon surface.

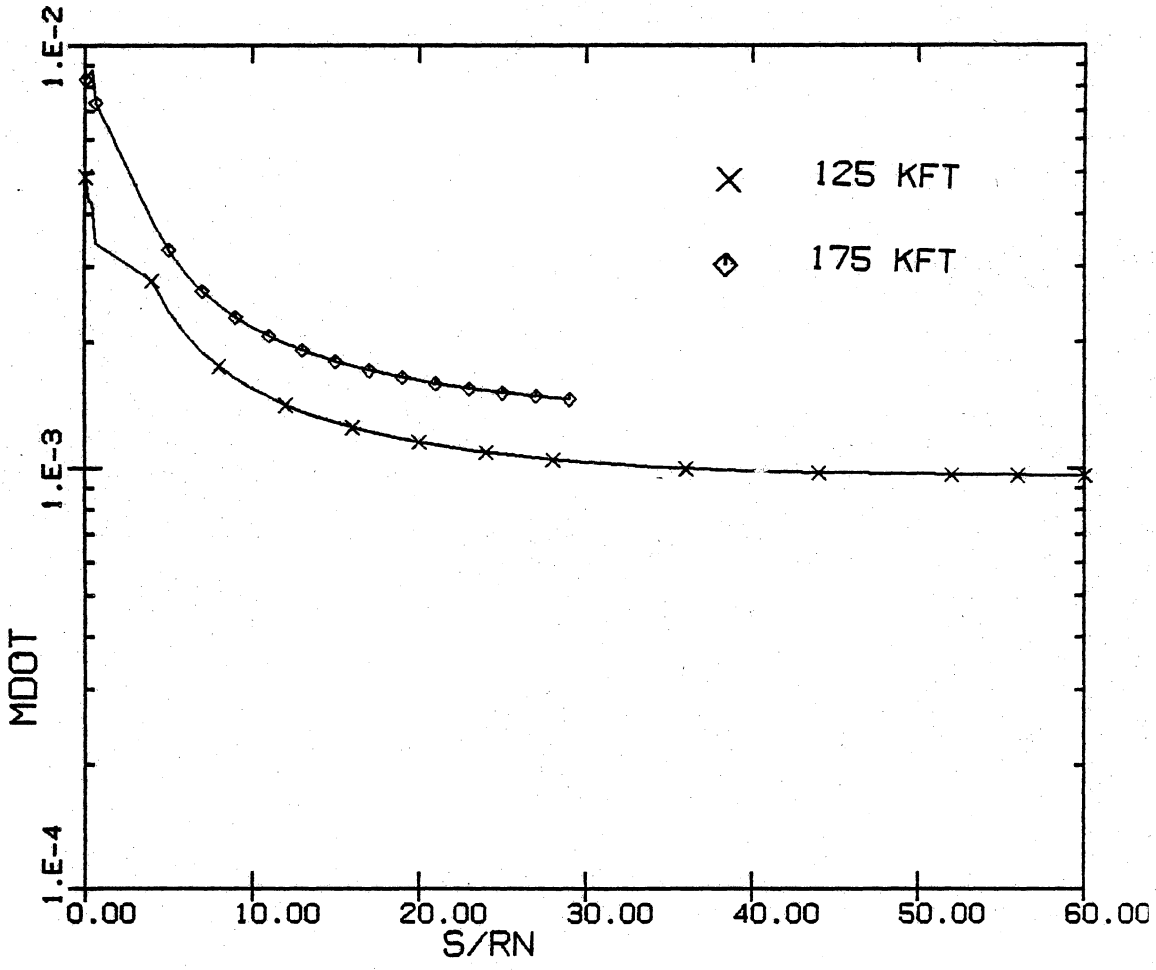

Figure 3. Mass-transfer distribution along the body for case A and case B

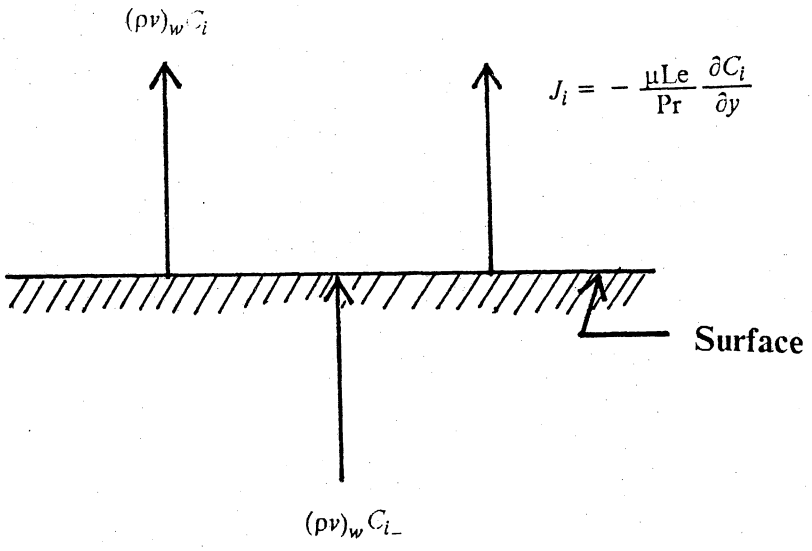

Figure 4a Schematic drawing for surface mass-transfer

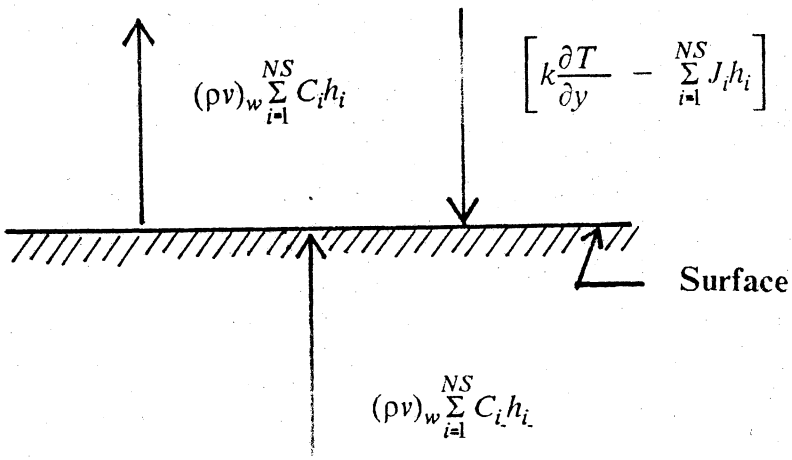

Figure 4b Schematic drawing for surface heat-transfer phenomena

Figure 4. Schematic drawing for surface mass-transfer and heat-transfer phenomena

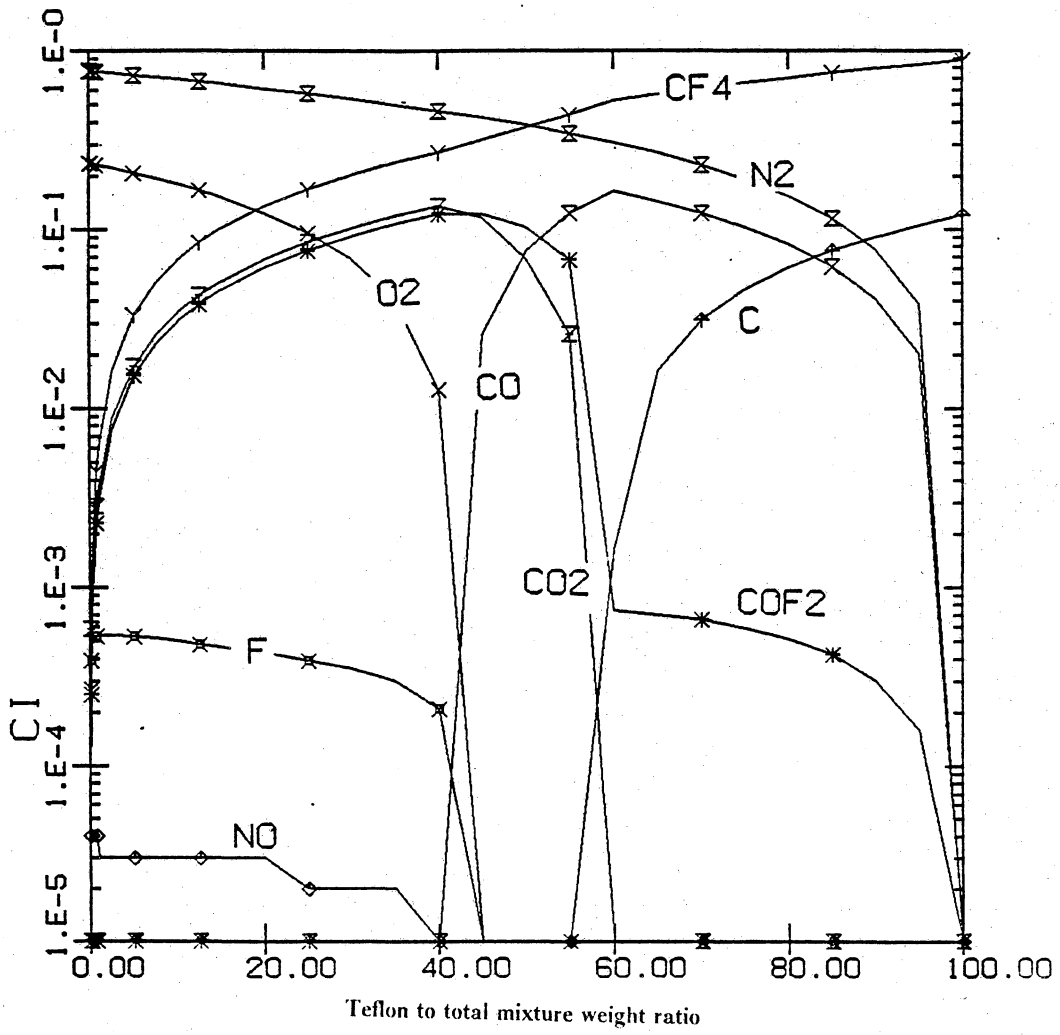

Figure 5. Teflon to total mixture weight ratio vs. species concentration at pressure = 0.001 psi

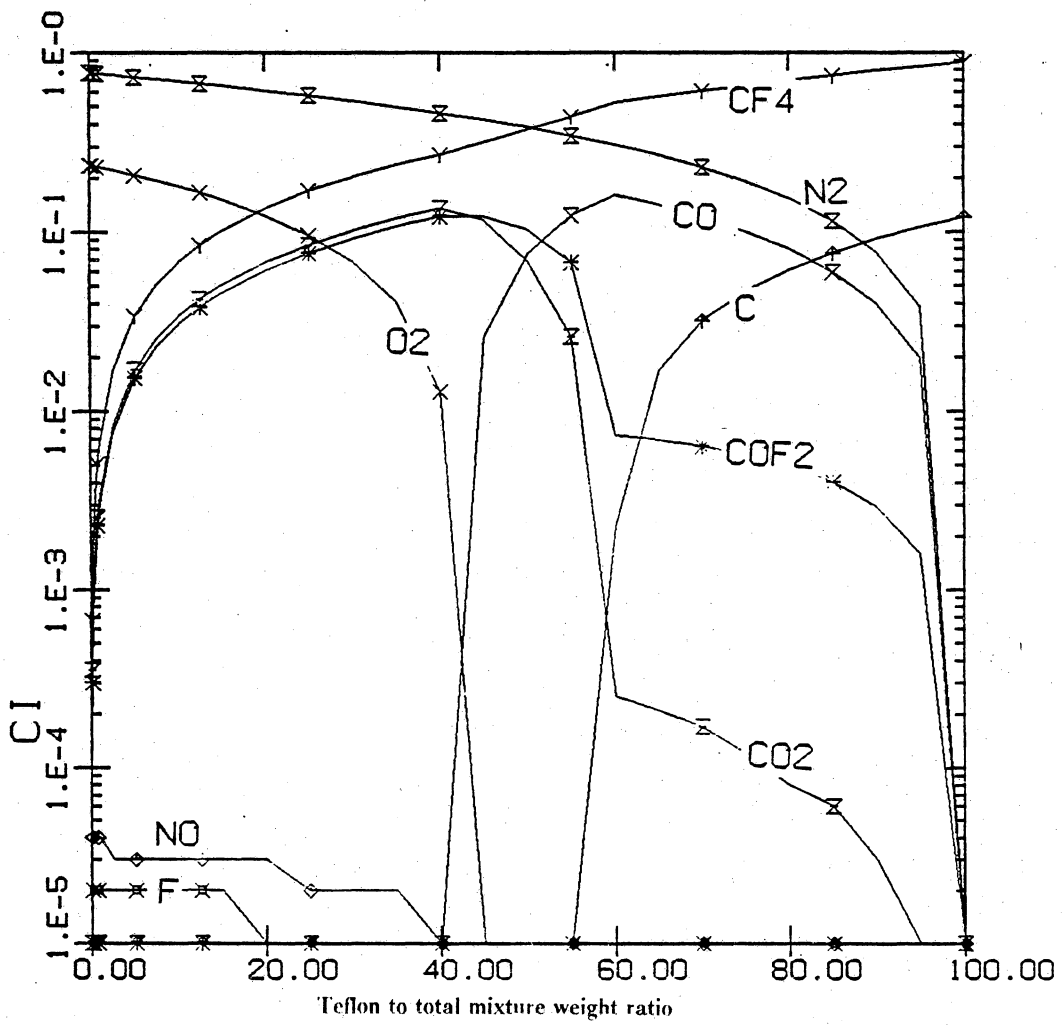

Figure 6. Teflon to total mixture weight ratio vs. species concentration at pressure = 0.1 psi

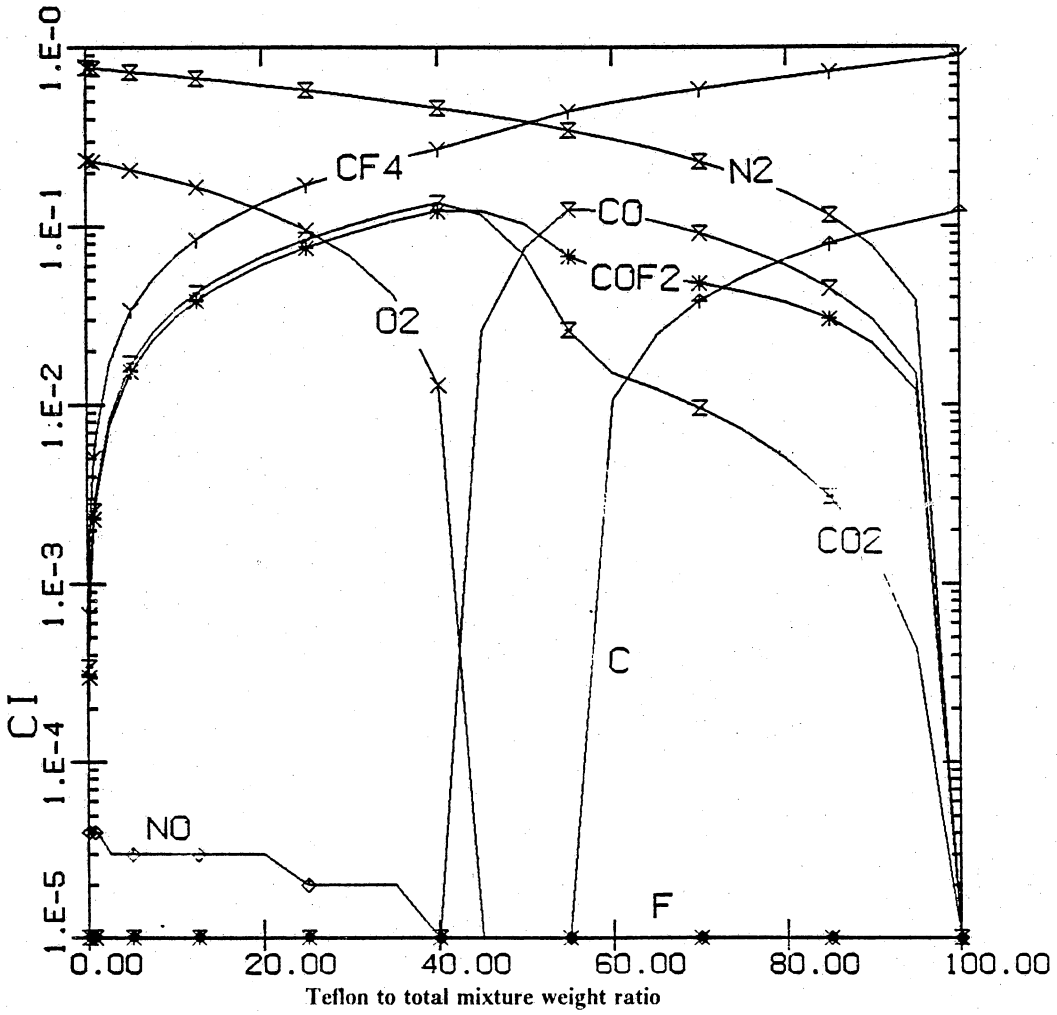

Figure 7. Teflon to total mixture weight ratio vs. species concentration at pressure = 10.0 psi

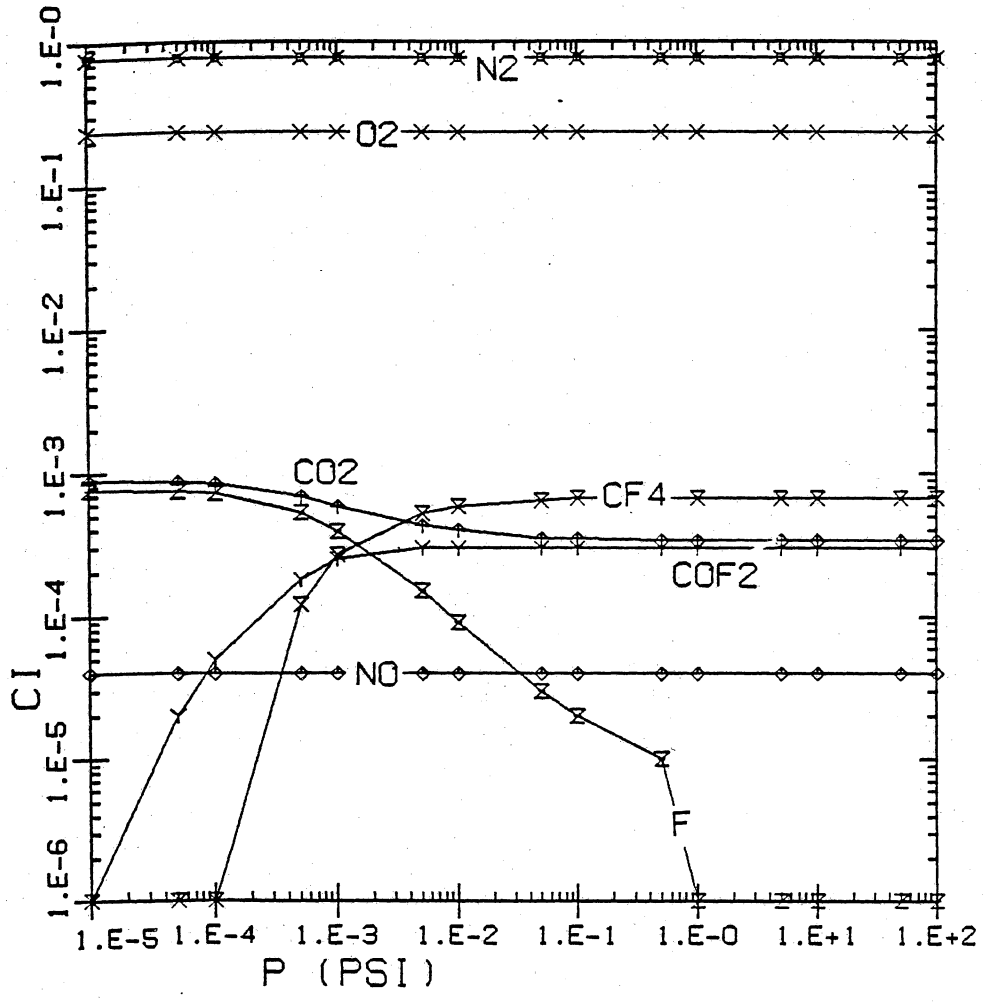

Figure 8. Pressure vs. species concentration at teflon to total mixture weight ratio of 0.1%

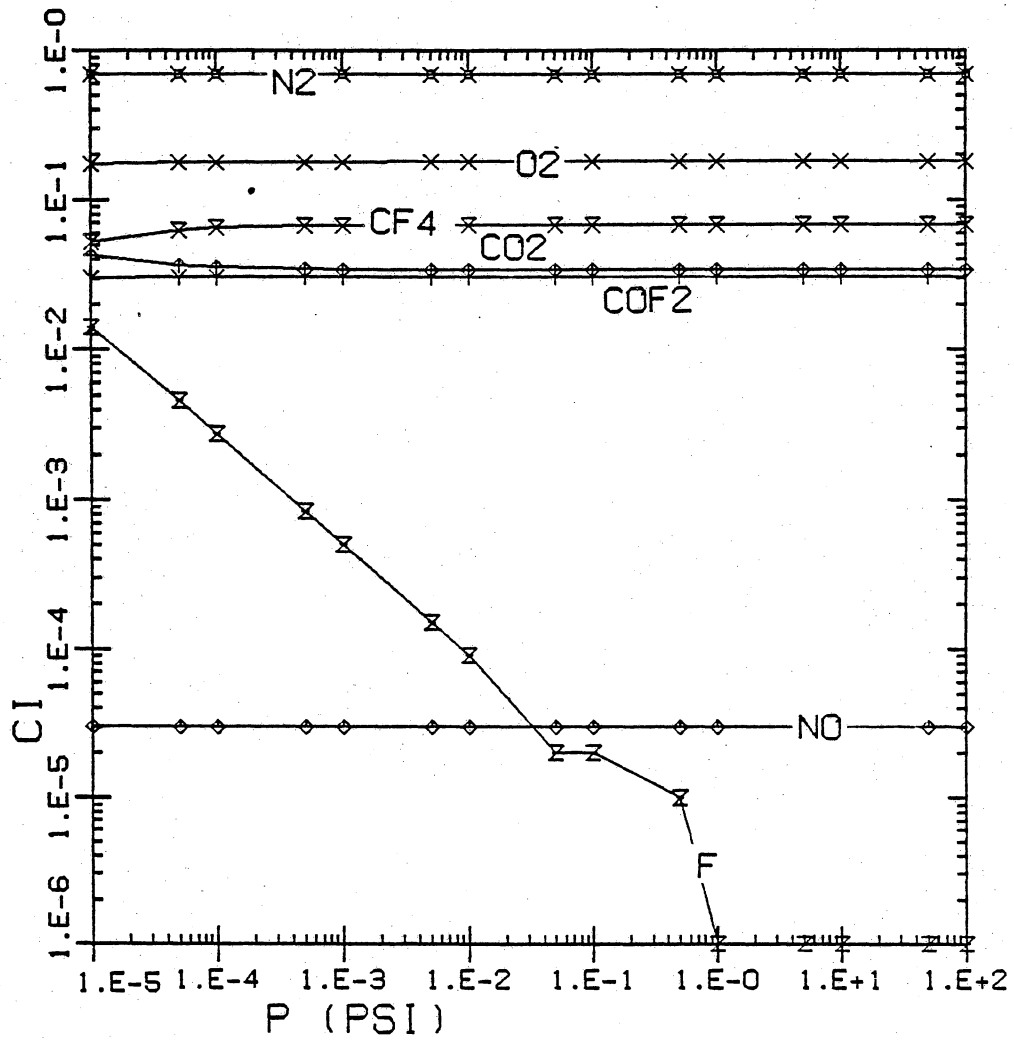

Figure 9. Pressure vs. species concentration at teflon to total mixture weight ratio of 10.0%

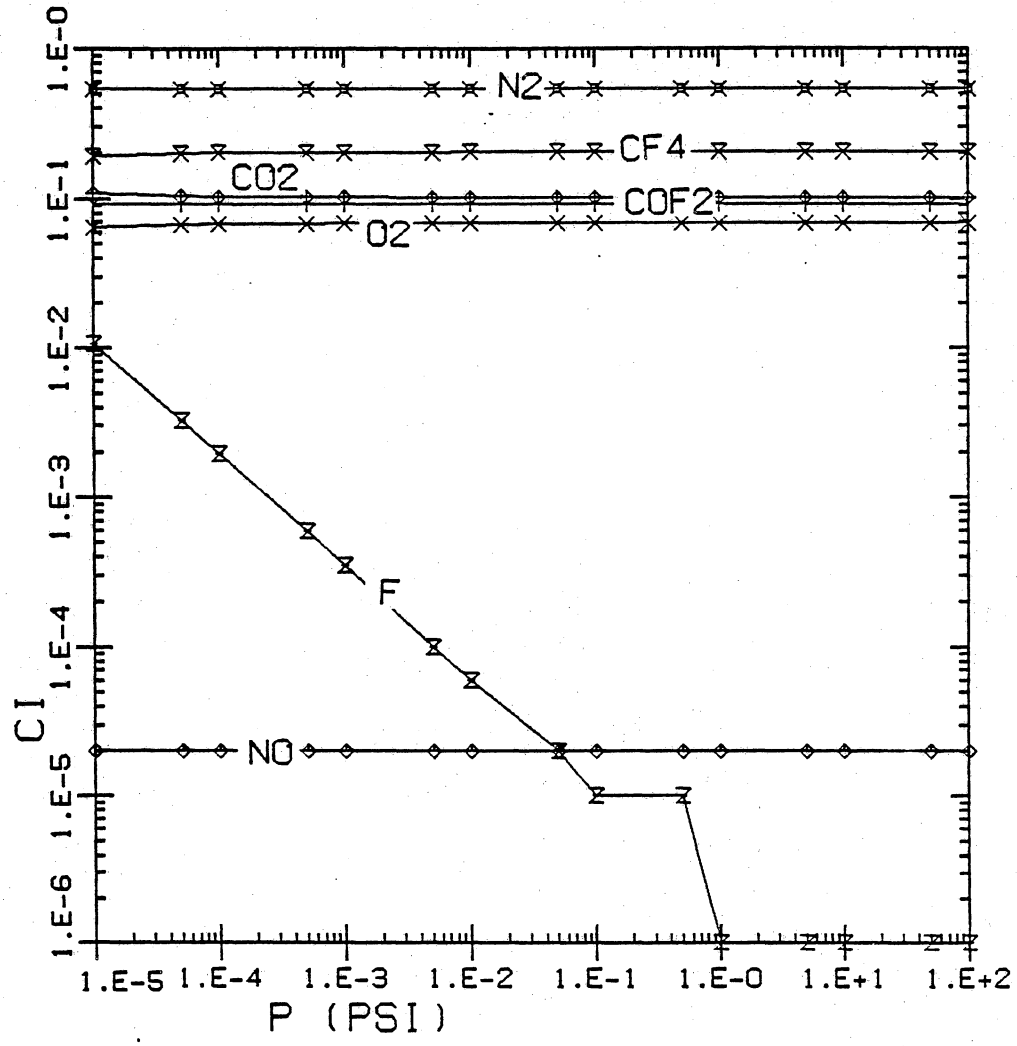

Figure 10. Pressure vs. species concentration at teflon to total mixture weight ratio of 30.0%

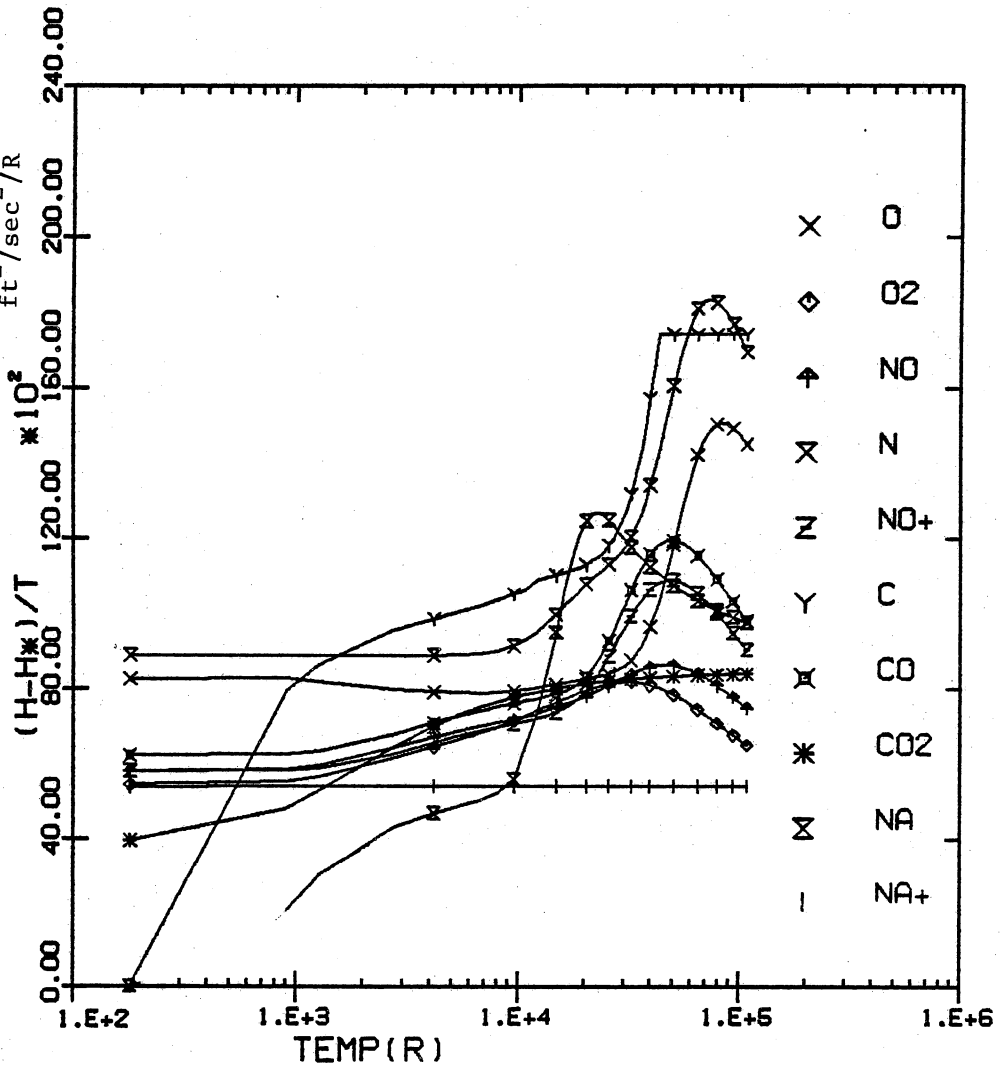

Figure 11. Enthalpy of the species O, O_2, NO, N, NO^+, C, CO, CO_2, Na, Na^+

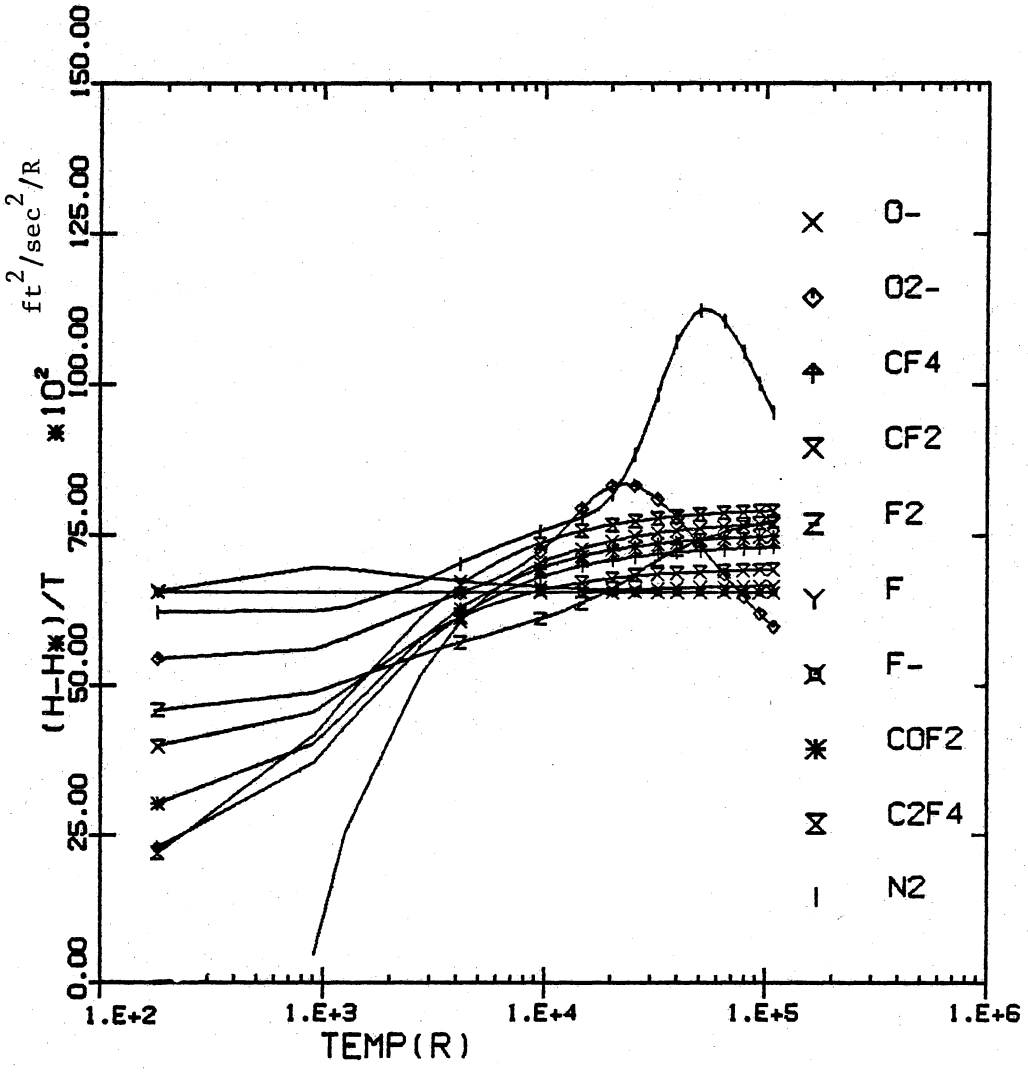

Figure 12. Enthalpy of the species O^-, O_2^-, CF_4,CF_2, F_2, F, F^-, COF_2, C_2F_4, N_2

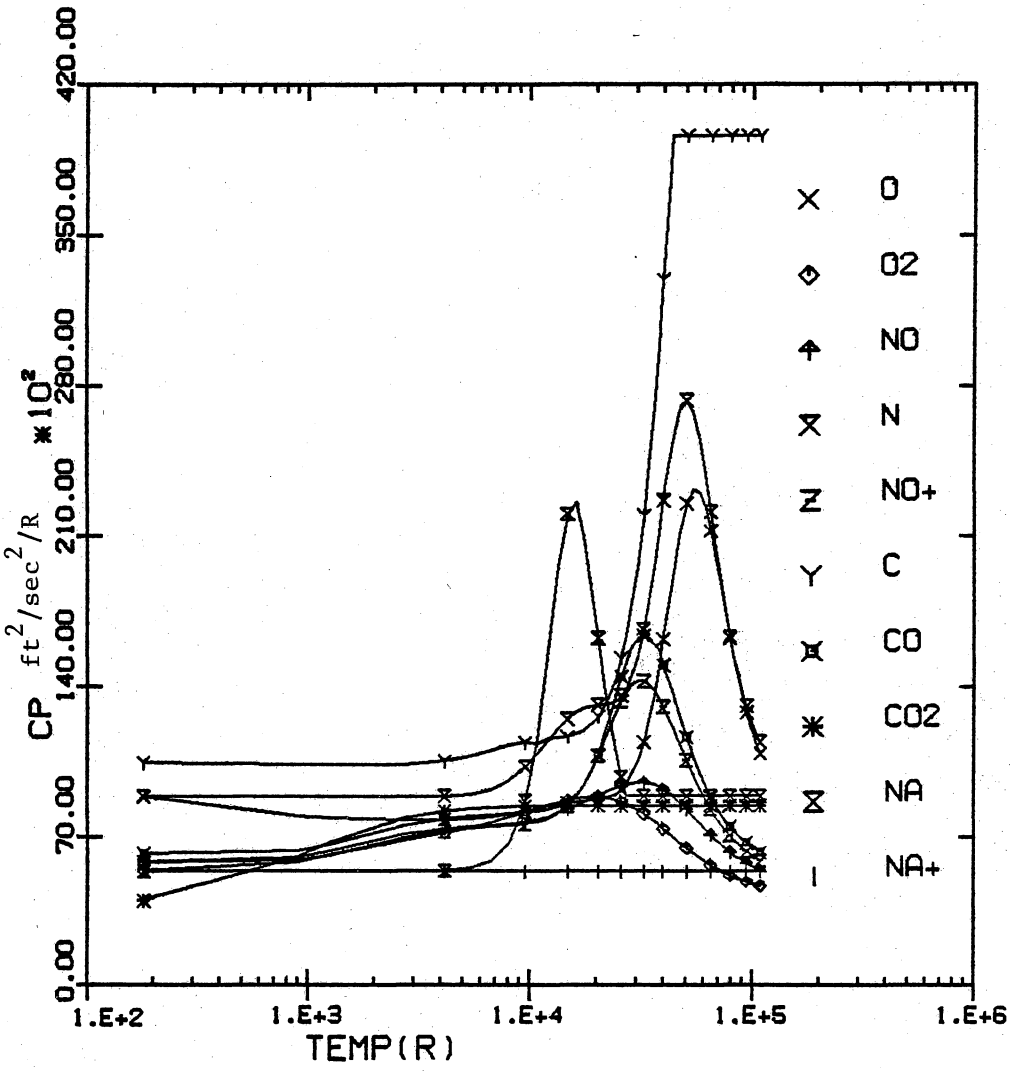

Figure 13. Specific heat of the species O, O_2, NO, N, NO^+, C, CO, CO_2, Na, Na^+

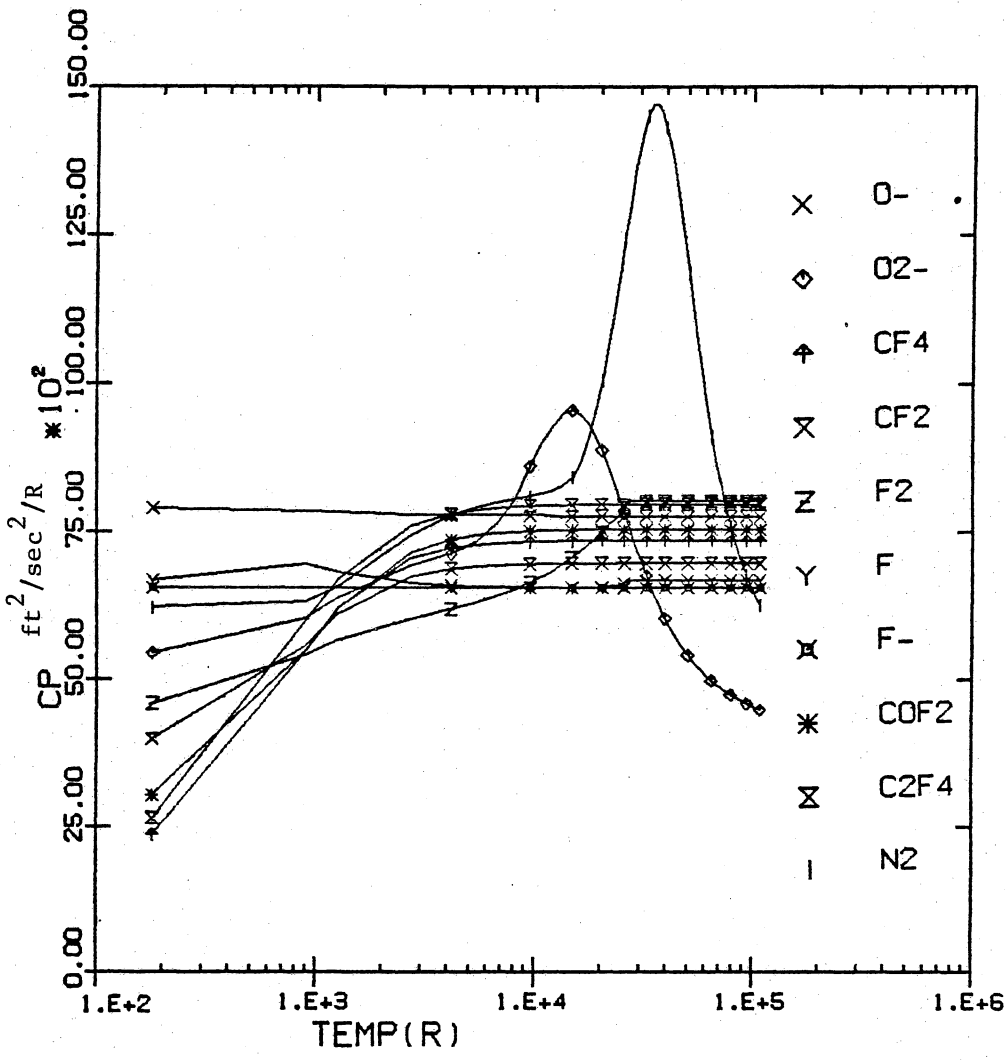

Figure 14. Specific heat of the species O^-, O_2^-, CF_4,CF_2, F_2, F, F^-, COF_2, C_2F_4, N_2

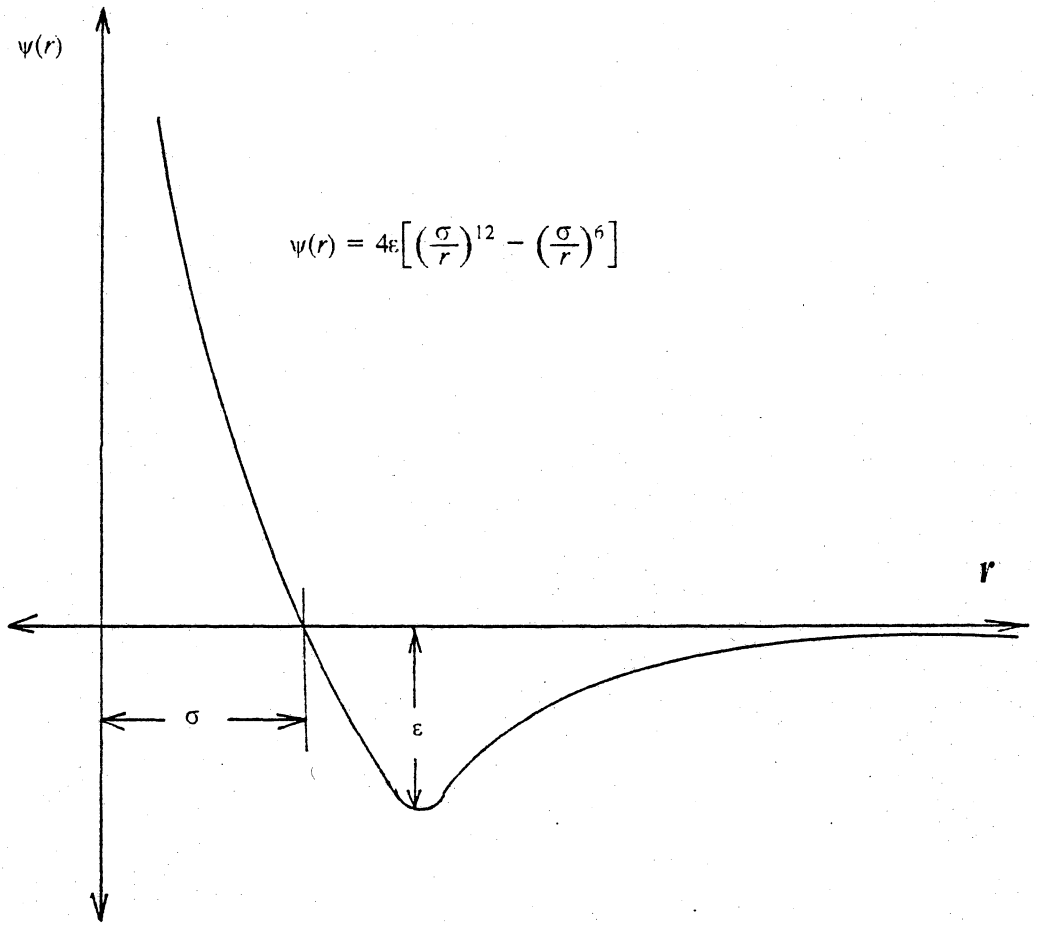

Figure 15. Schematic drawing for Lennard-Jones 12-6 potential

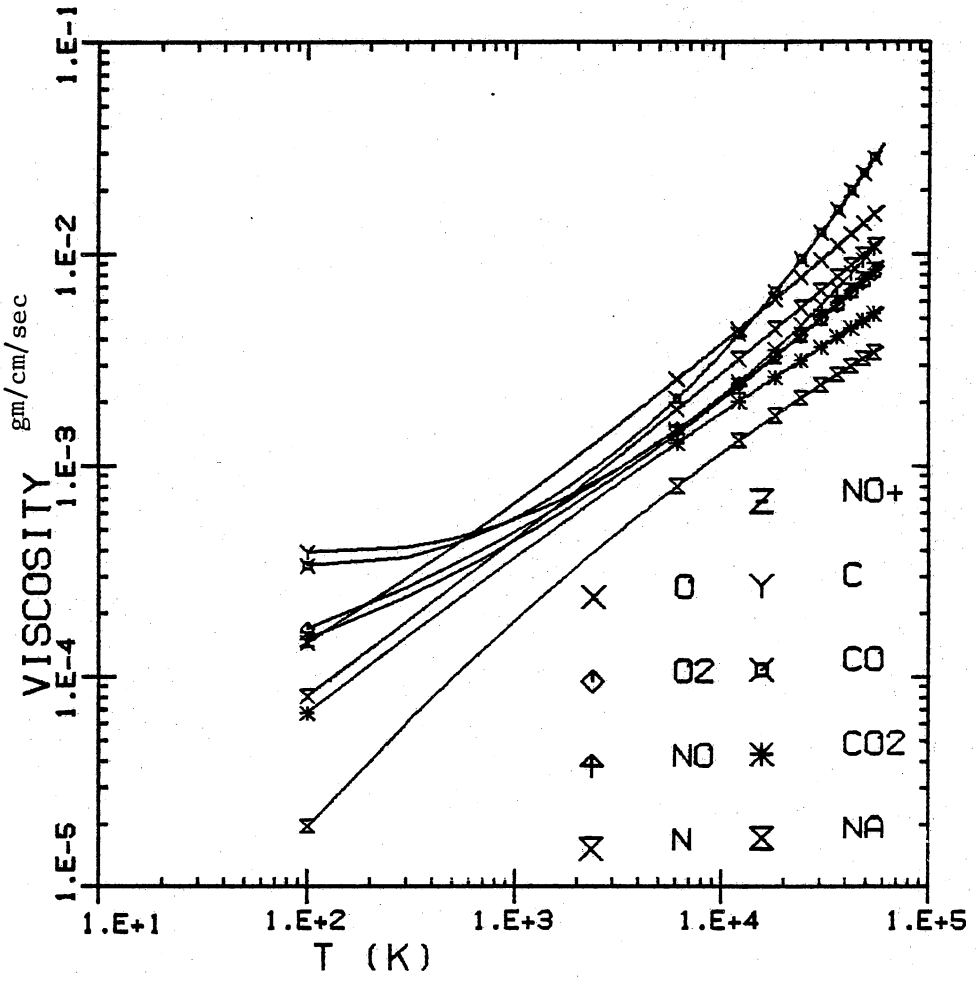

Figure 16. Viscosity of the species O, O_2, NO, N, NO^+, C, CO, CO_2, Na

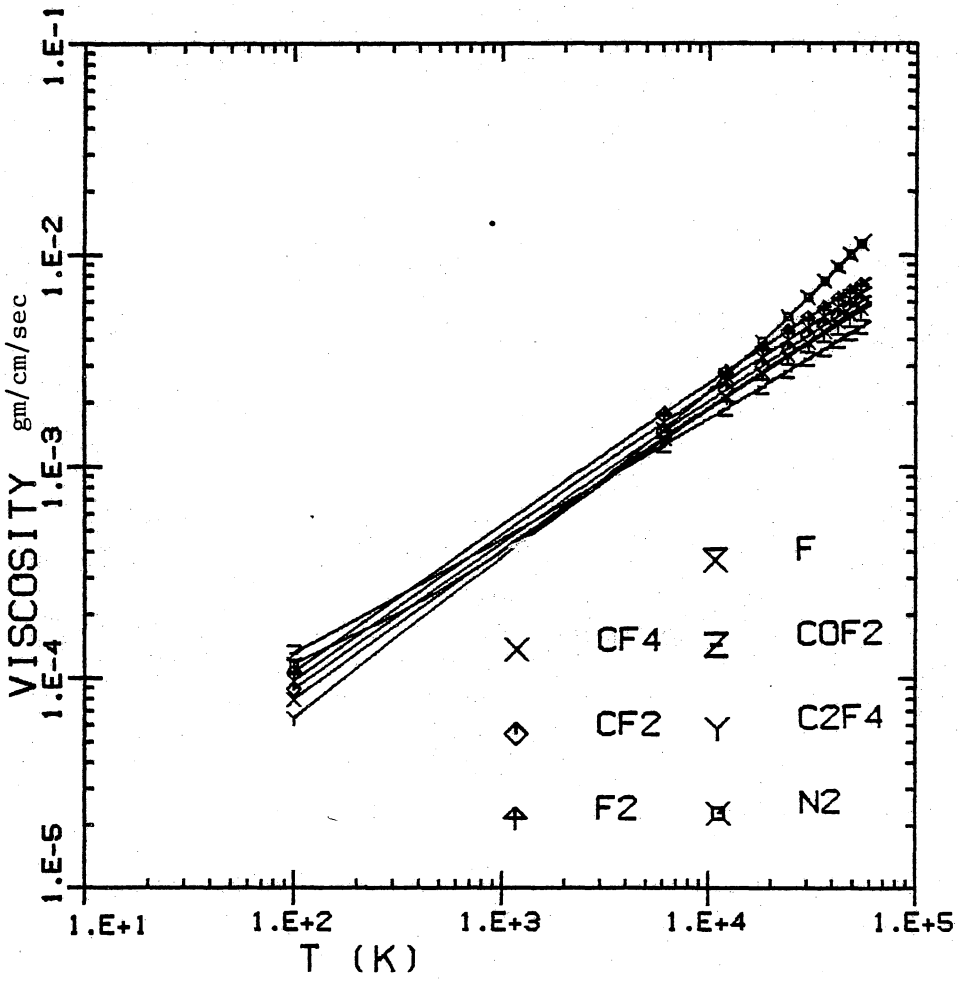

Figure 17. Viscosity of teflon ablation species CF_4, CF_2, F_2, F, COF_2, C_2F_4, N_2

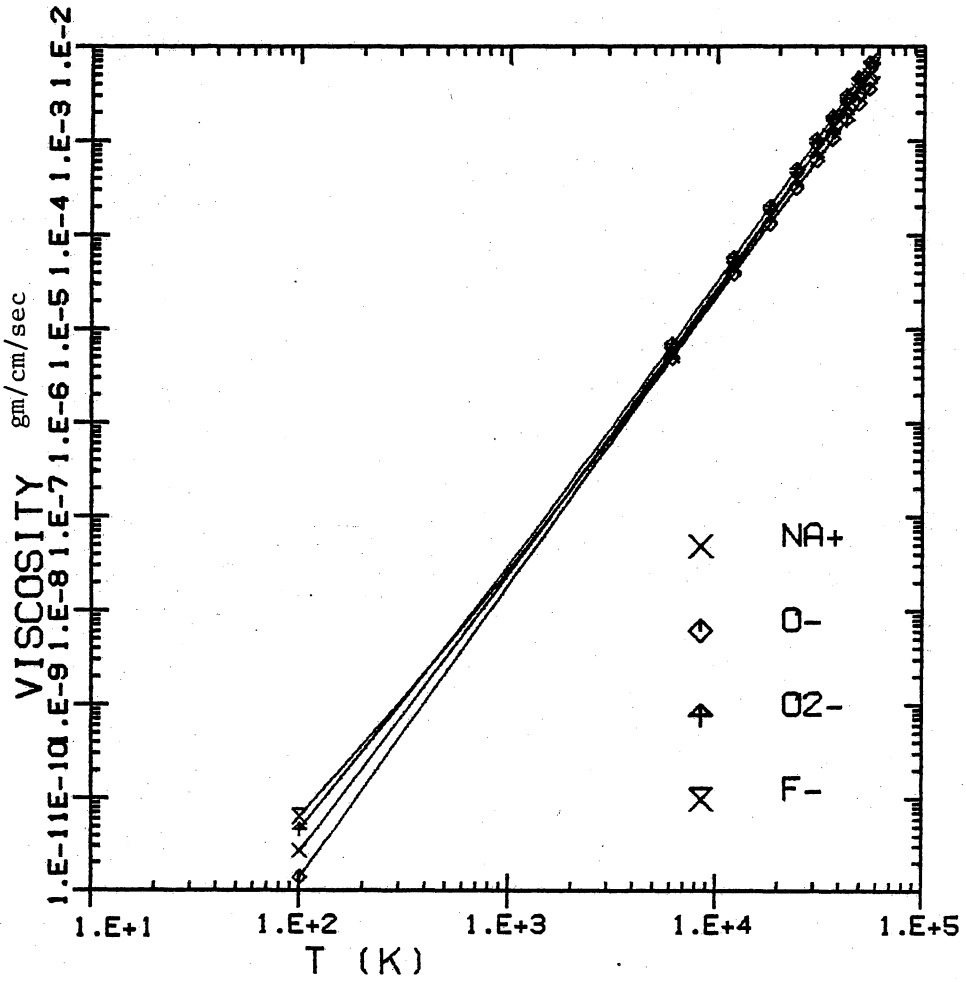

Figure 18. Viscosity of the ionized species Na^+, O^-, O_2^-, F^-

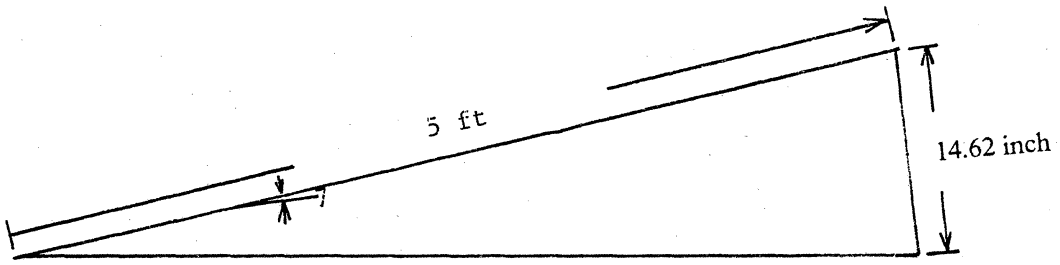

Fig. 19a. 7° cone with 5 ft slant length

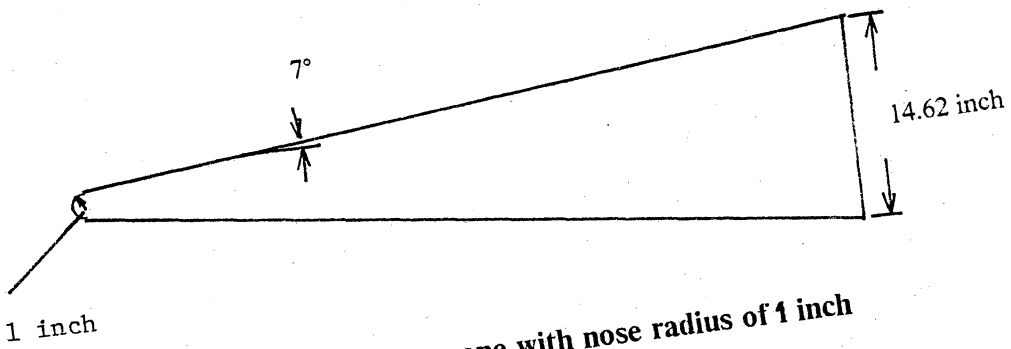

Fig. 19b. 7° sphere-cone with nose radius of 1 inch

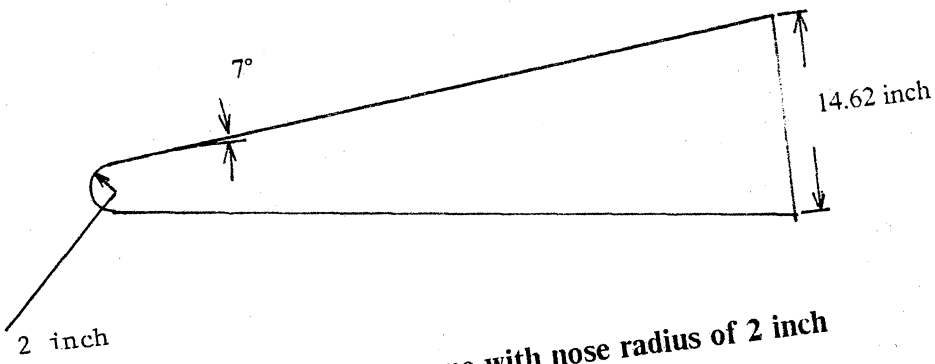

Fig. 19c. 7° sphere-cone with nose radius of 2 inch

Figure 19. Vehicle geometries

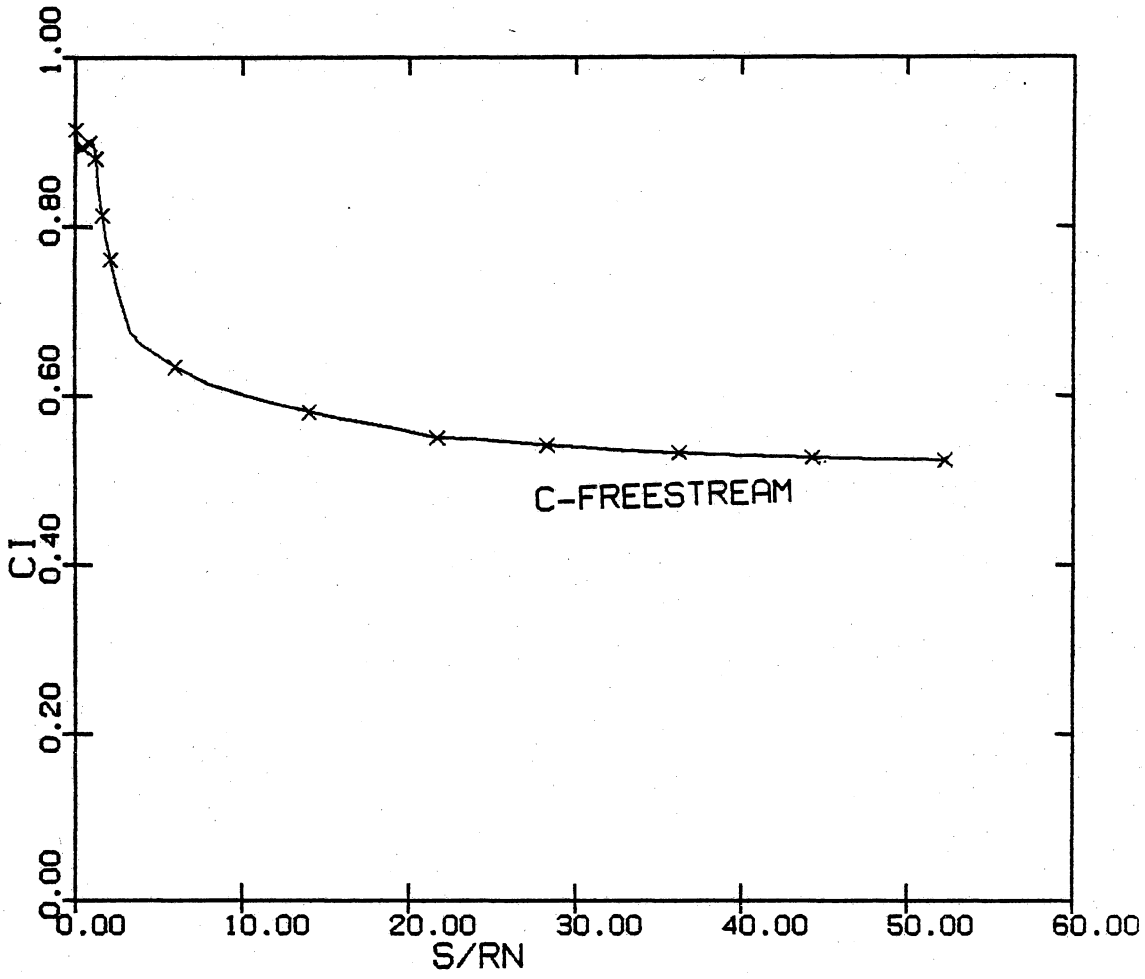

Figure 20. Freestream air concentration distribution at the wall along the body for case A.

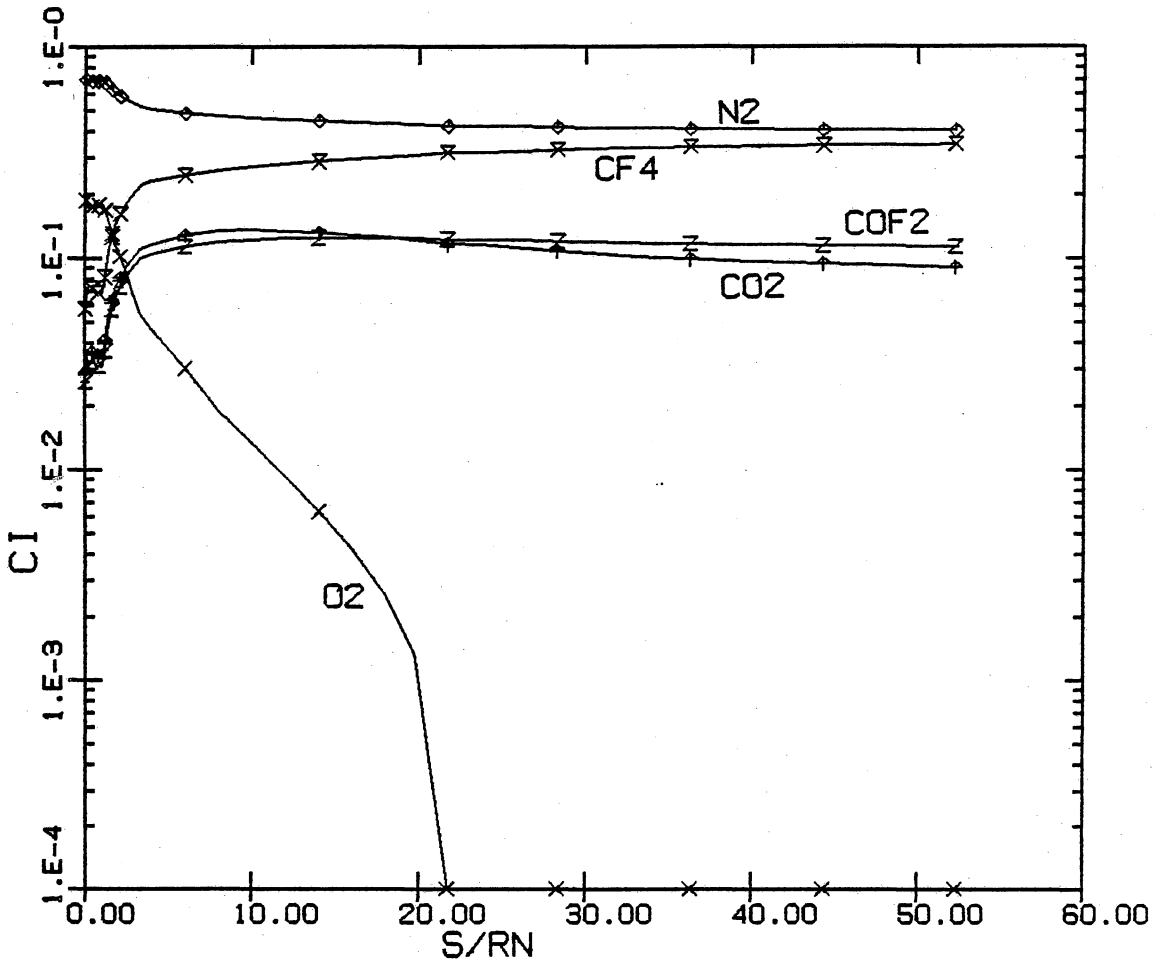

Figure 21. Equilibrium wall species concentration distribution along the body for case A.

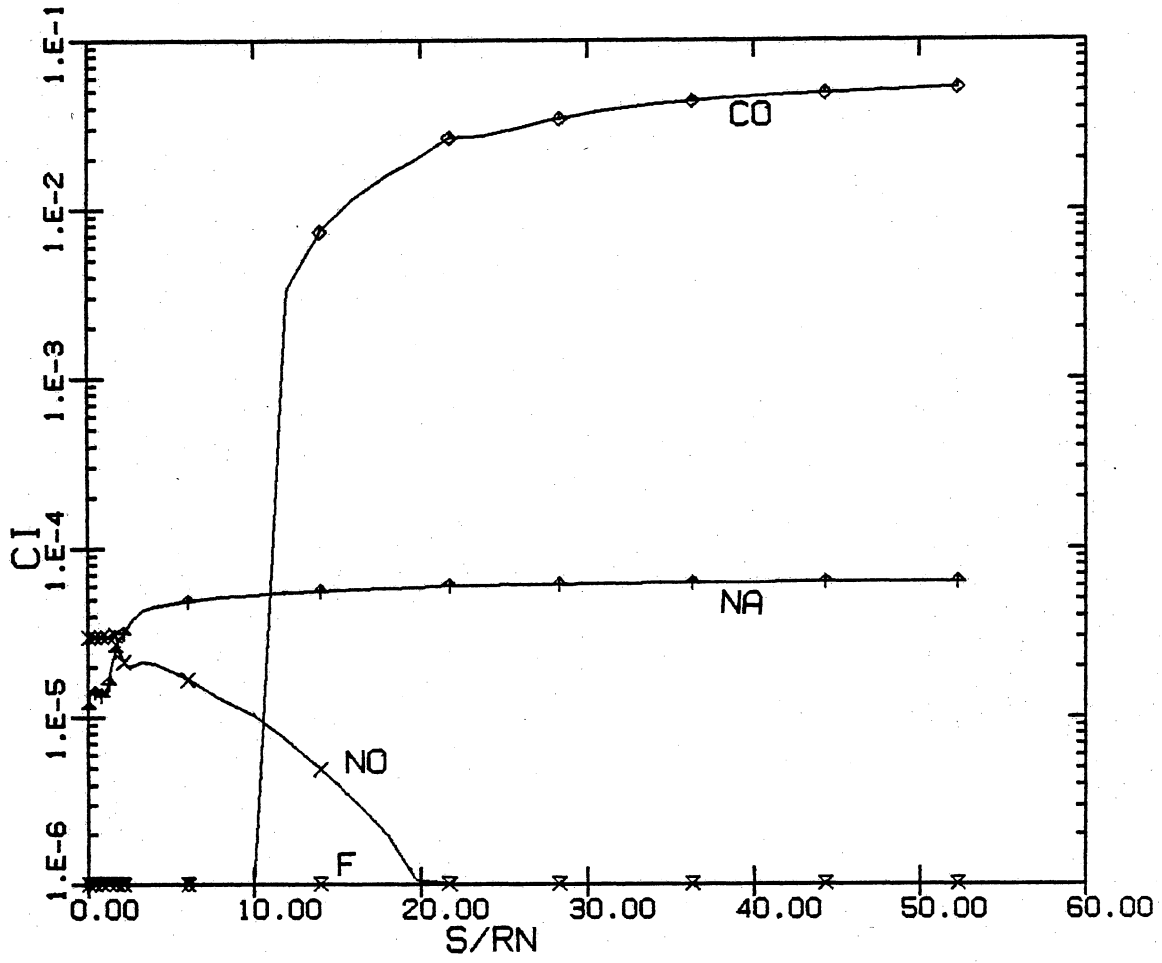

Figure 22. Equilibrium wall species concentration distribution along the body for case A.

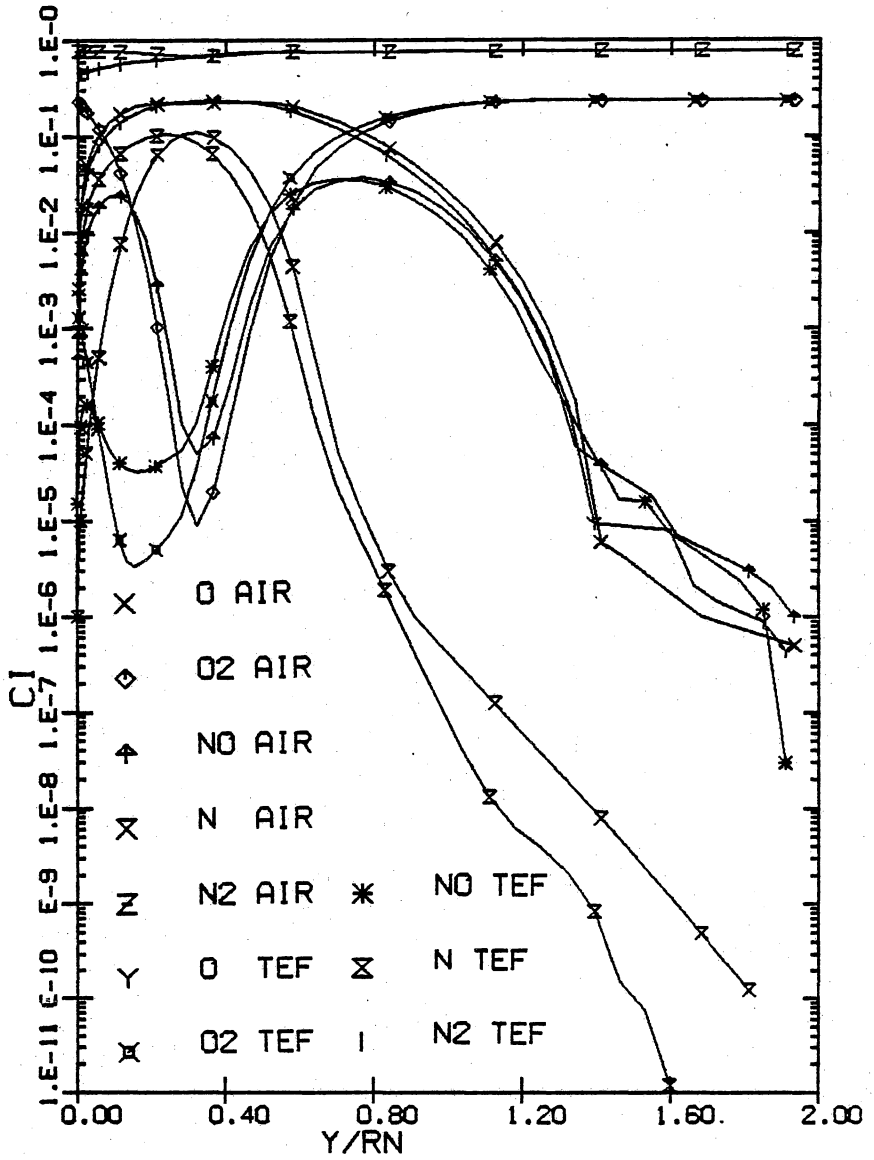

Figure 23. Nonequilibrium air species concentration comparison at s/Rn = 19.7 between the seven species code and the teflon code for case A.

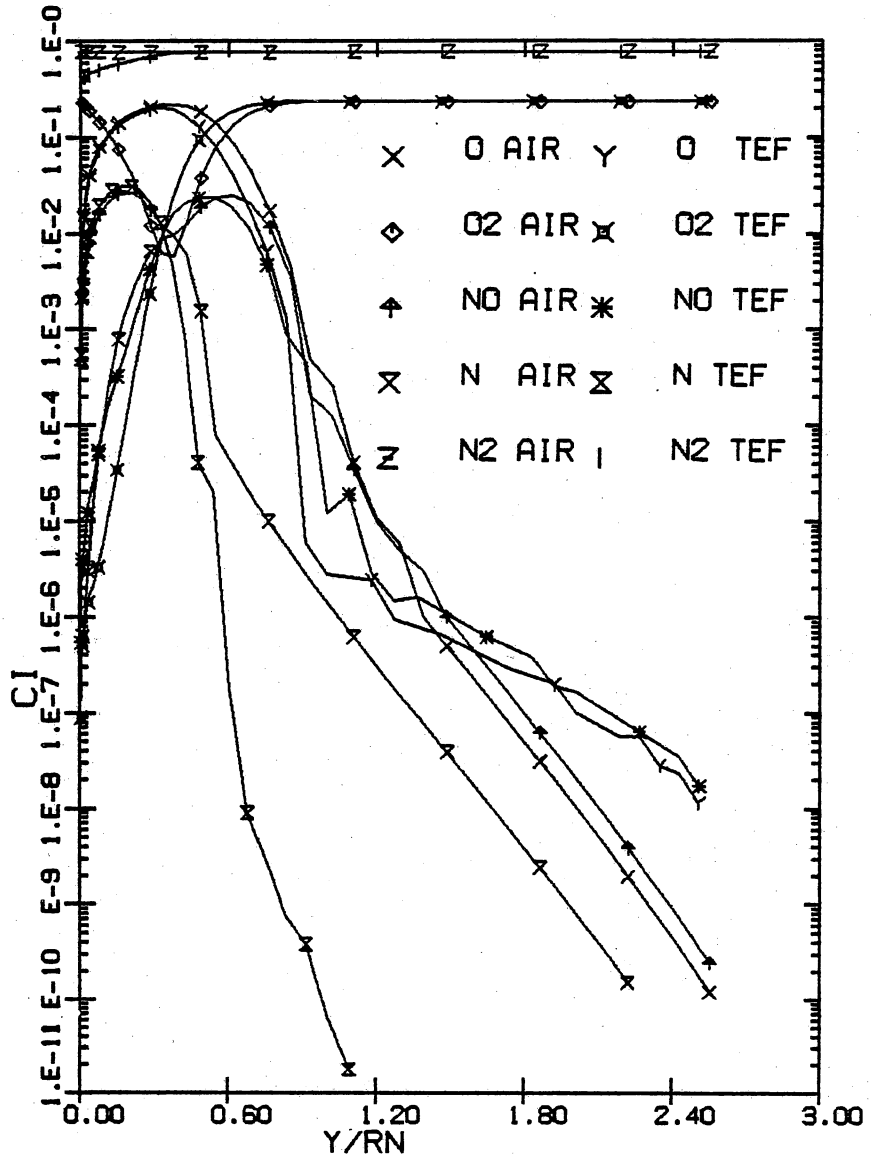

Figure 24. Nonequilibrium air species concentration comparison at s/Rn = 52.3 between the seven species code and the teflon code for case A.

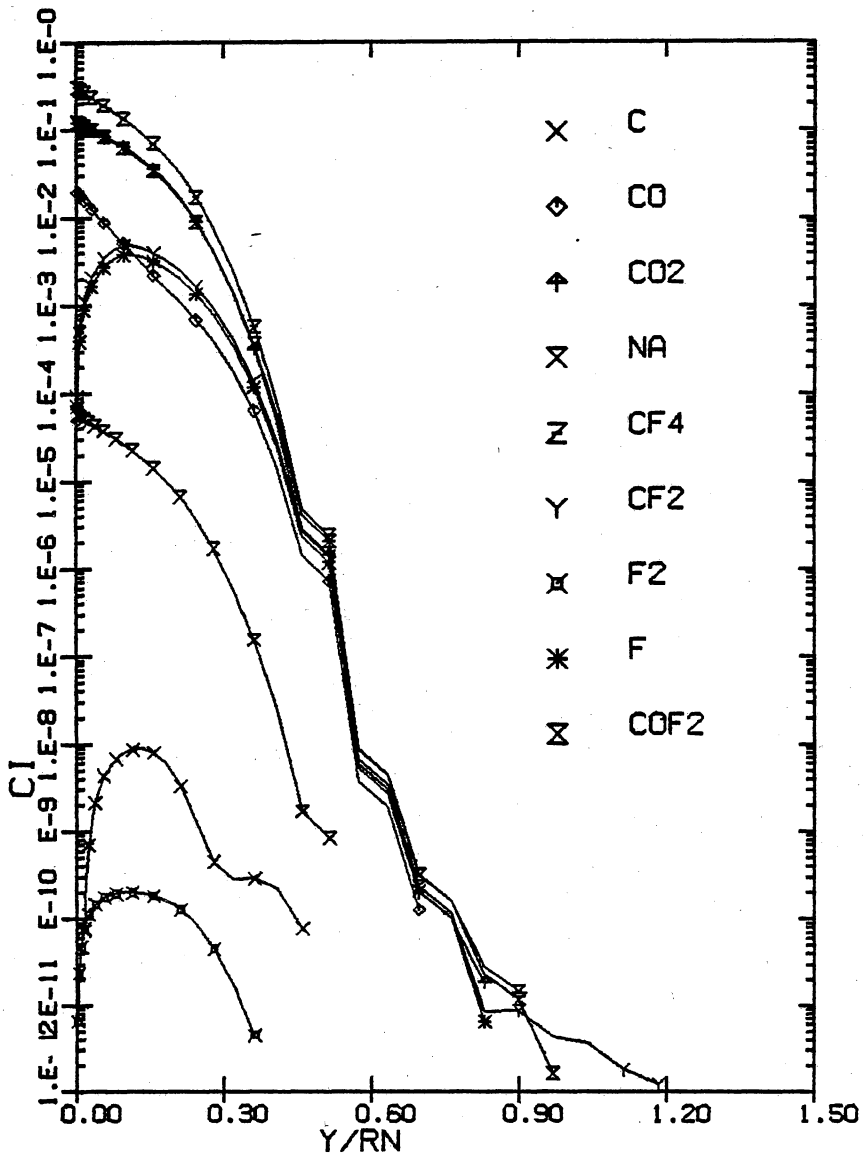

Figure 25. Teflon ablation species concentration comparison at s/Rn = 19.7 for case A.

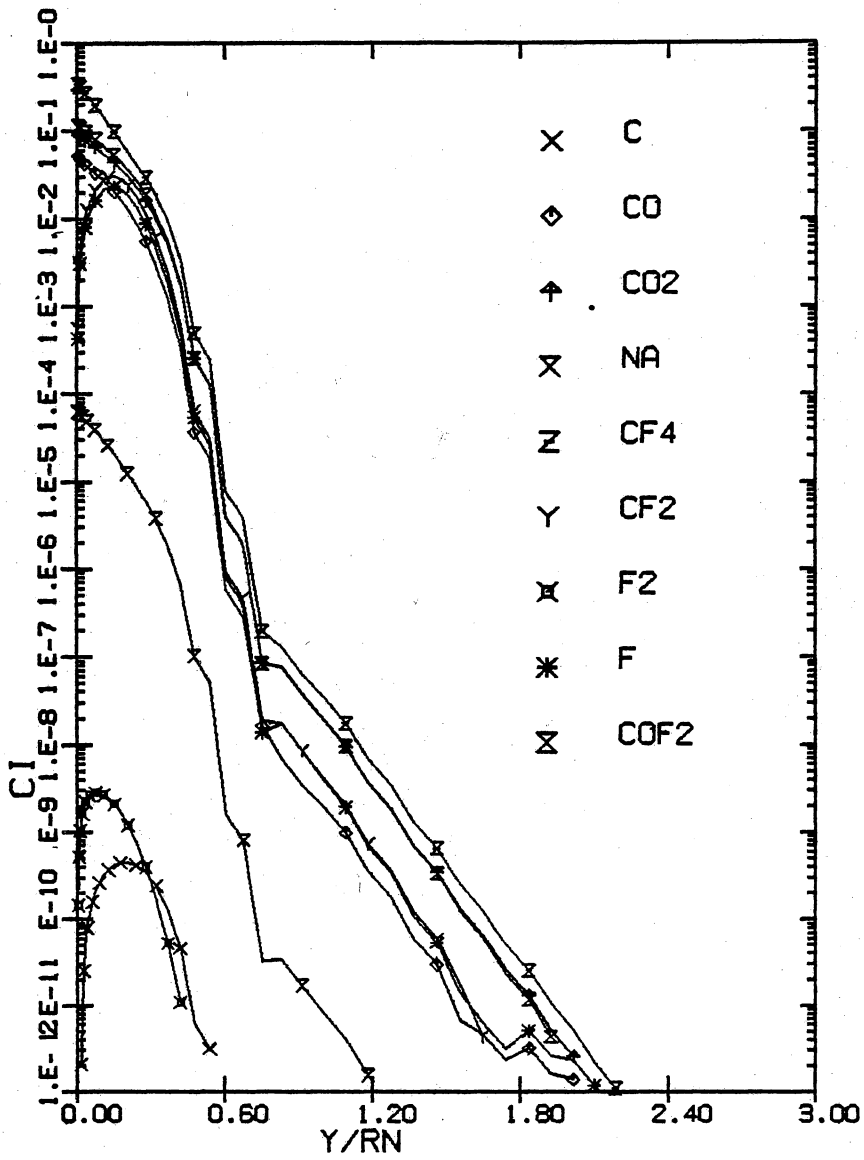

Figure 26. Teflon ablation species concentration comparison at s/Rn = 52.3 for case A.

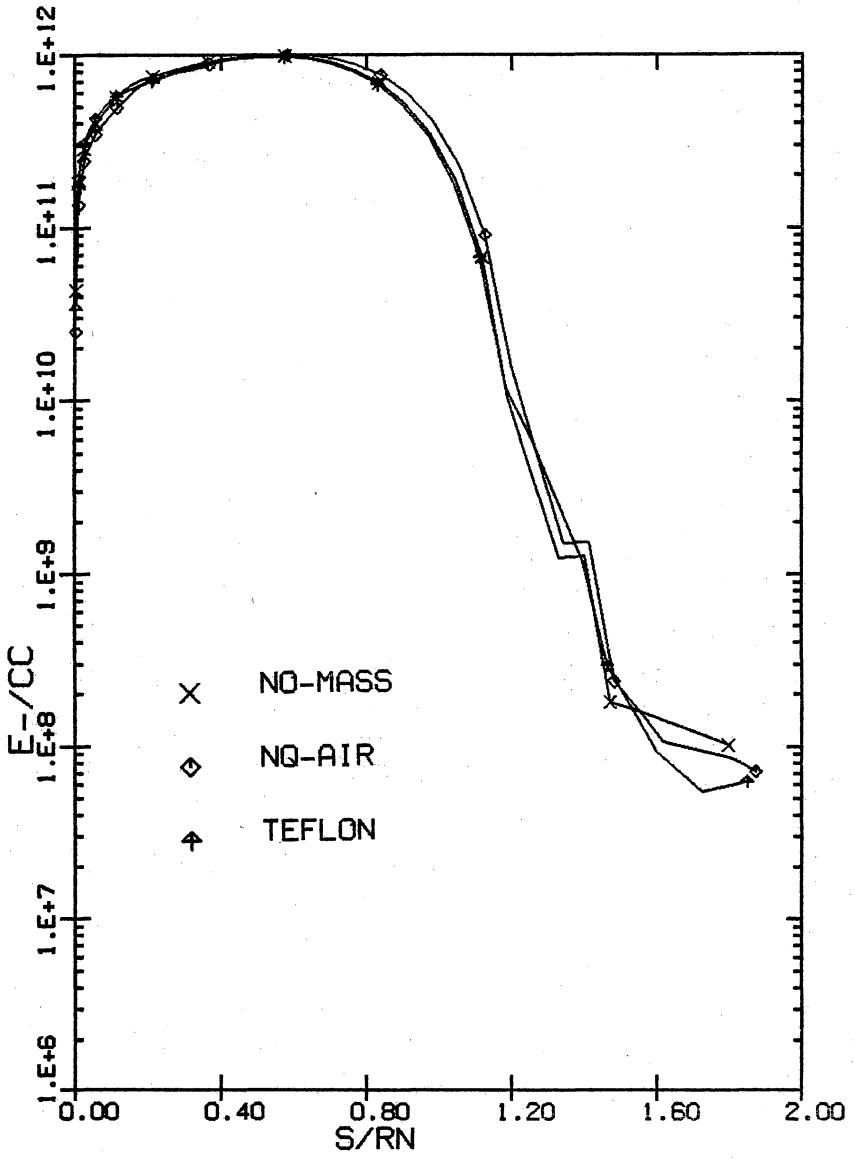

Figure 27. Electron number density comparison at s/Rn = 19.7 between the seven species code and the teflon code for case A.

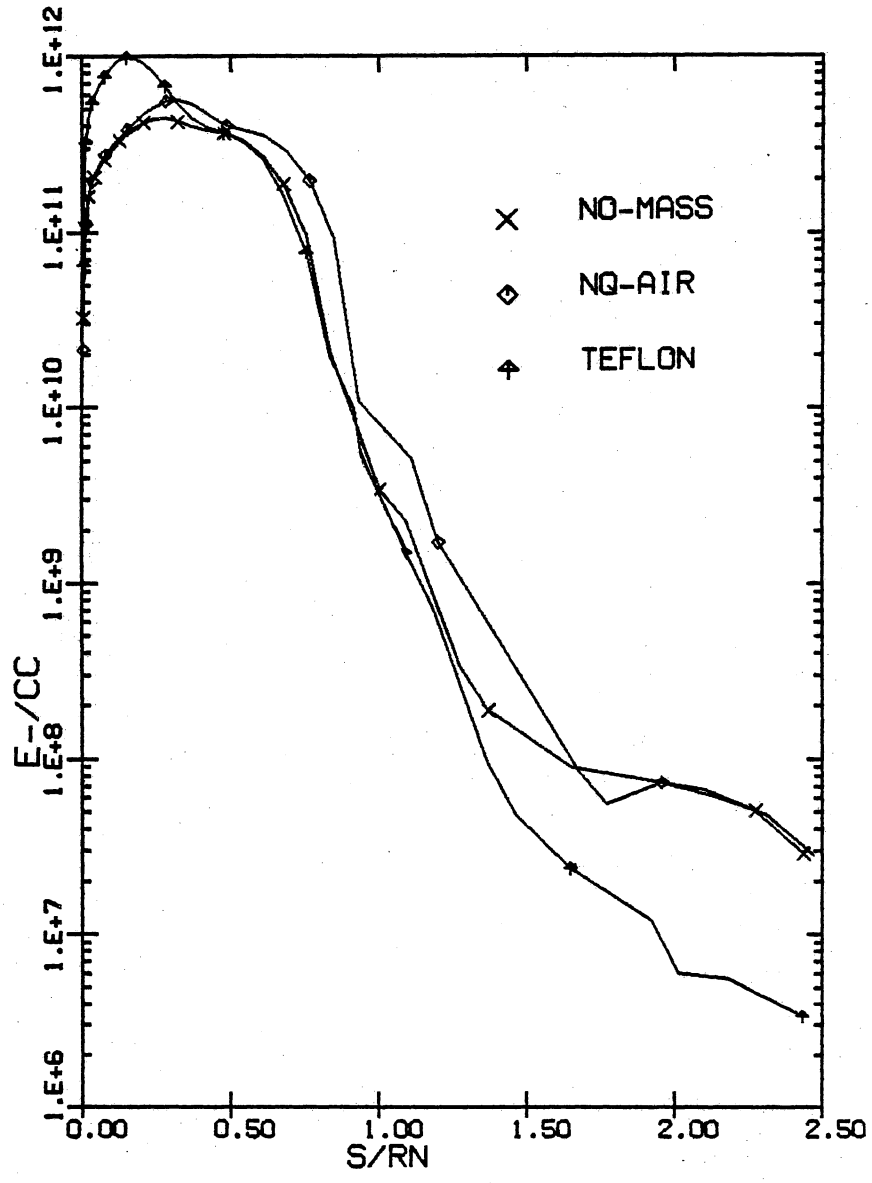

Figure 28. Electron number density comparison at s/Rn = 52.3 between the seven species code and the teflon code for case A.

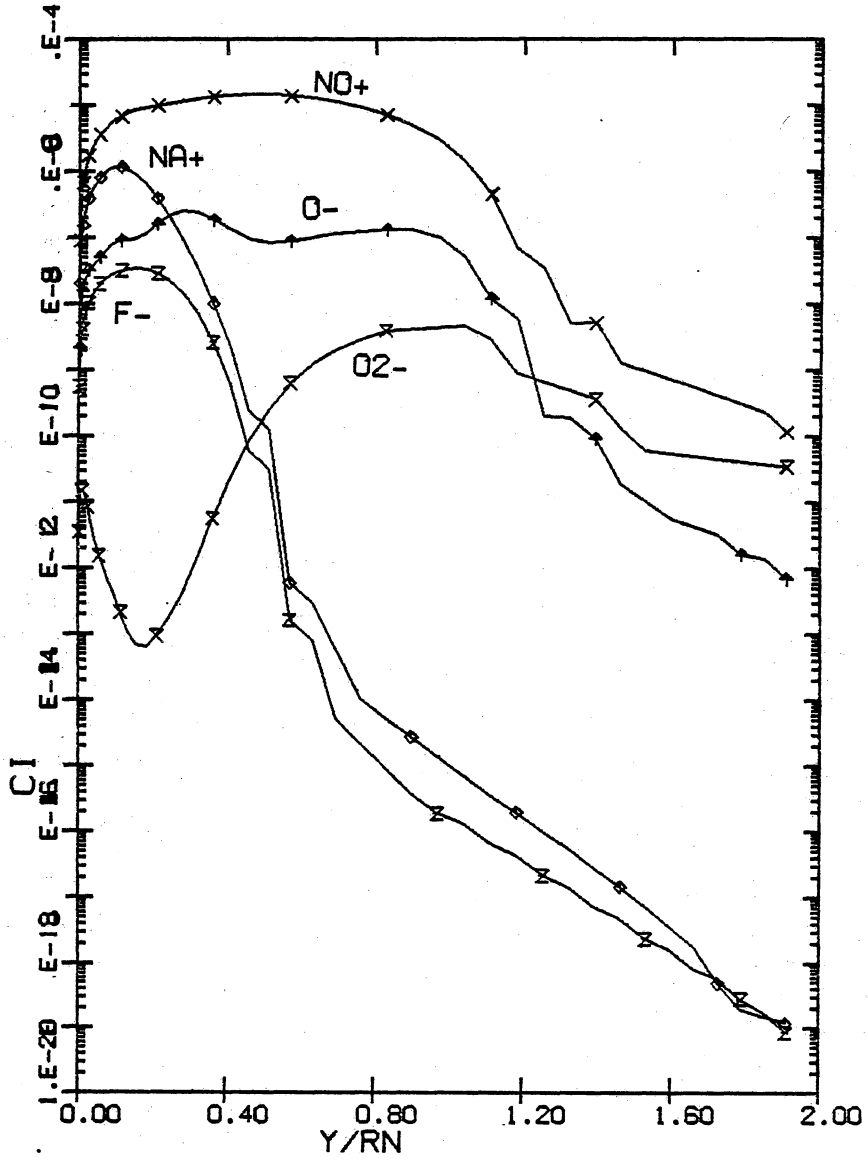

Figure 29. Ionized species concentration profiles at s/Rn = 19.7 for case A.

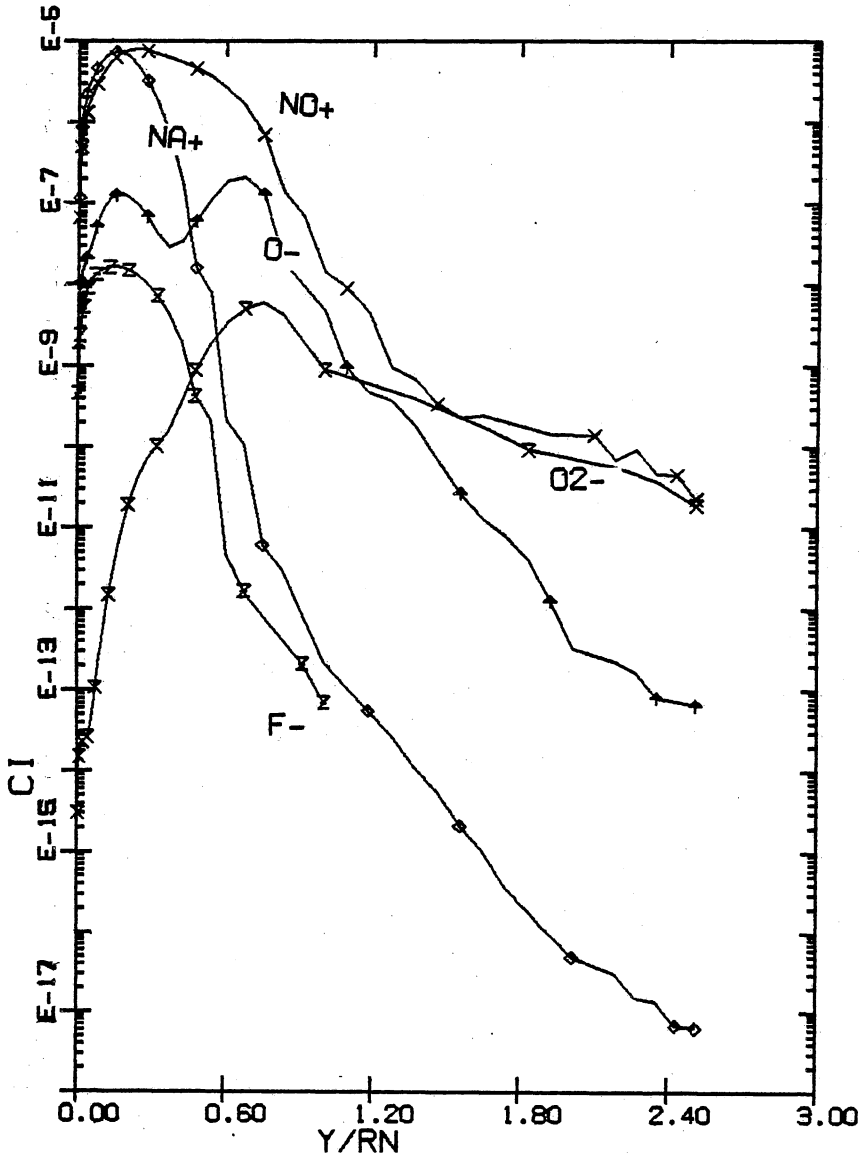

Figure 30. Ionized species concentraton profiles at s/Rn = 52.3 for case A.

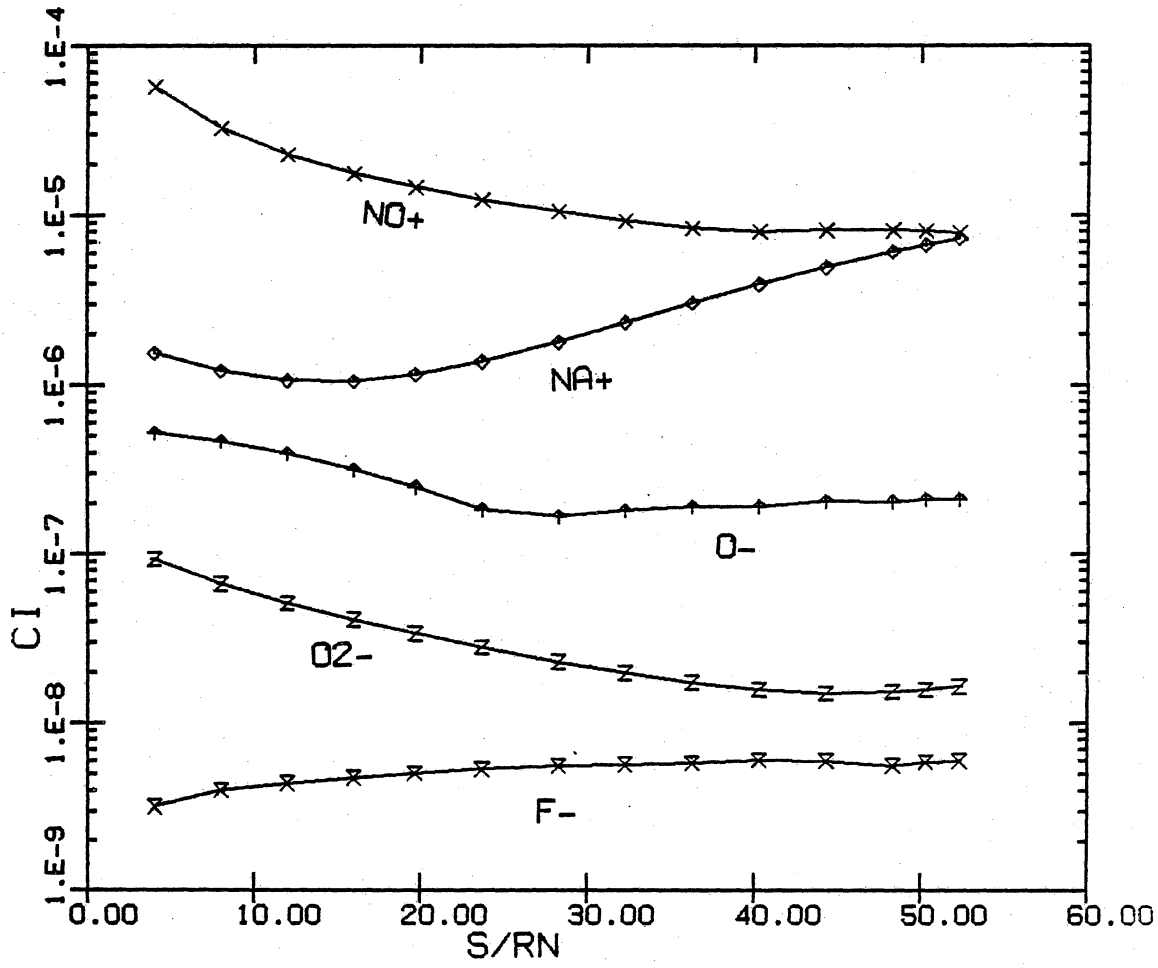

Figure 31. Peak concentration distribution of the ionized species along the body for case A.

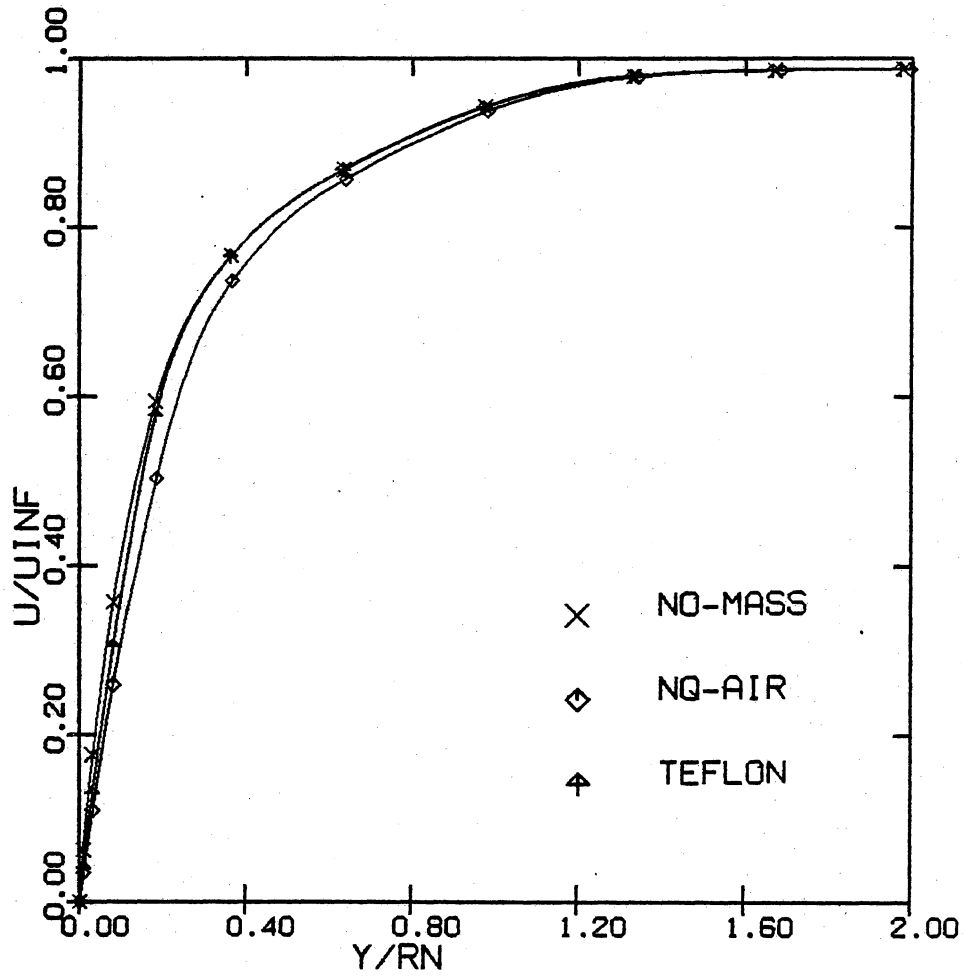

Figure 32. Streamwise velocity profile comparison at s/Rn = 19.7 between the seven species code and the teflon code for case A.

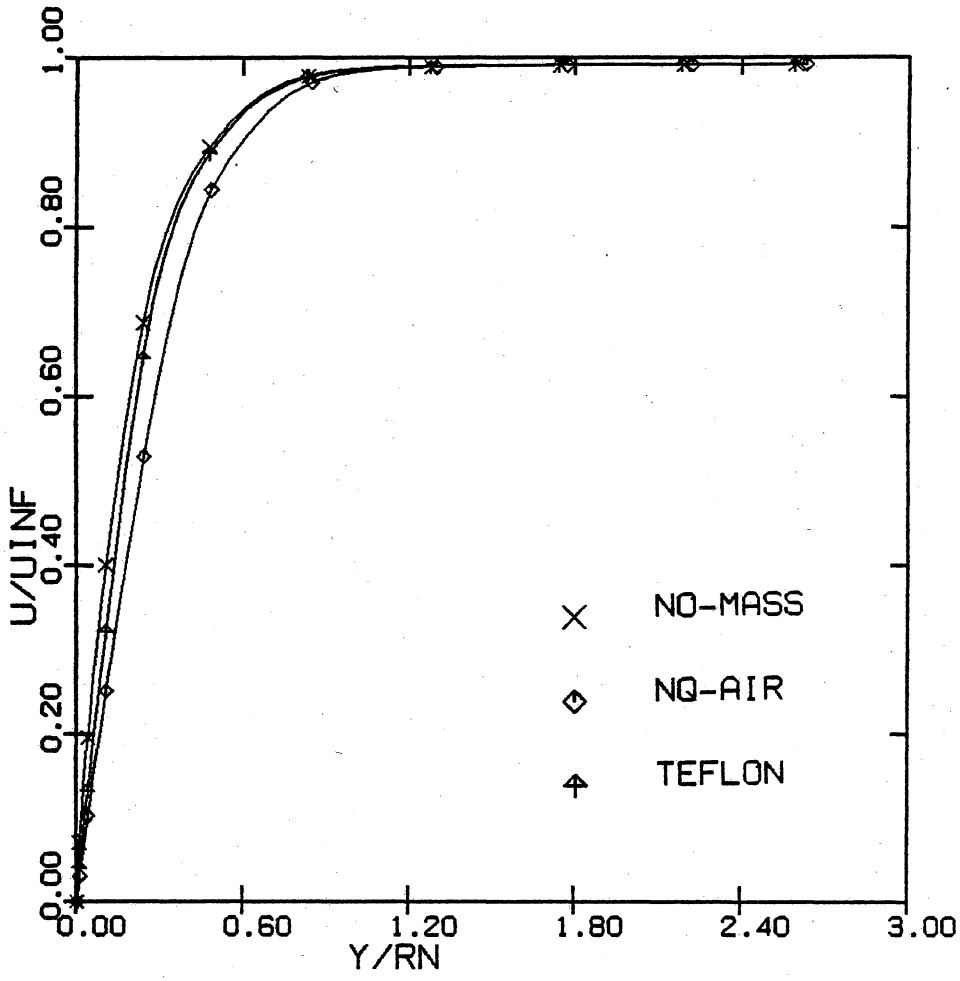

Figure 33. Streamwise velocity profile comparison at s/Rn = 52.3 between the seven species code and the teflon code for case A.

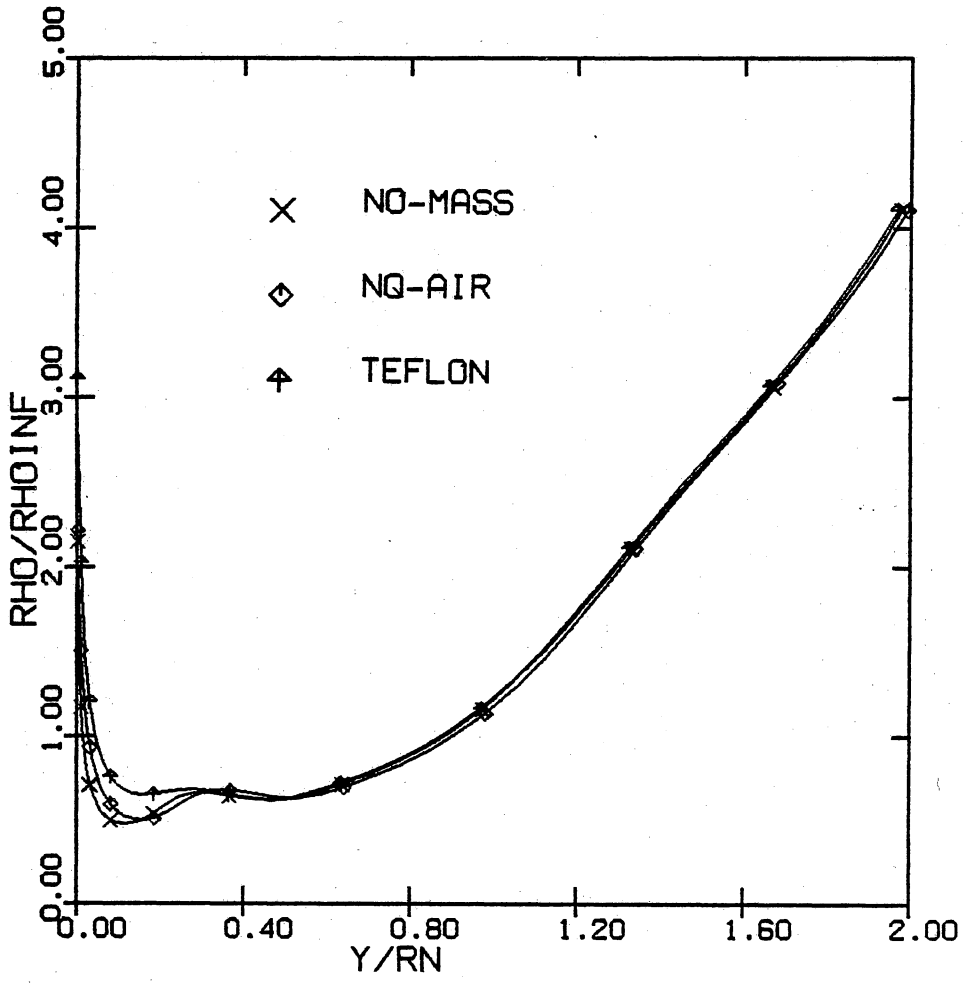

Figure 34. Density profile comparison at s/Rn = 19.7 between the seven species code and the teflon code for case A.

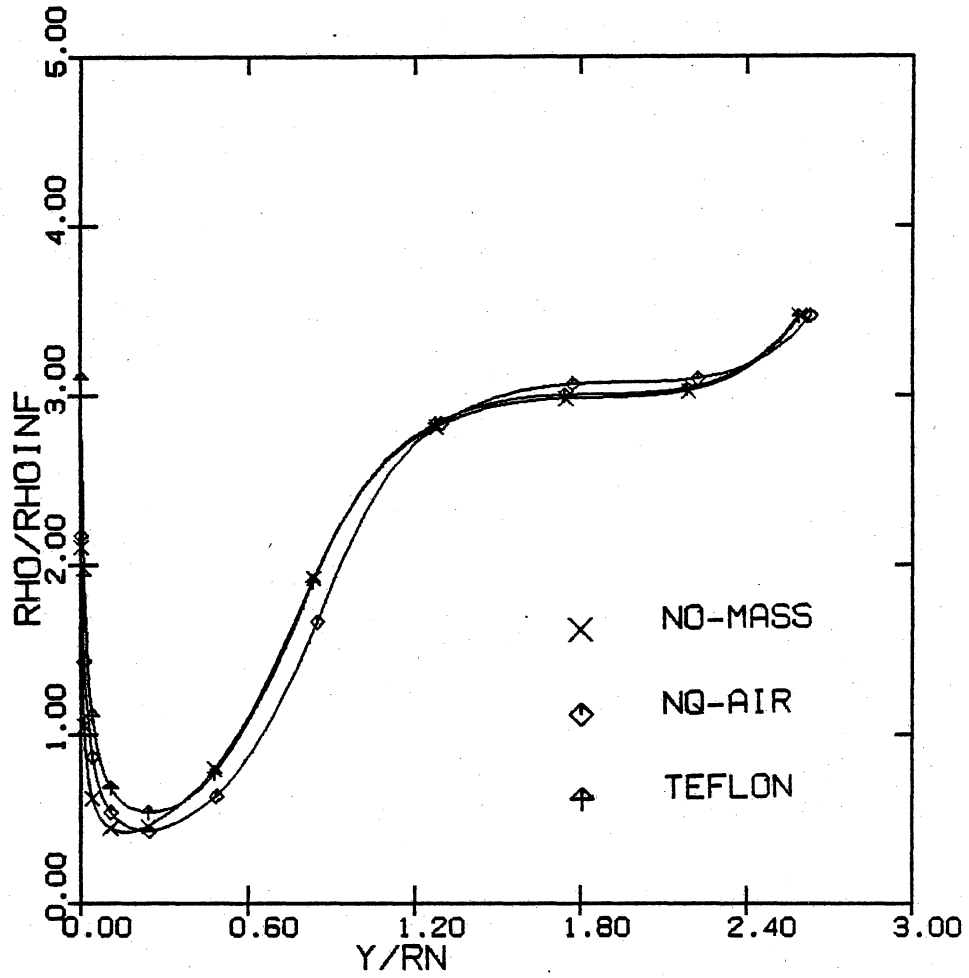

Figure 35. Density profile comparison at s/Rn = 52.3 between the seven species code and the teflon code for case A.

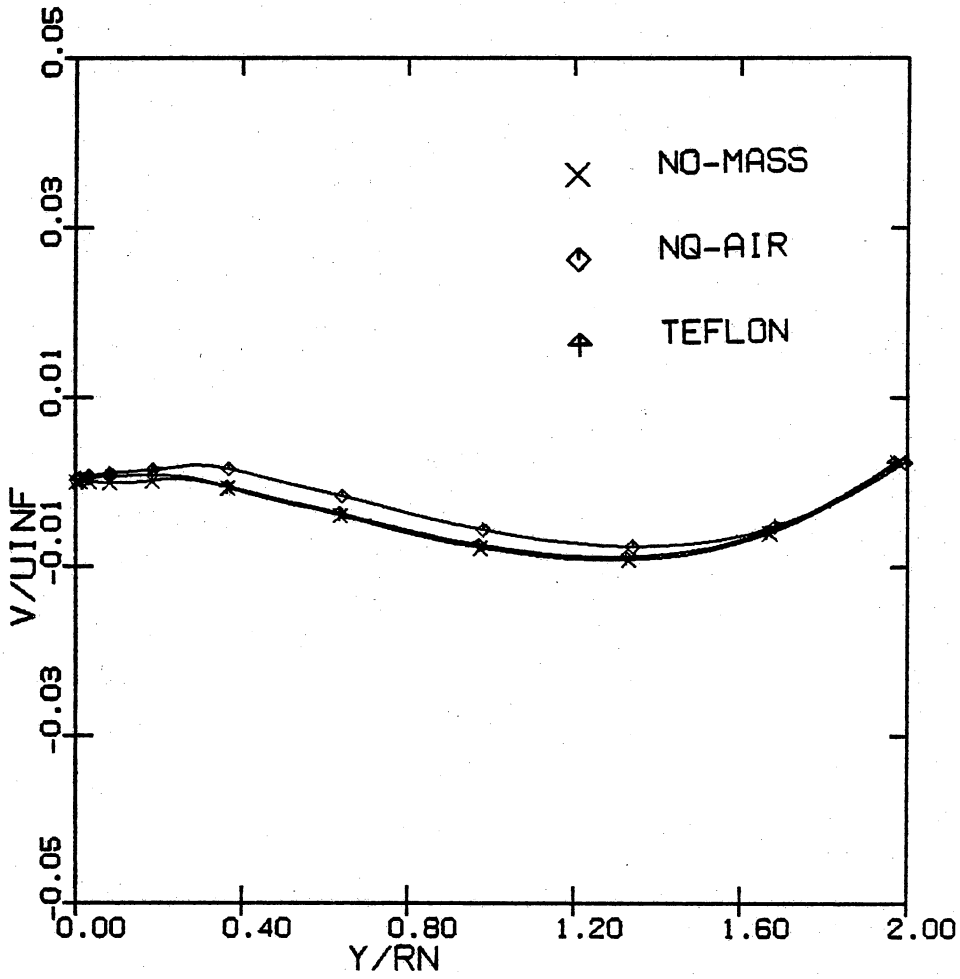

Figure 36. Normal velocity profile comparison at s/Rn = 19.7 between the seven species code and the teflon code for case A.

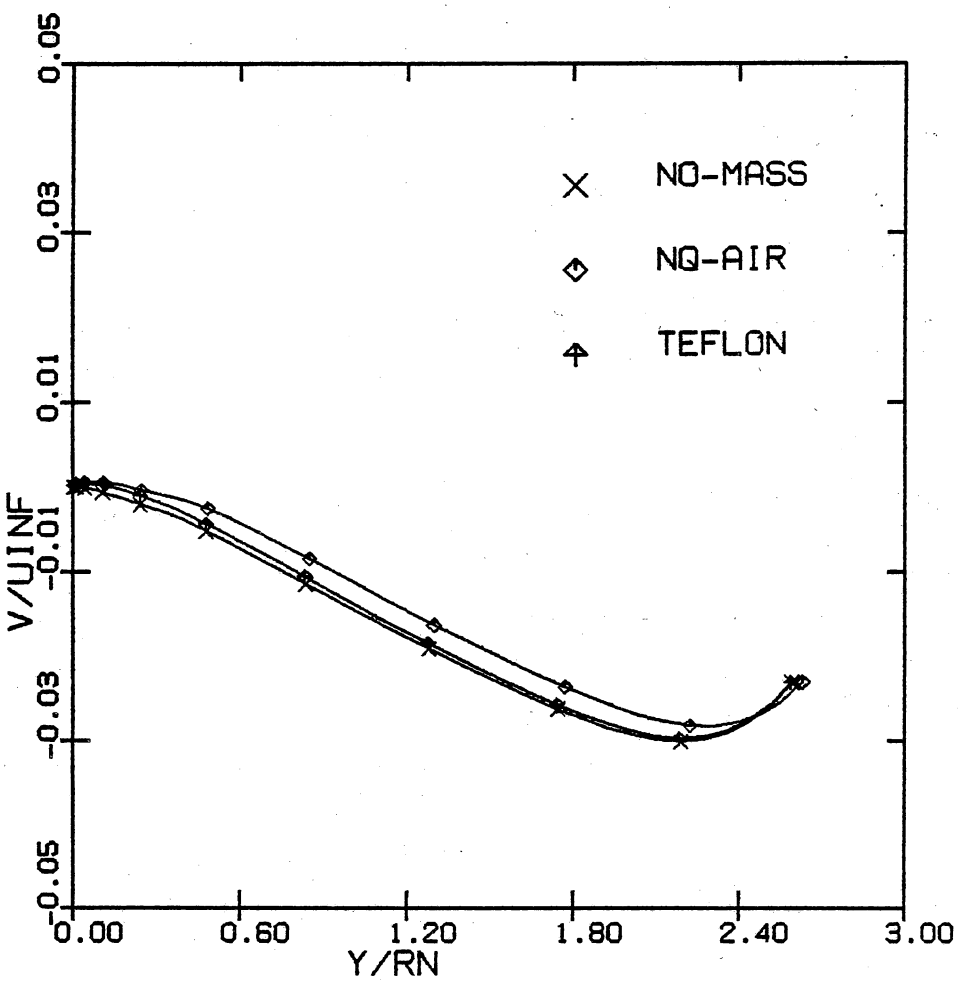

Figure 37. Normal velocity profile comparison at s/Rn = 52.3 between the seven species code and the teflon code for case A.

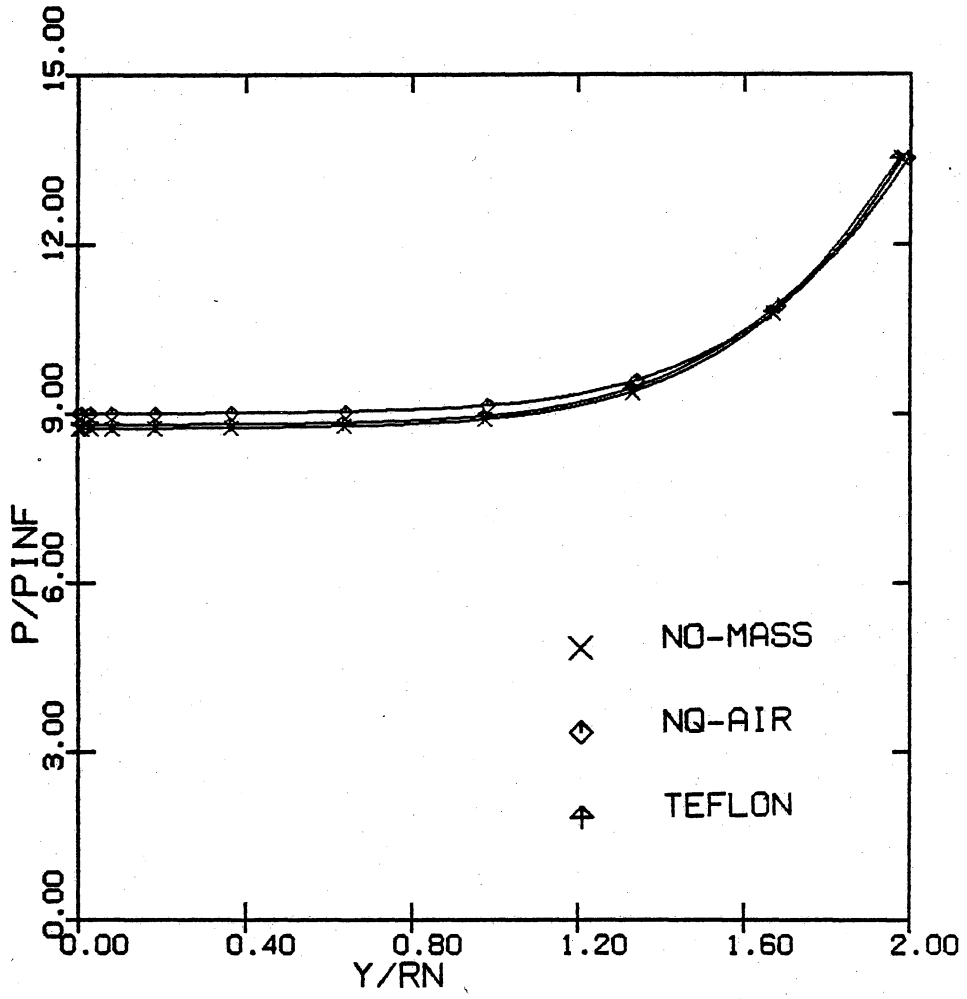

Figure 38. Pressure profile comparison at s/Rn = 19.7 between the seven species code and the teflon code for case A.

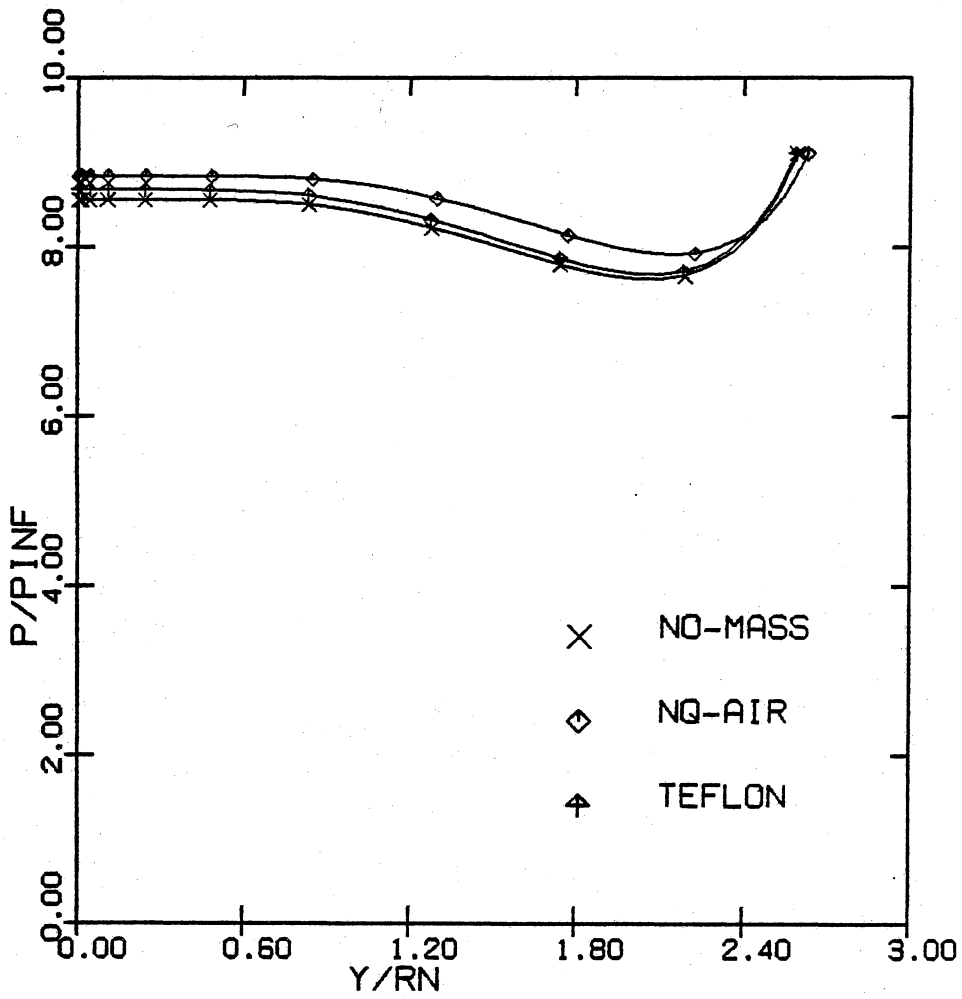

Figure 39. Pressure profile comparison at s/Rn = 52.3 between the seven species code and the teflon code for case A.

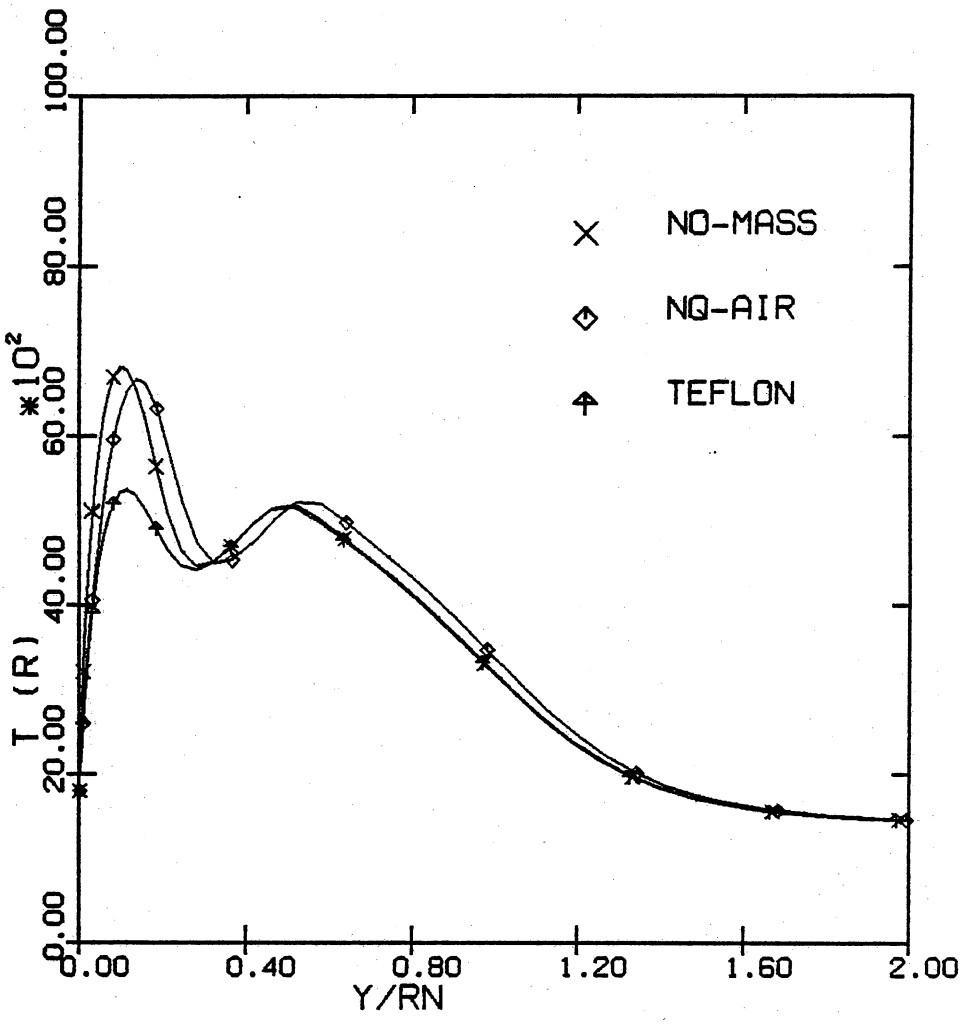

Figure 40. Temperature profile comparison at s/Rn = 19.7 between the seven species code and the teflon code for case A.

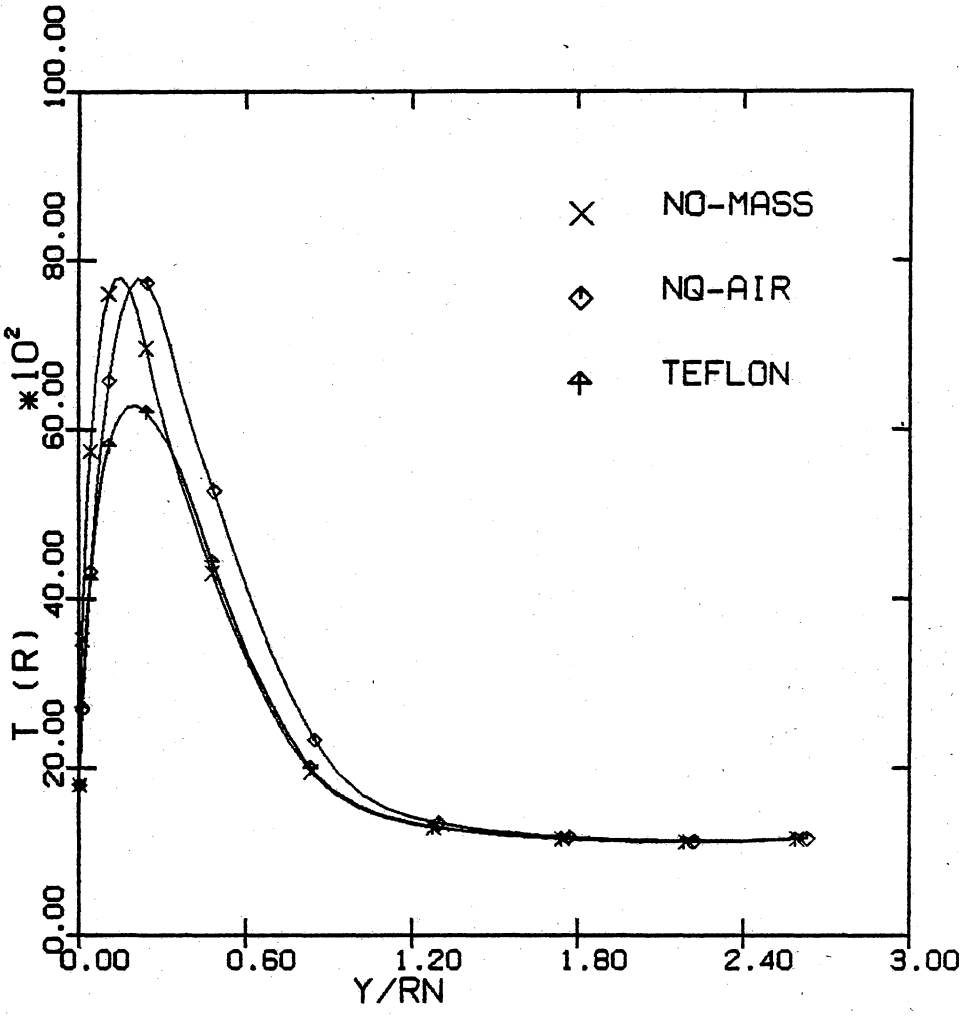

Figure 41. Temperature profile comparison at s/Rn = 52.3 between the seven species code and the teflon code for case A.

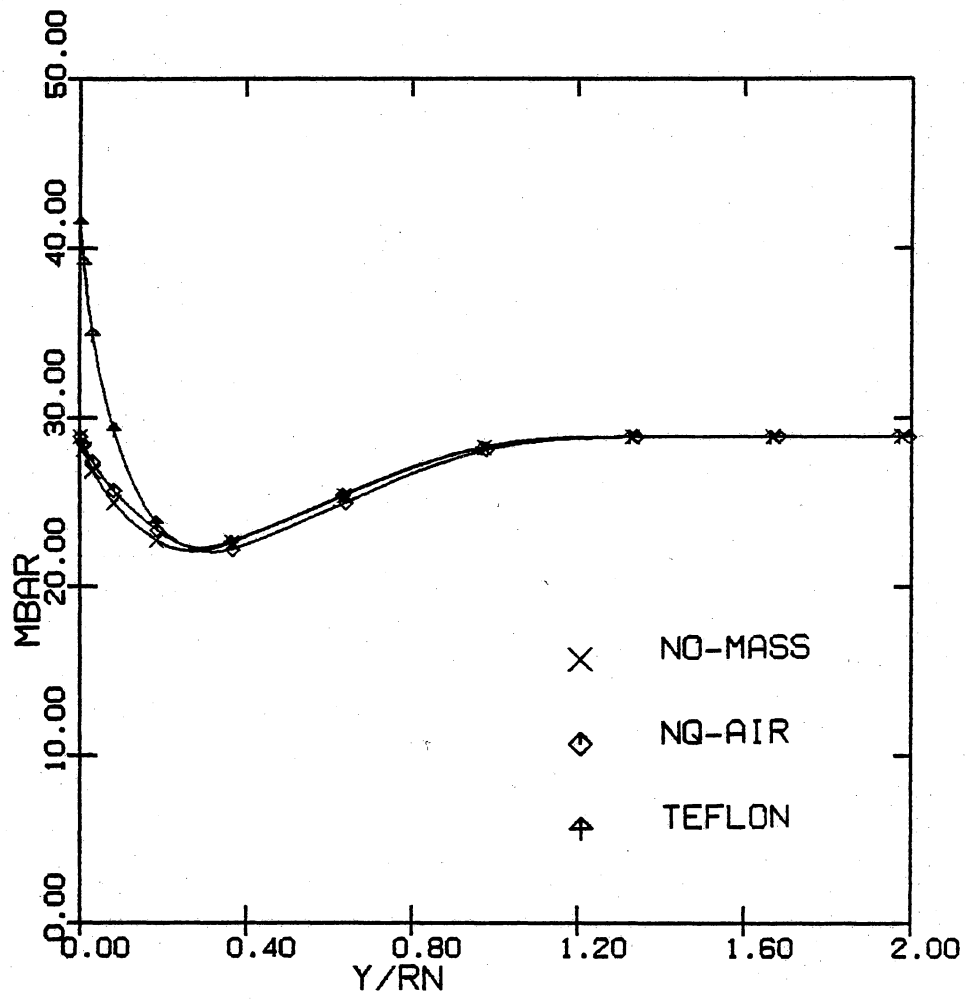

Figure 42. Average molecular weight profile comparison at s/Rn = 19.7 between the seven species code and the teflon code for case A.

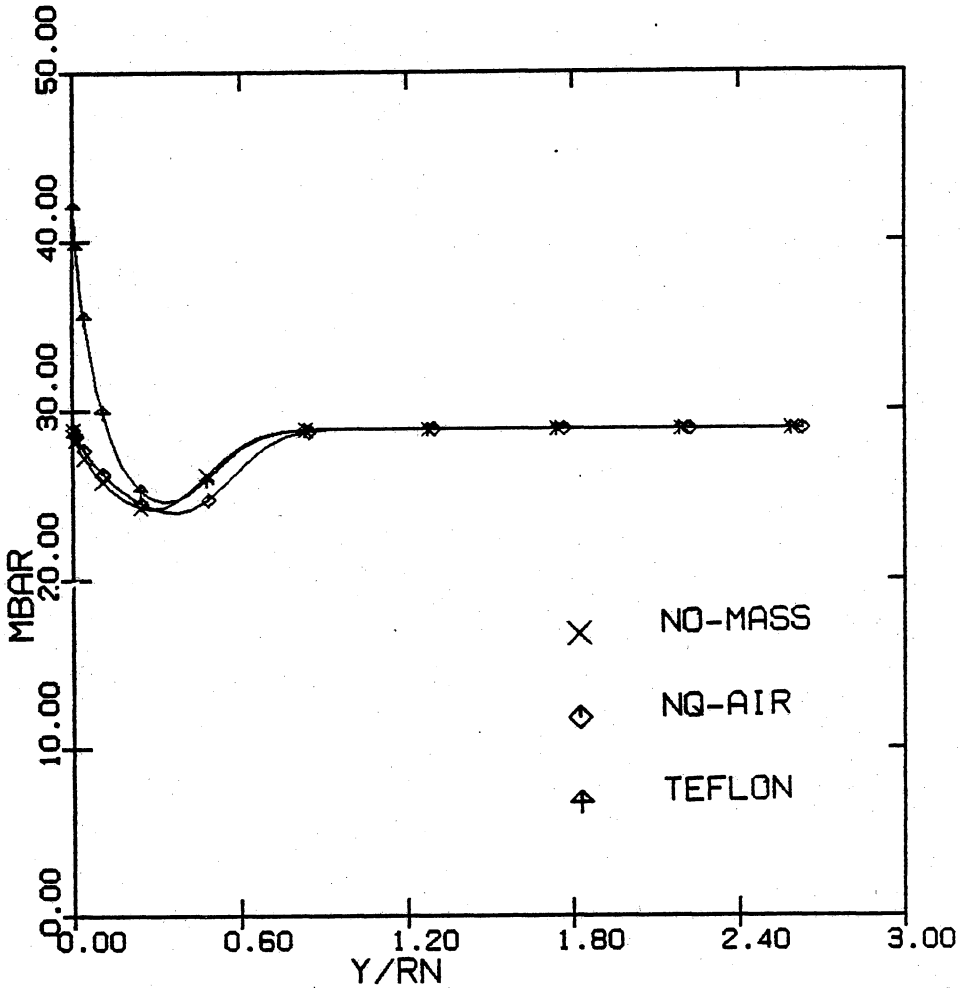

Figure 43. Average molecular weight profile comparison at s/Rn = 52.3 between the seven species code and the teflon code for case A.

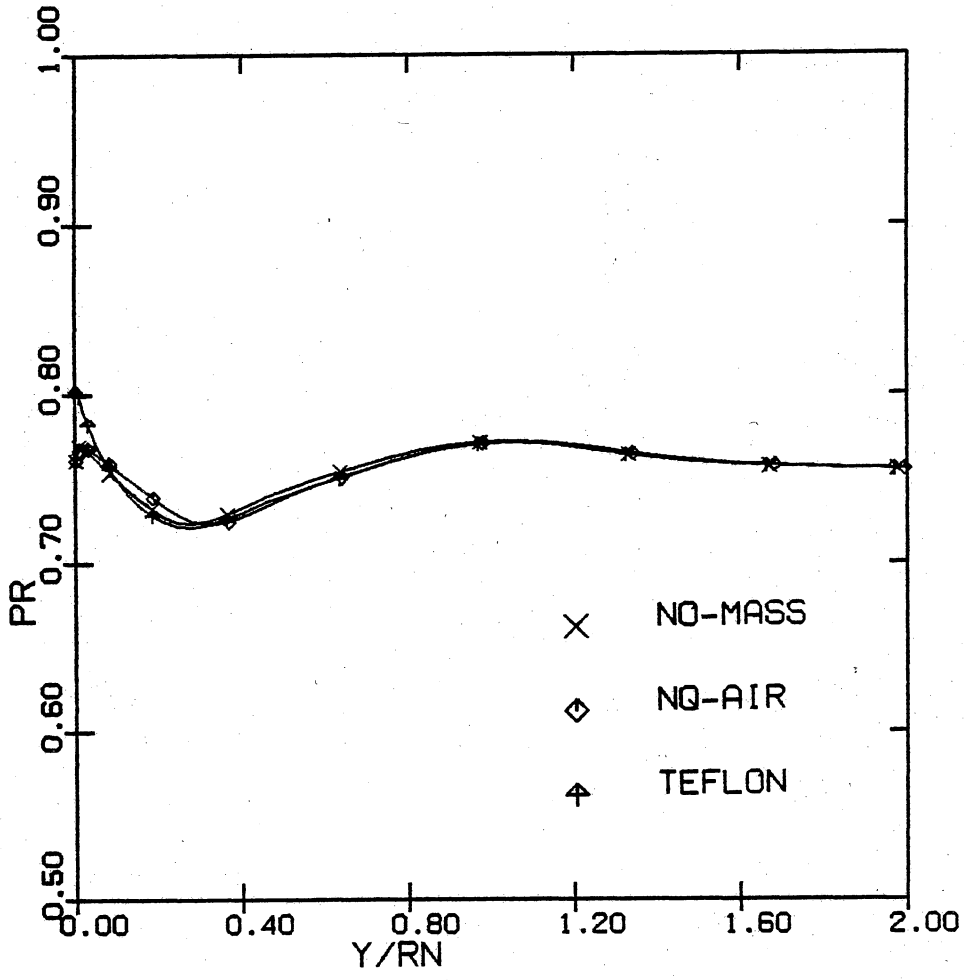

Figure 44. Prandtl No. profile comparison at s/Rn = 19.7 between the seven species code and the teflon code for case A.

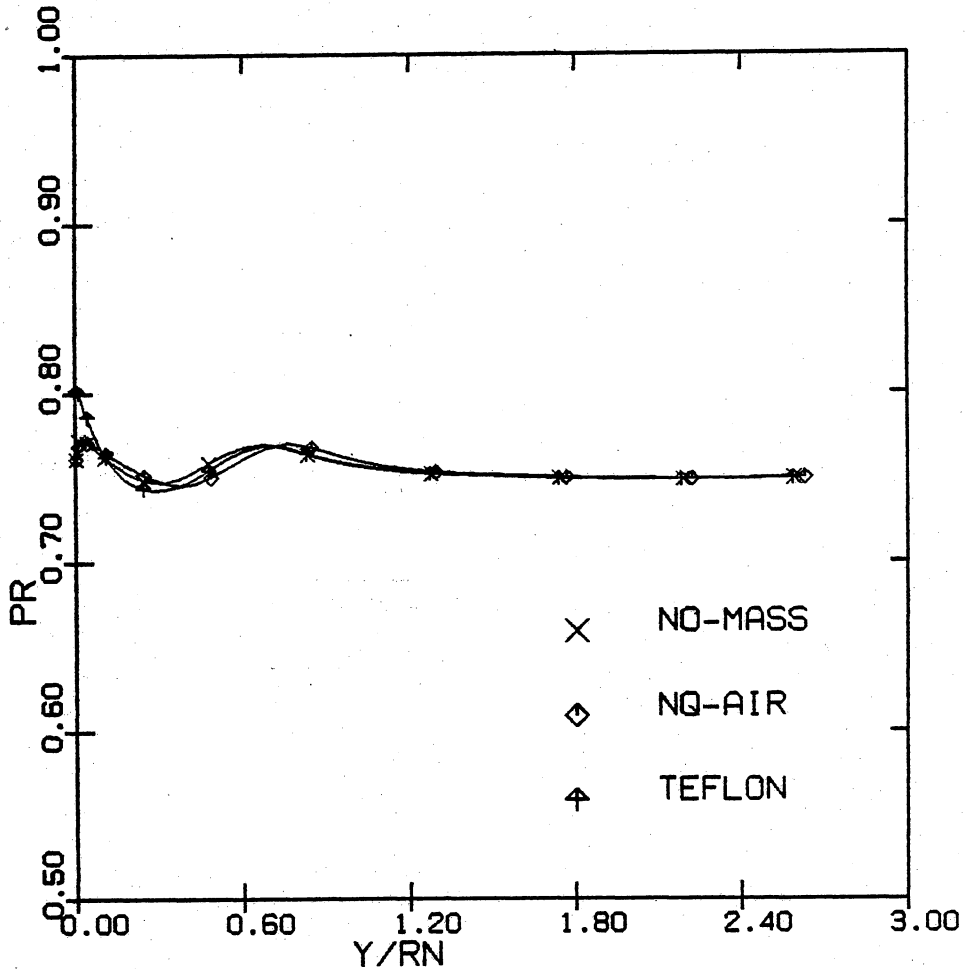

Figure 45. Prandtl No. profile comparison at s/Rn = 52.3 between the seven species code and the teflon code for case A.

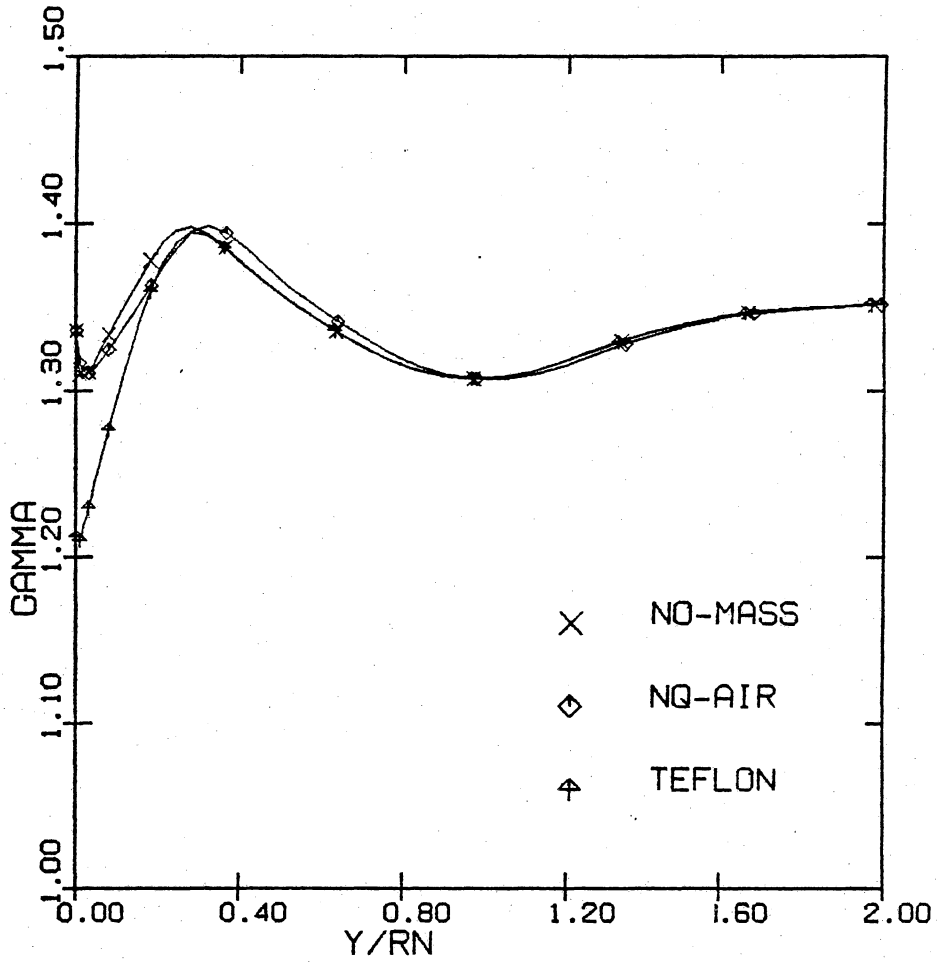

Figure 46. Specific heat ratio profile comparison at s/Rn = 19.7 between the seven species code and the teflon code for case A.

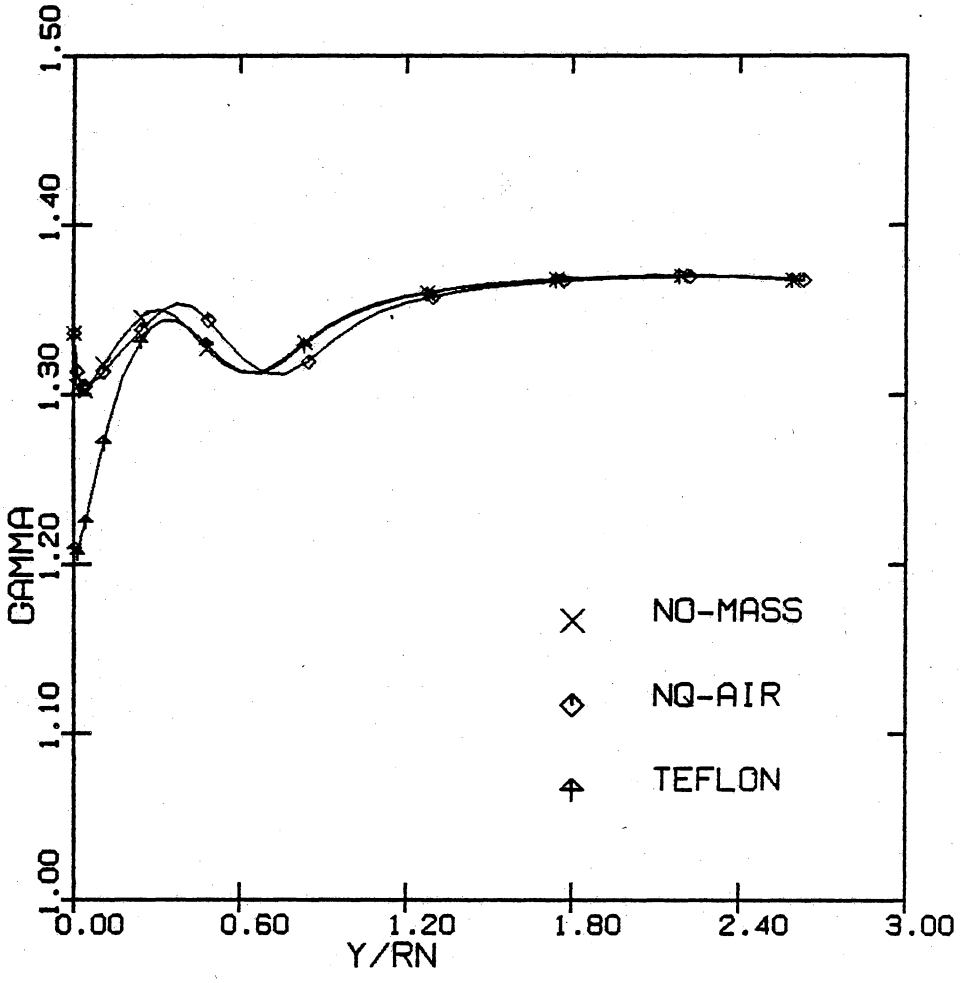

Figure 47. Specific heat ratio profile comparison at s/Rn = 52.3 between the seven species code and the teflon code for case A.

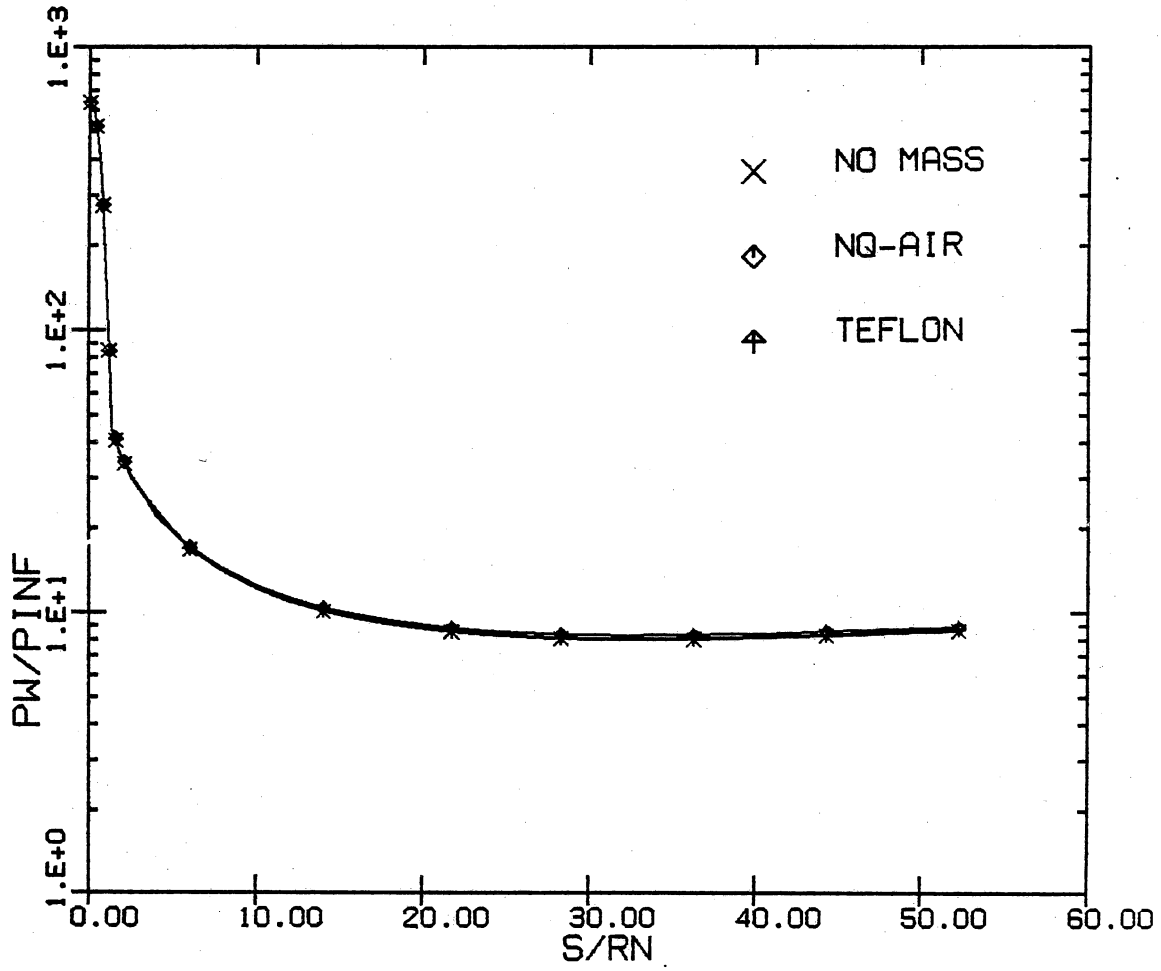

Figure 48. Wall pressure distribution comparison along the body for case A.

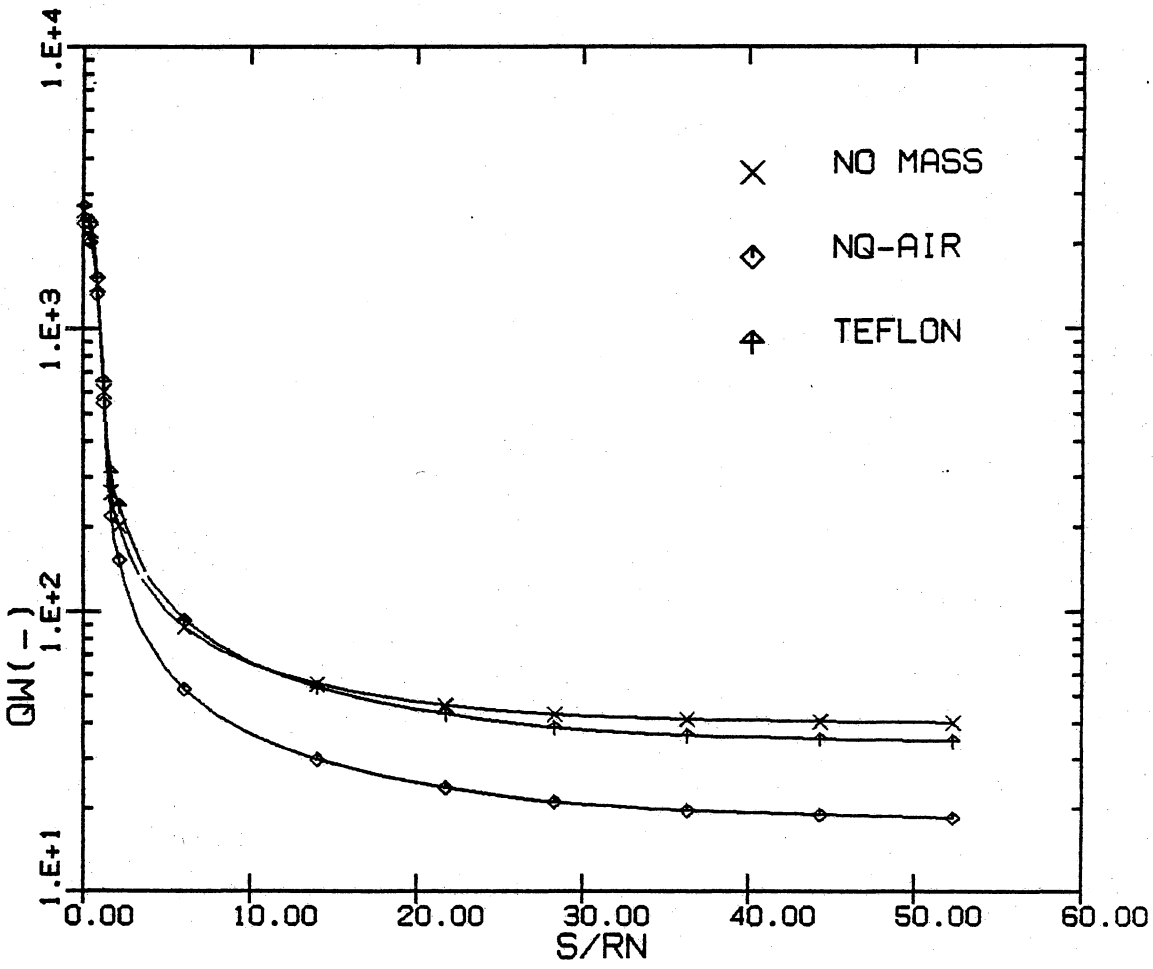

Figure 49. Heat-transfer rate distribution comparison along the body for case A.

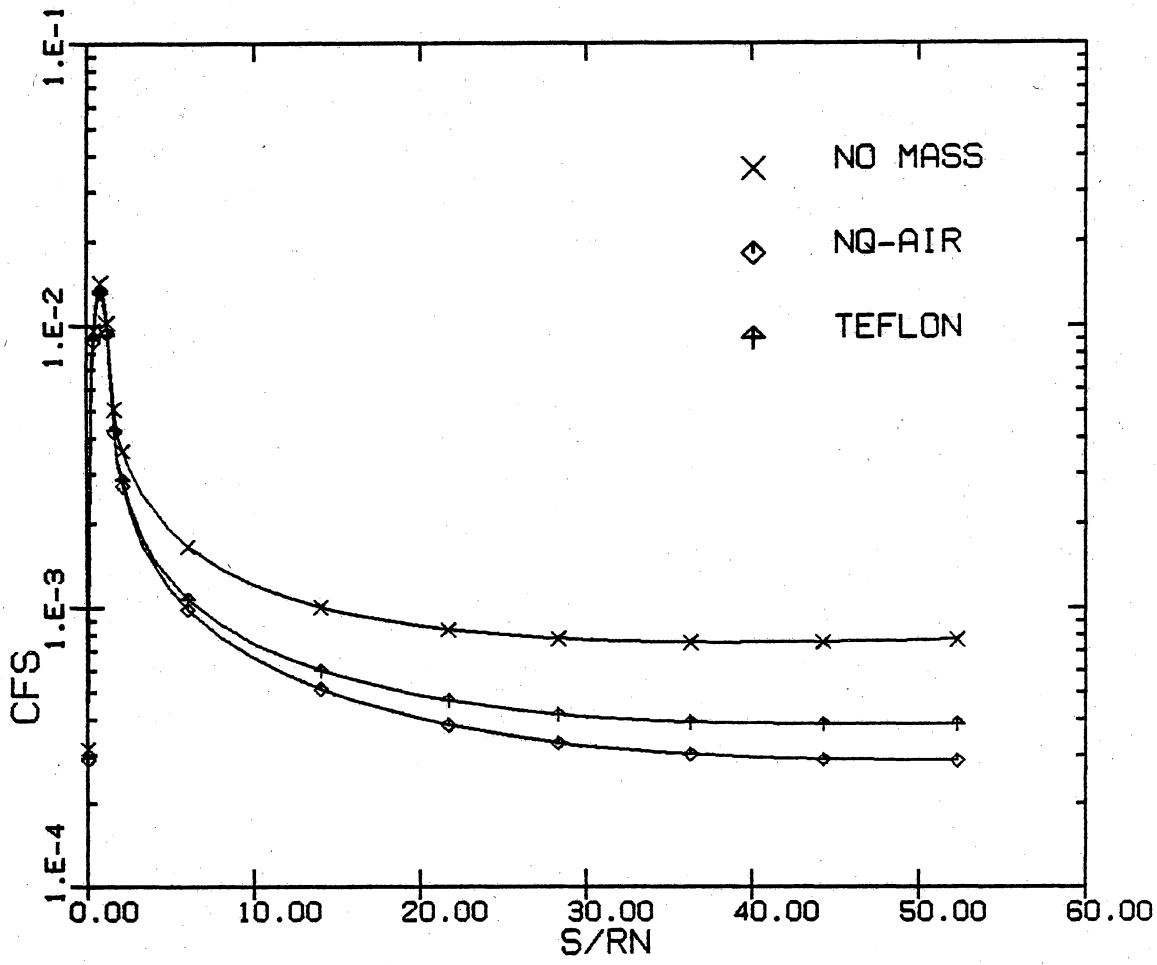

Figure 50. Skin-friction coefficient distribution compariosn along the body for case A.

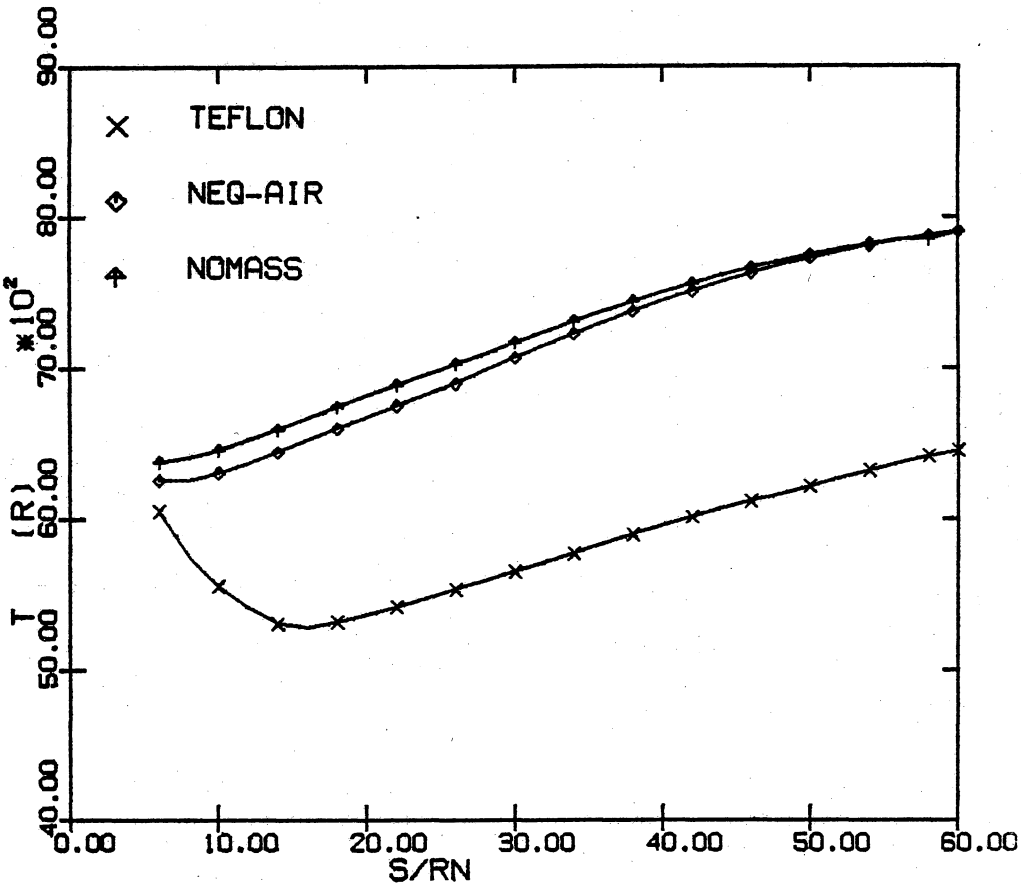

Figure 51. Shock-layer peak temperature distribution comparison along the body for case A.

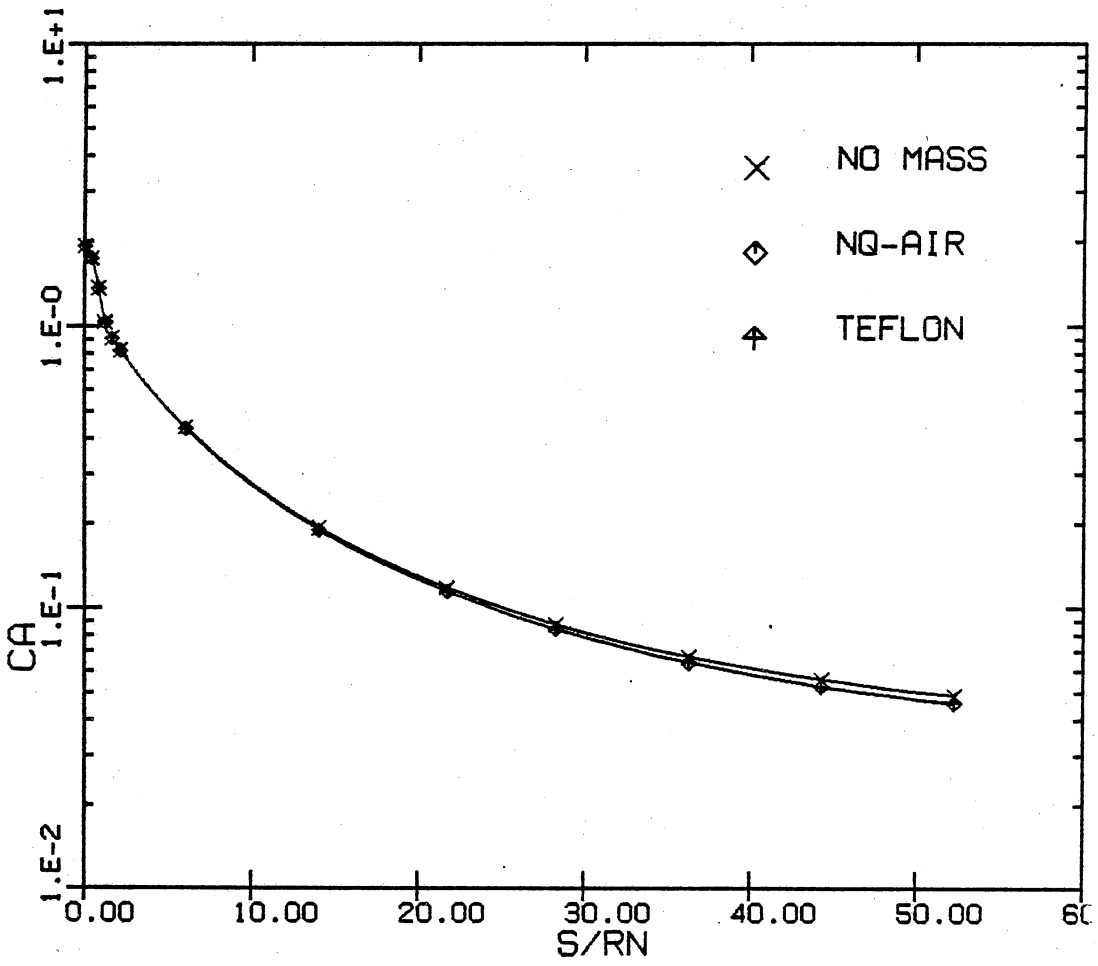

Figure 52. Axial-force coefficient distribution comparison along the body for case A.

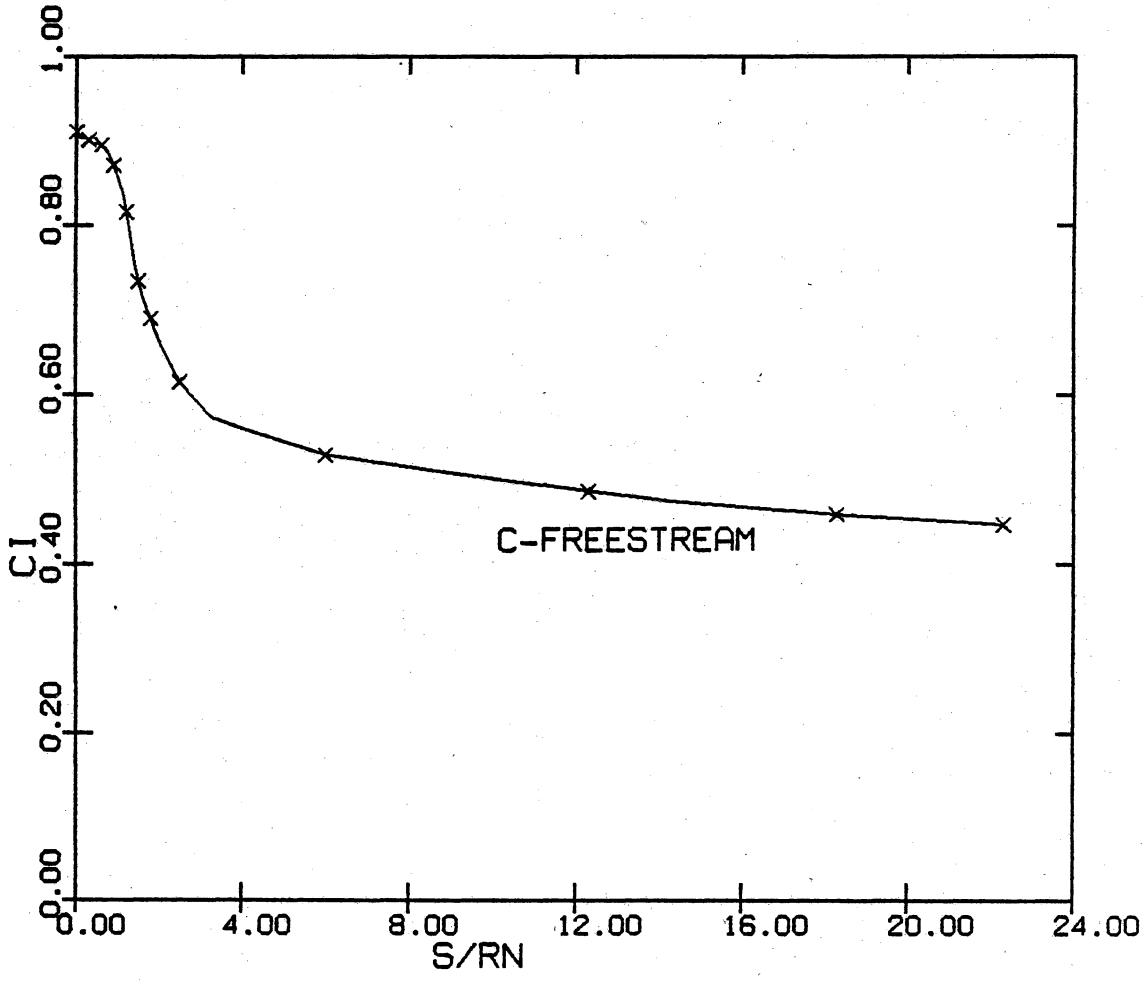

Figure 53. Freestream air distribution at the wall along the body for case B.

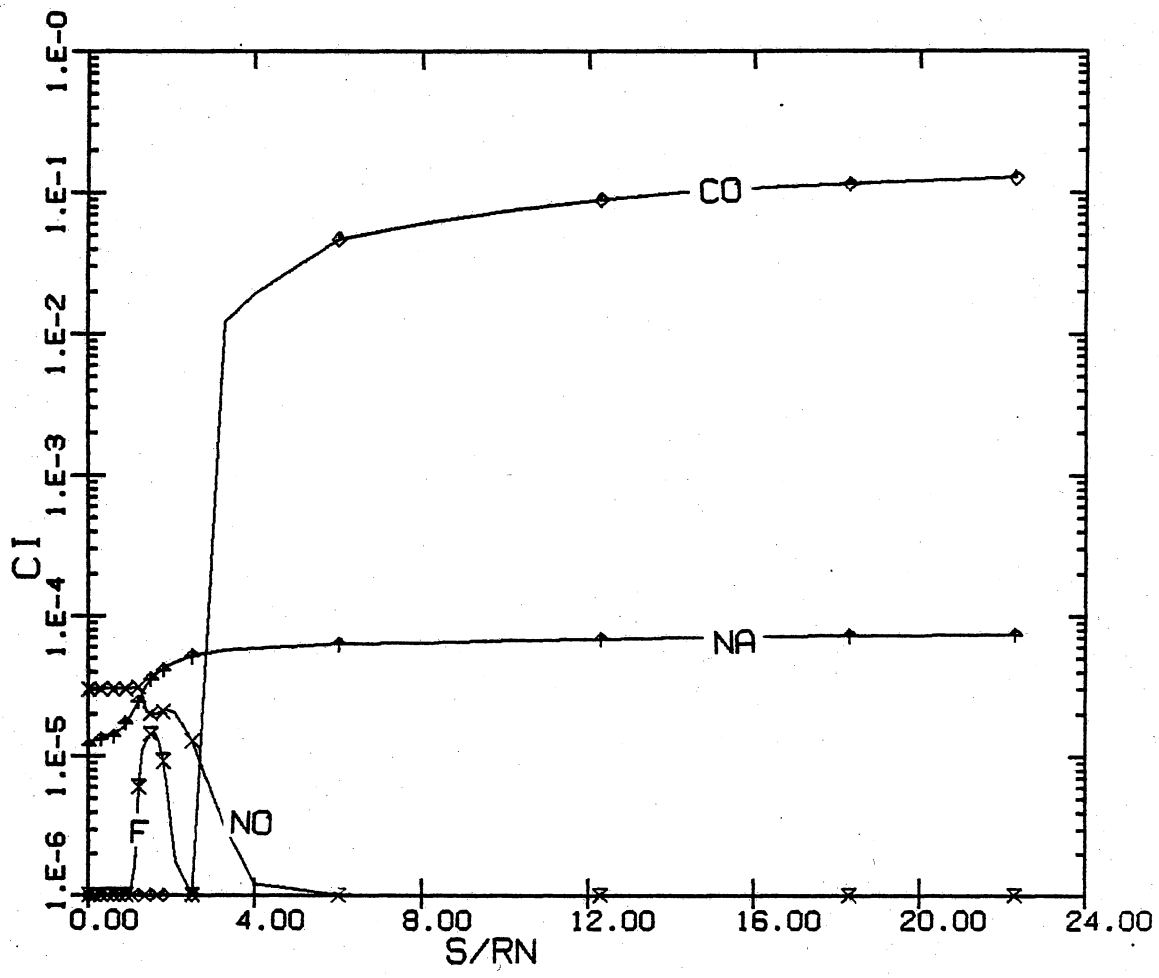

Figure 54. Equilibrium wall species concentration distribution along the body for case B.

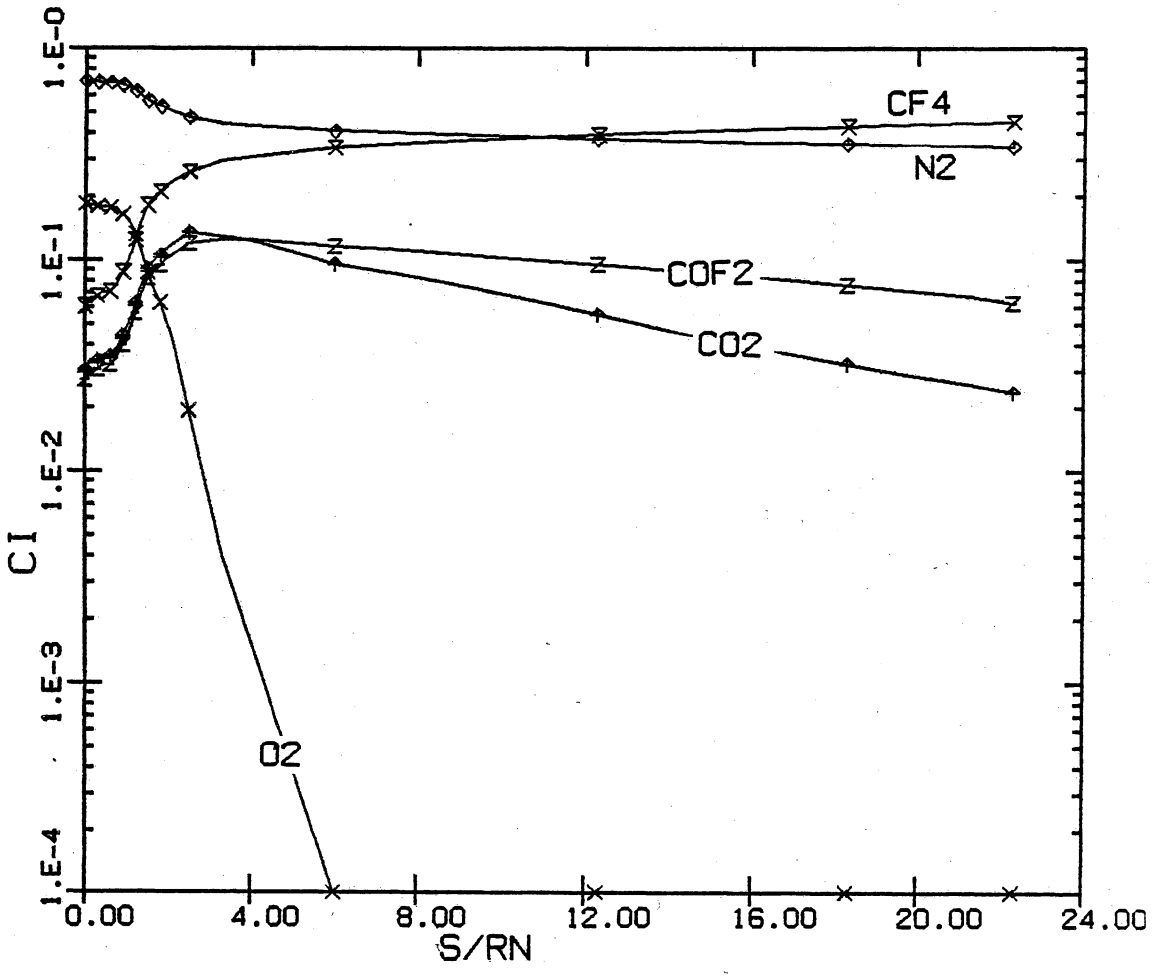

Figure 55. Equilibrium wall species concentration distribution along the body for case B.

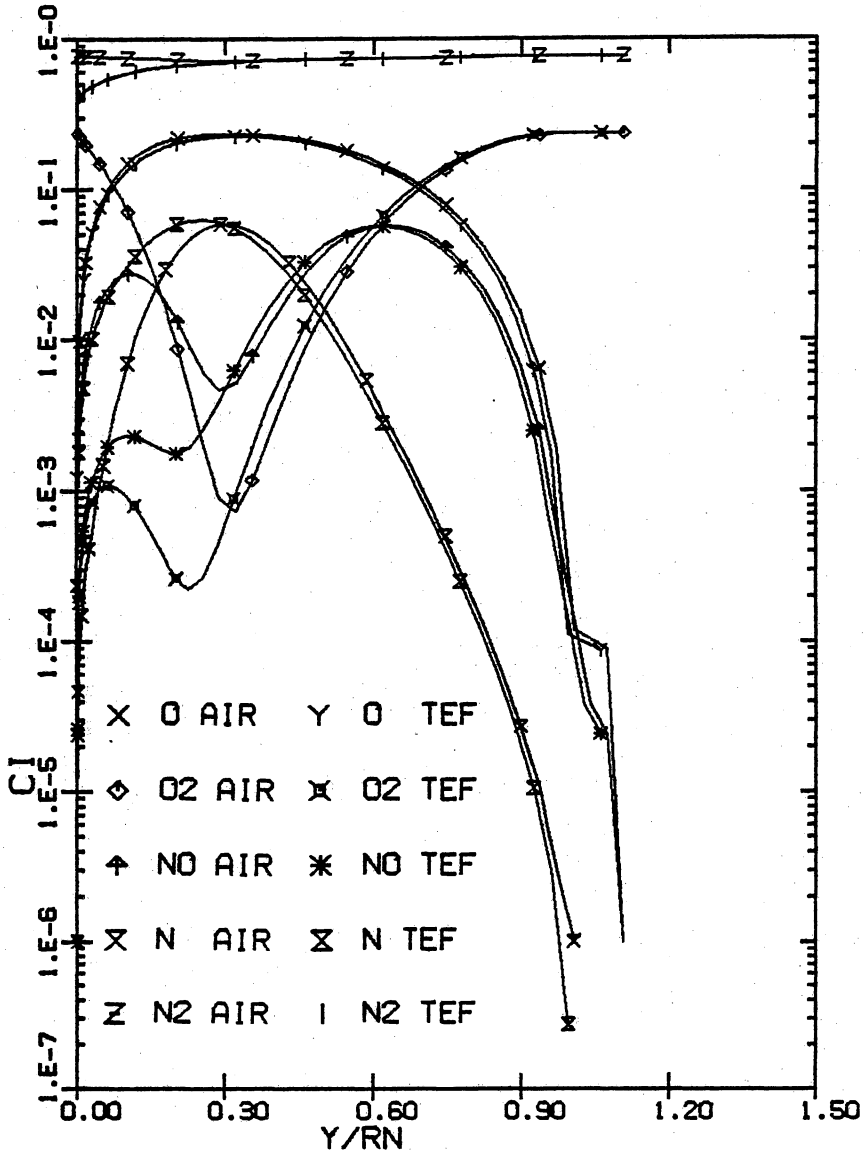

Figure 56. Nonequilibrium air species concentration comparison at s/Rn = 6.0 between the seven species code and the teflon code for case B.

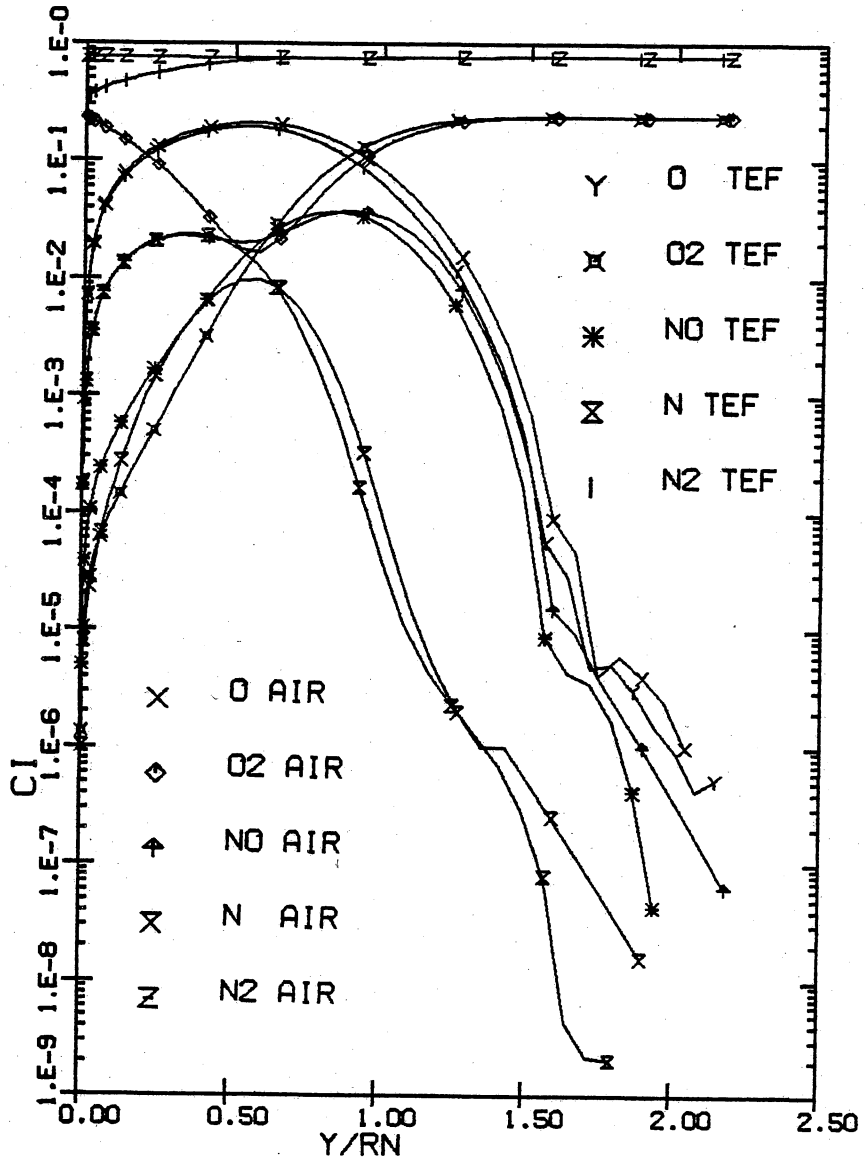

Figure 57. Nonequilibrium air species concentration comparison at s/Rn = 22.3 between the seven species code and the teflon code for case B.

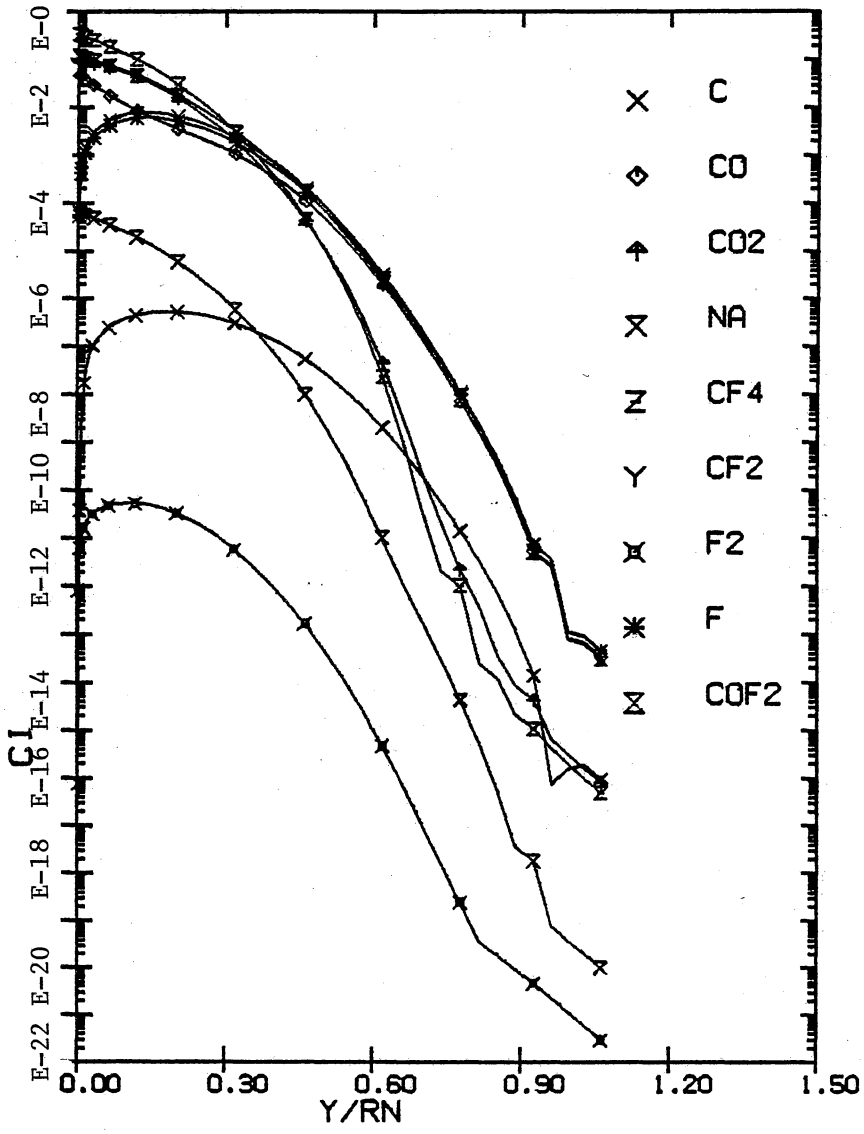

Figure 58. Teflon ablation species concentration comparison at s/Rn = 6.0 for case B.

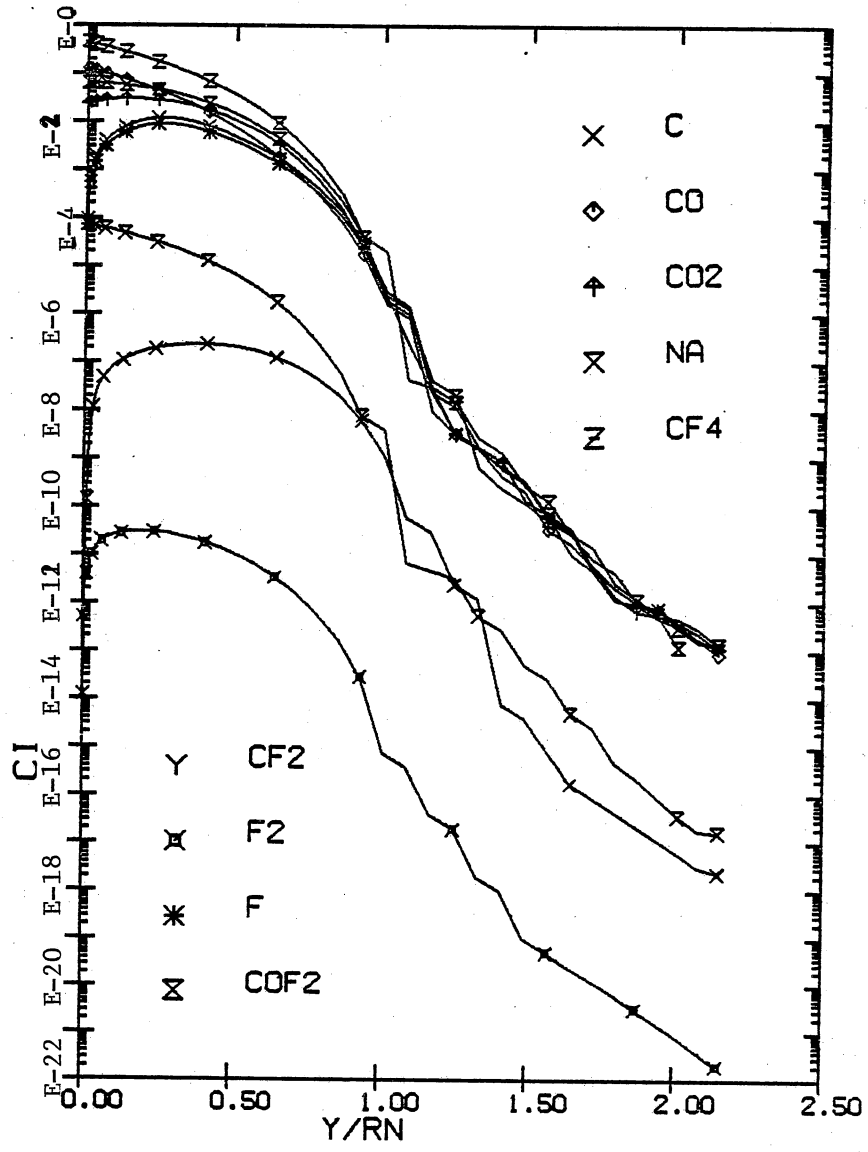

Figure 59. Teflon ablation species concentration comparison at s/Rn = 22.3 for case B.

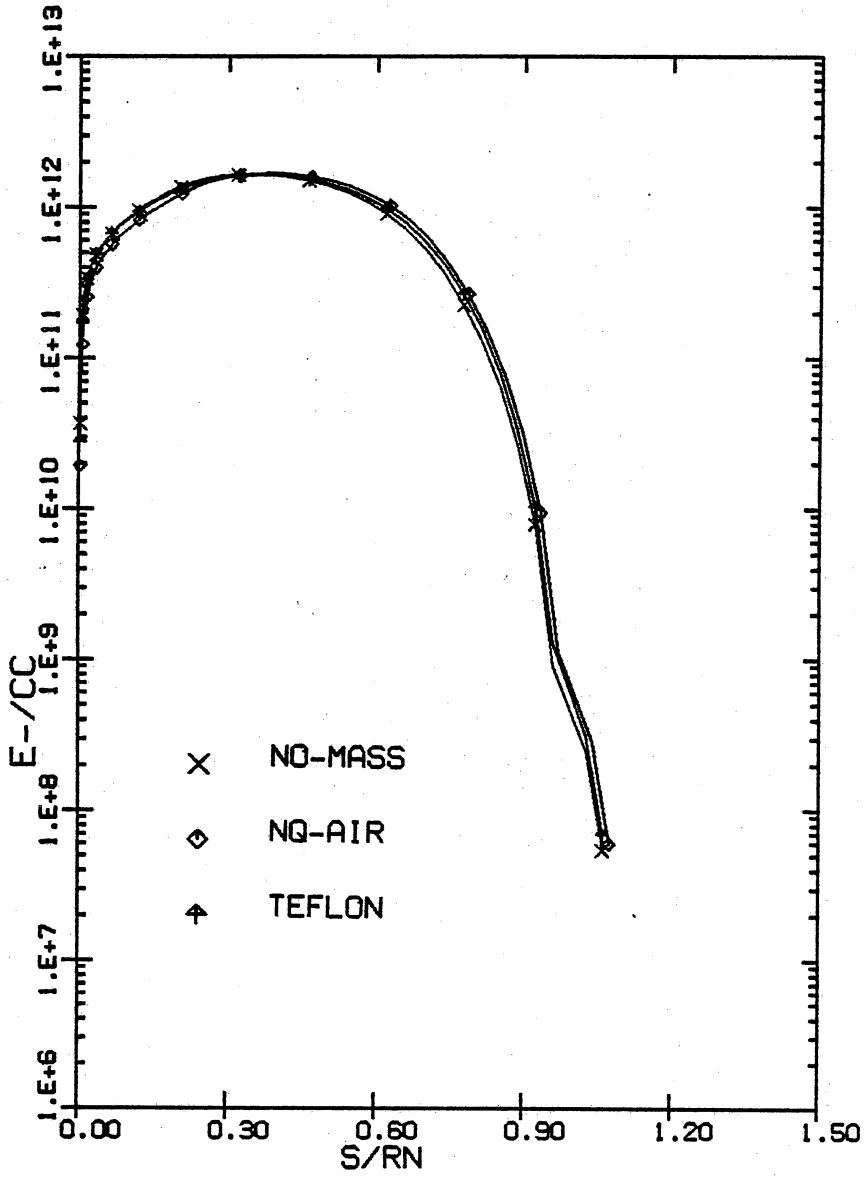

Figure 60. Electron number density comparison at s/Rn = 6.0 between the seven species code and the teflon code for case B.

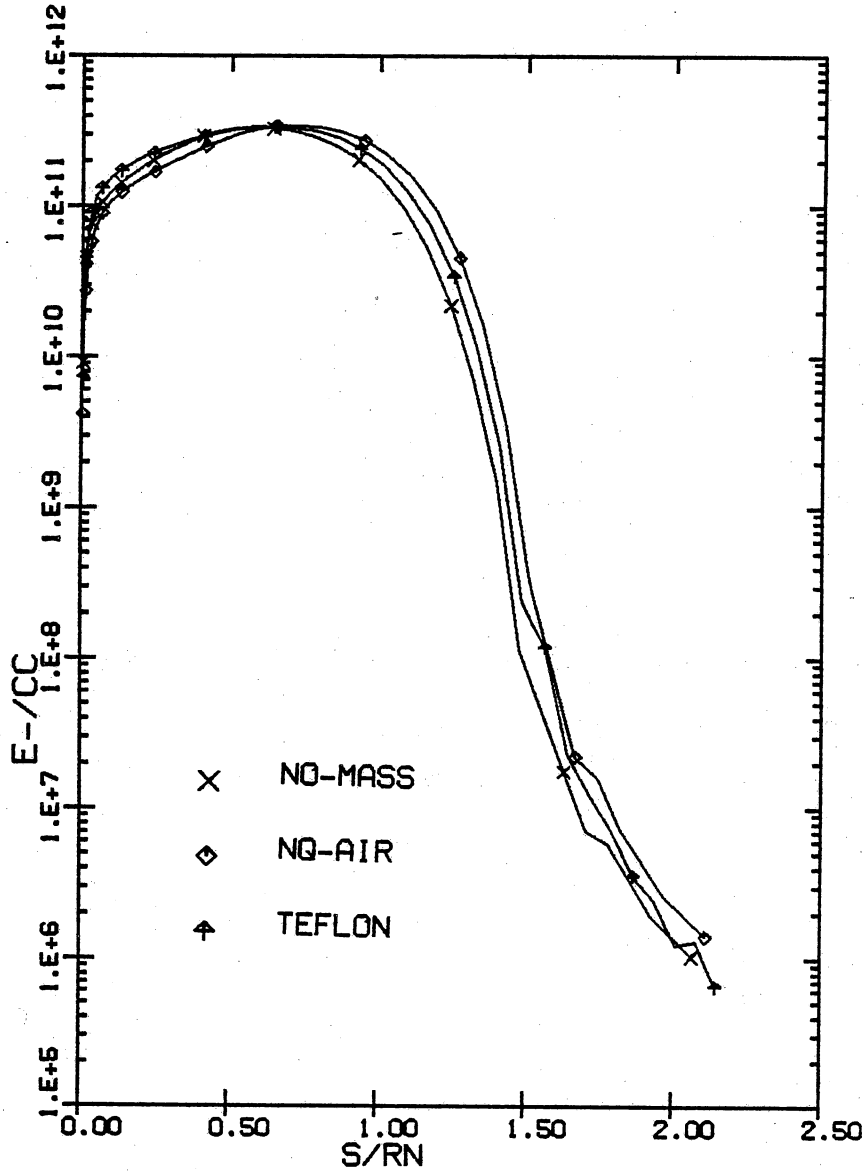

Figure 61. Electron number density comparison at s/Rn = 22.3 between the seven species code and the teflon code for case B.

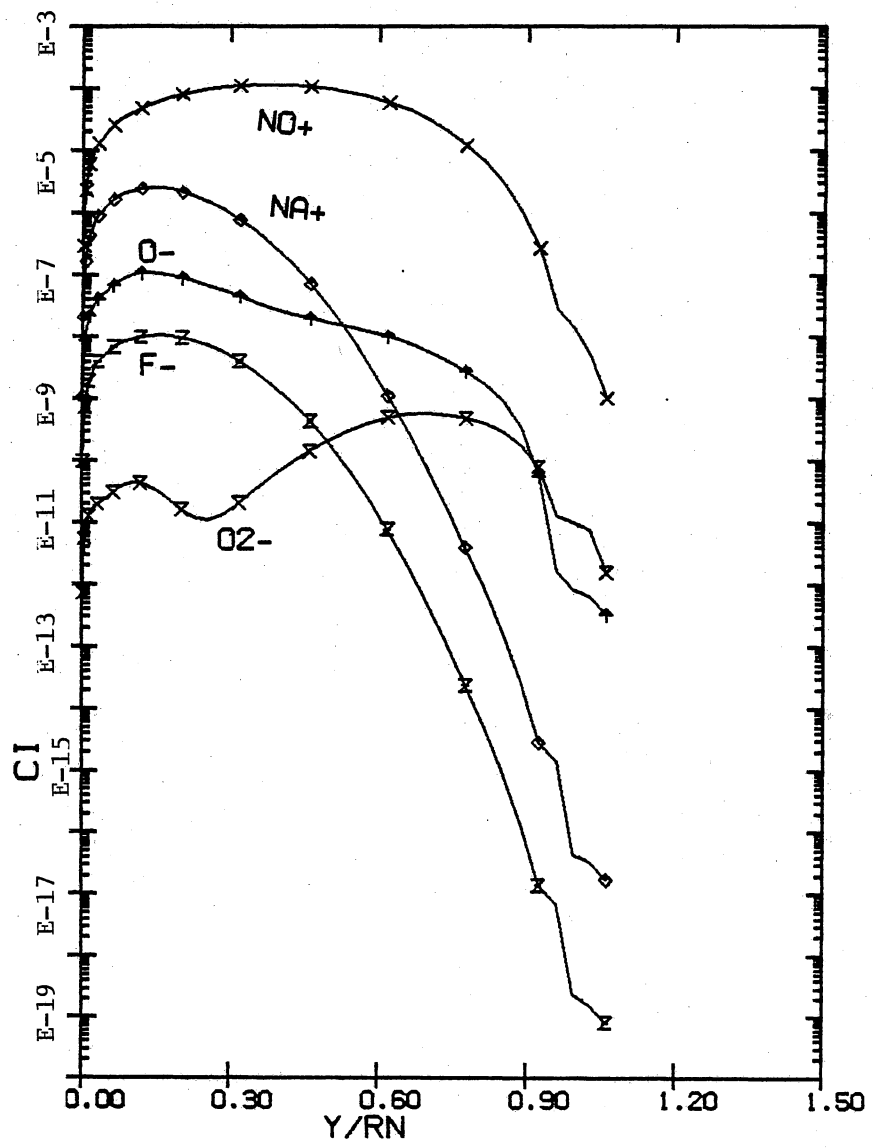

Figure 62. Ionized species concentration profile at s/Rn = 6.0 for case B.

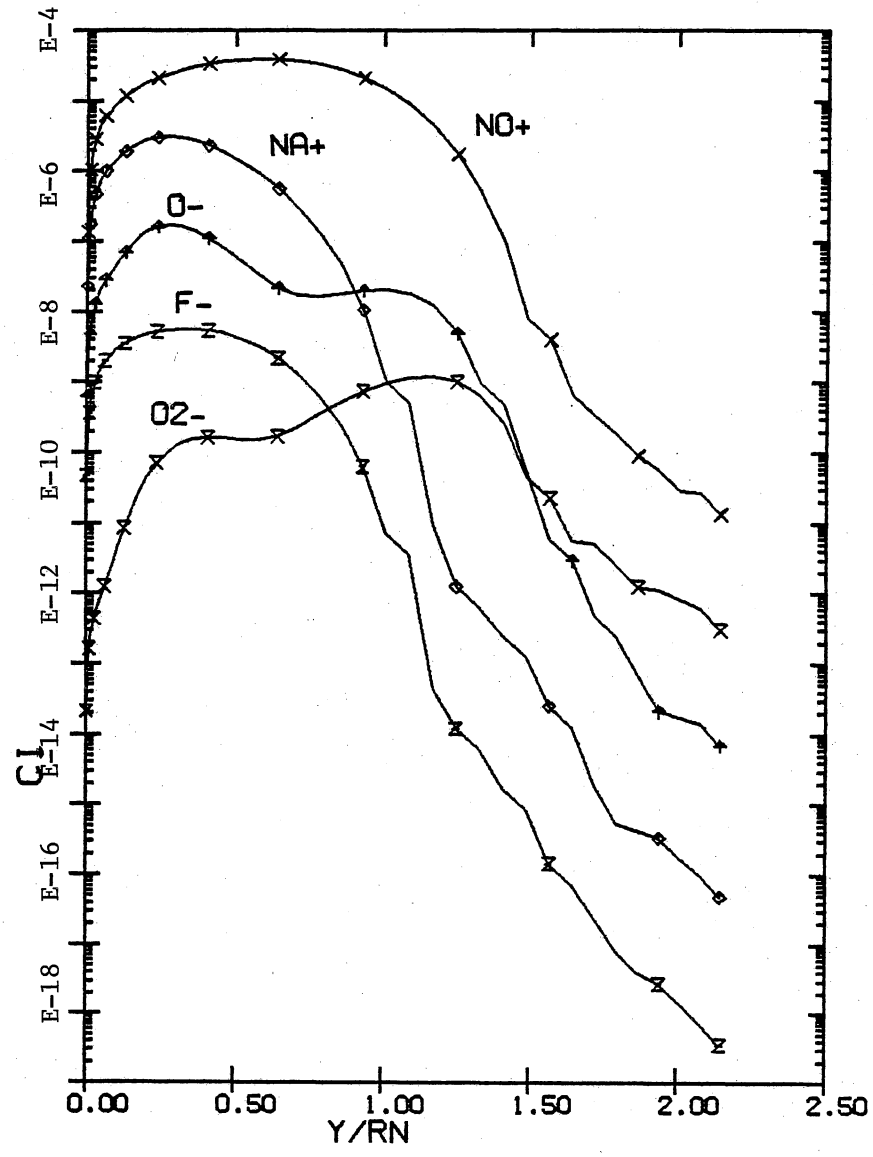

Figure 63. Ionized species concentraton profile at s/Rn = 22.3 for case B.

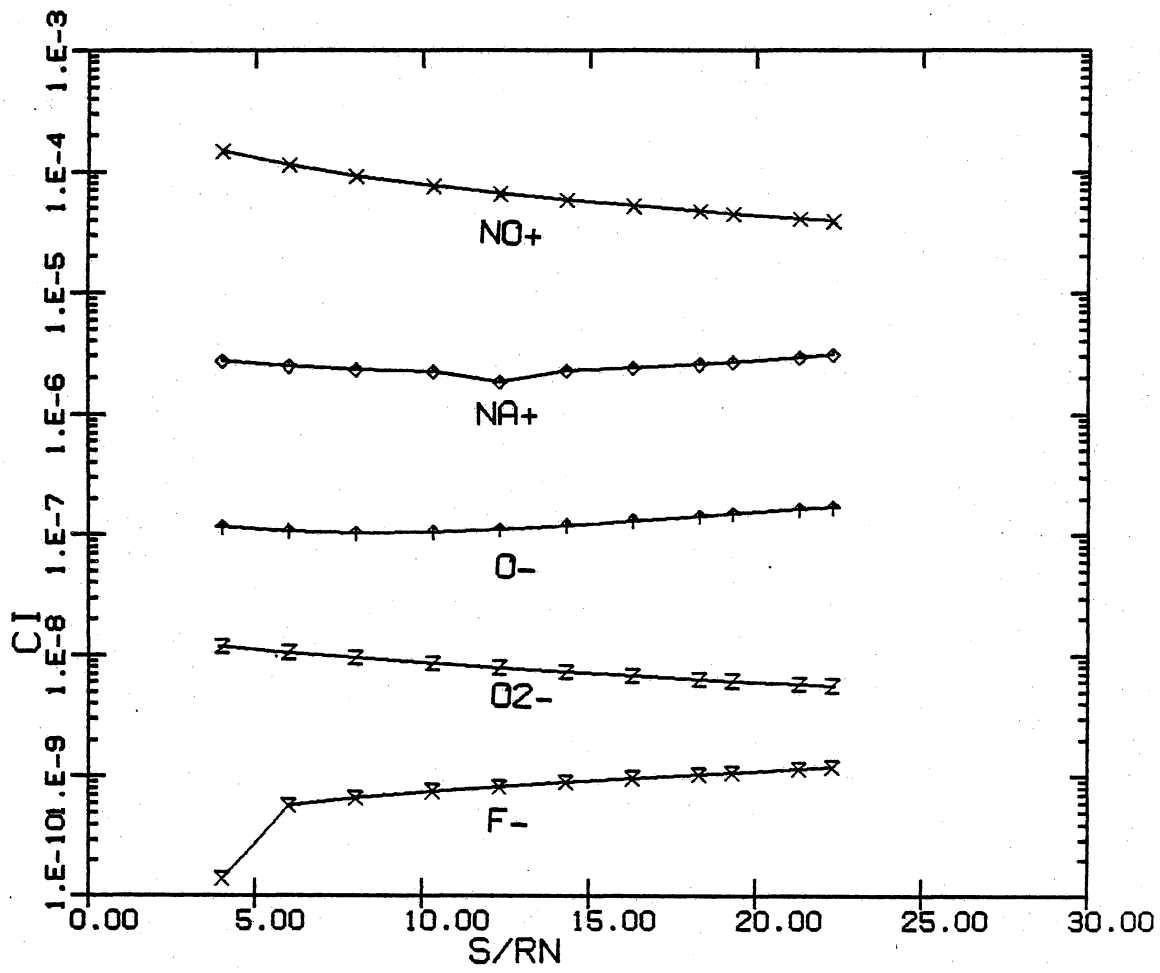

Figure 64. Peak ionized species distribution along the body for case B.

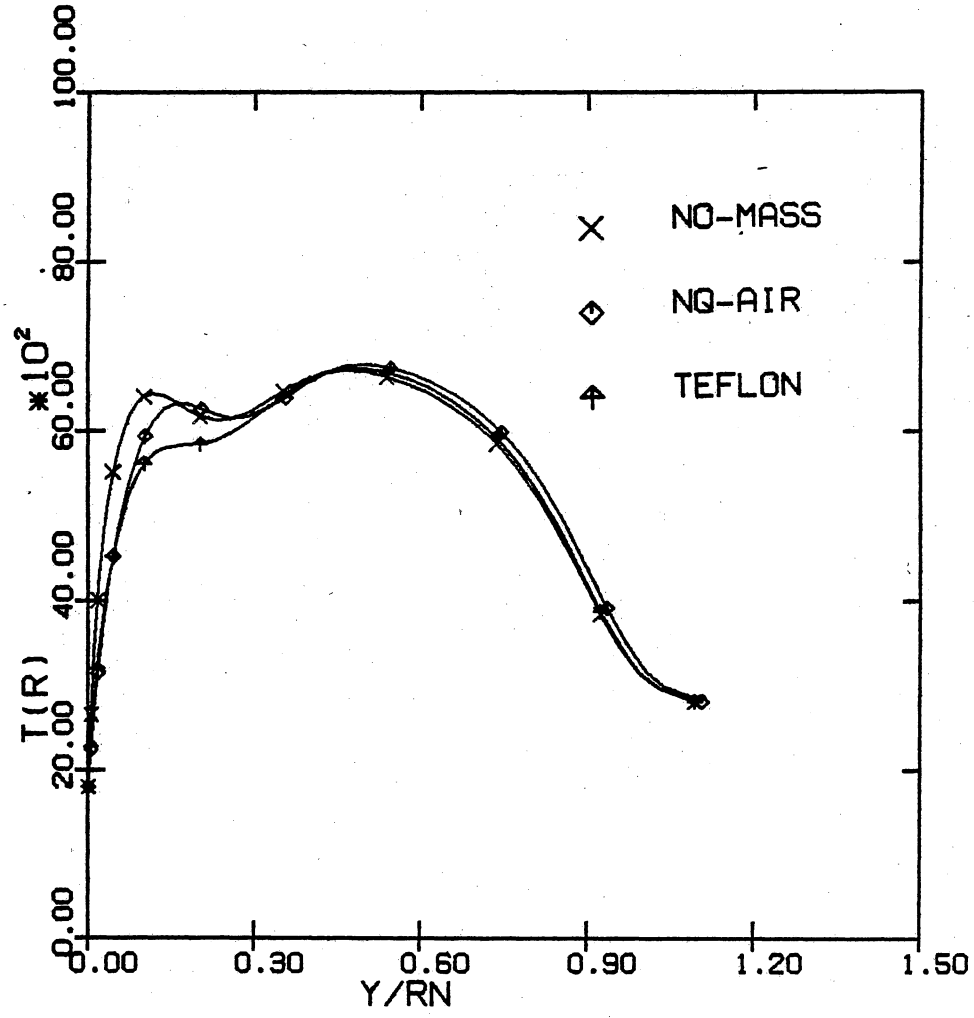

Figure 65. Temperature profile comparison at s/Rn = 6.0 between the seven species code and the teflon code for case B.

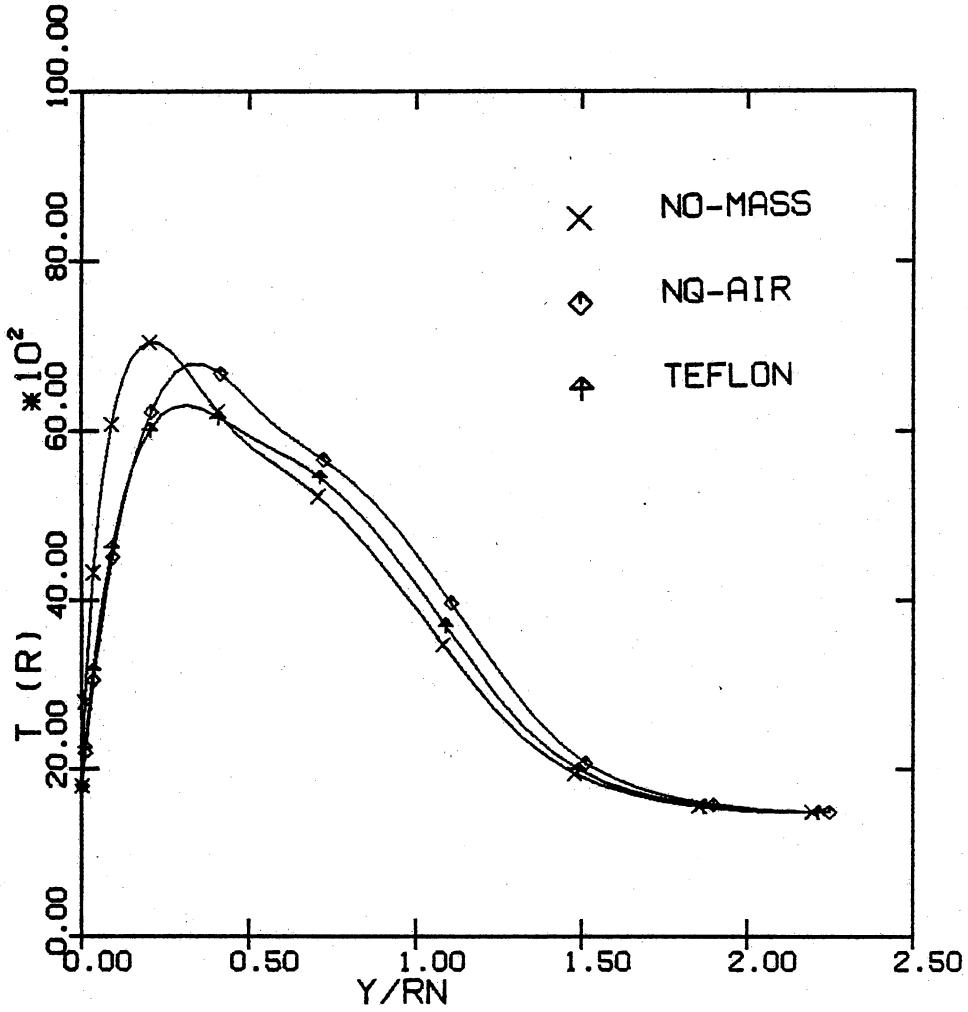

Figure 66. Temperature profile comparison at s/Rn = 22.3 between the seven species code and the teflon code for case B.

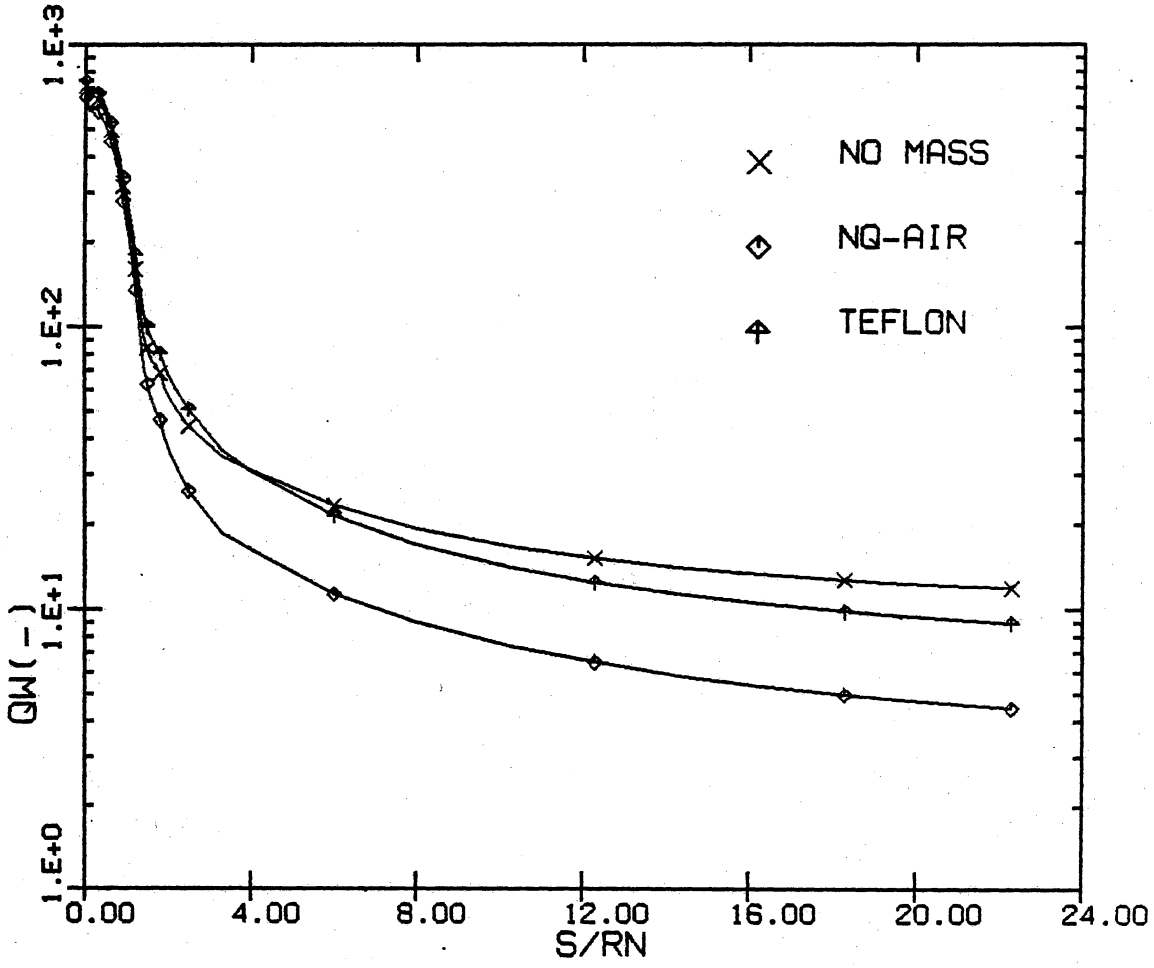

Figure 67. Wall heat-transfer rate distribution comparison between the seven species code and the teflon code for case B.

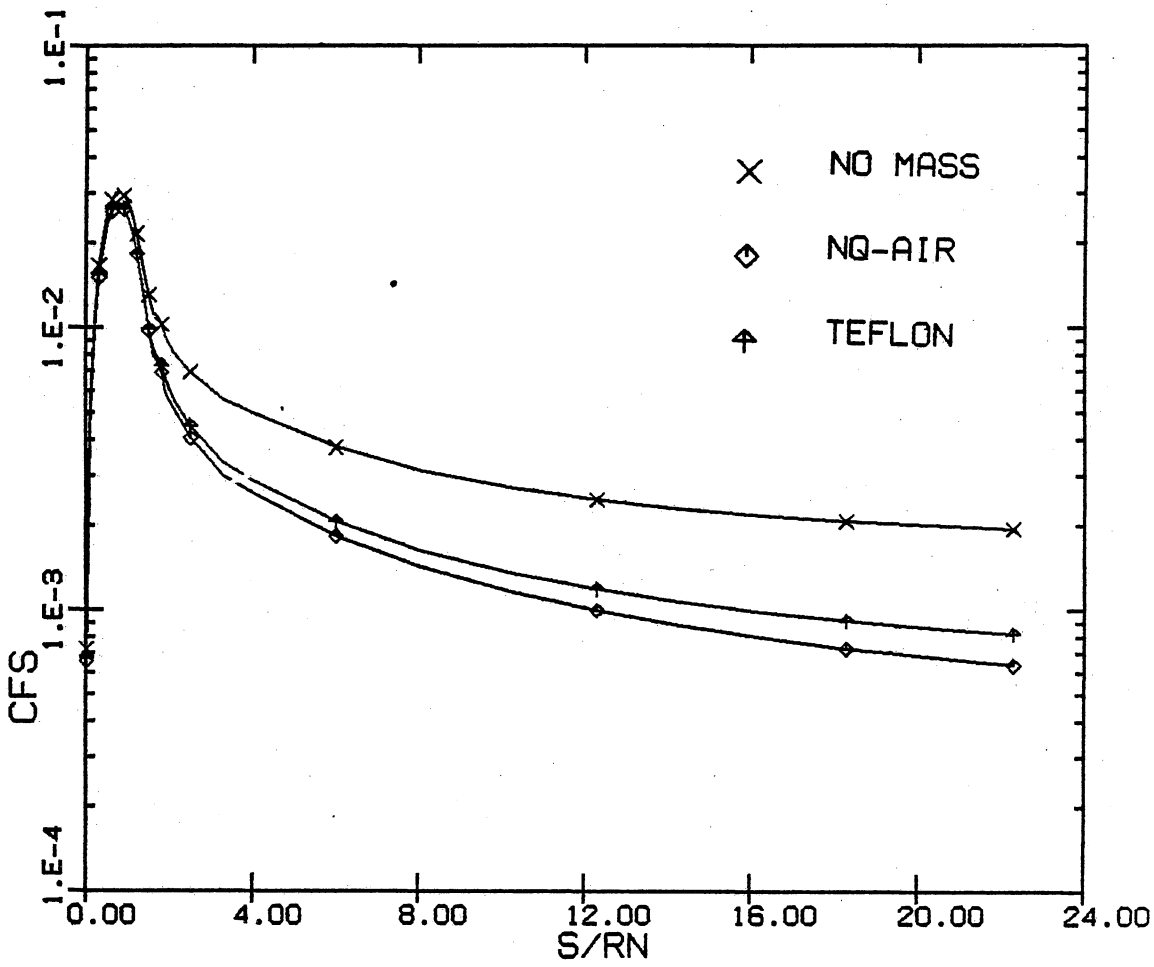

Figure 68. Skin-friction coefficient distribution comparison along the body for case B.

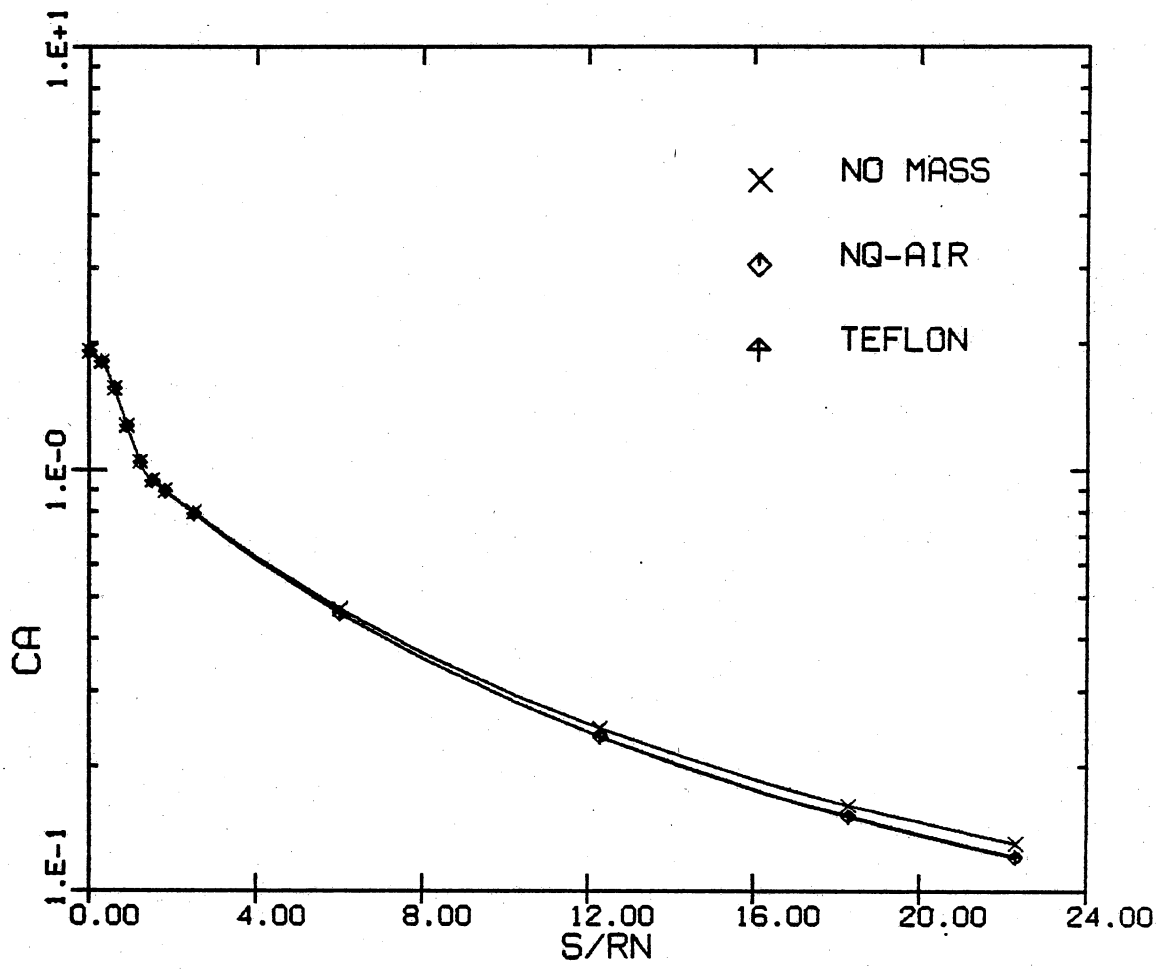

Figure 69. Axial-force coefficient distribution comparison along the body for case B.

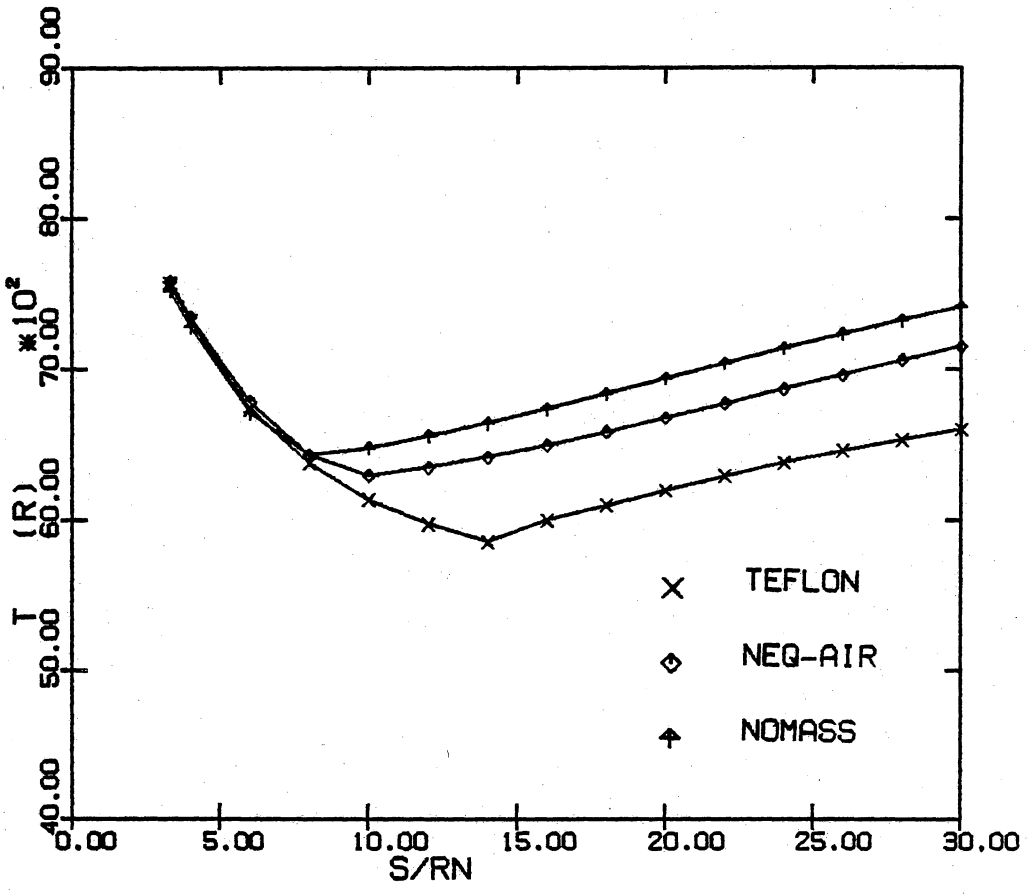

Figure 70. Shock-layer peak temperature distribution comparison along the body for case B.

Tables

Table 1. Freestream conditions of test cases

Freestream conditions:

	CASE A	CASE B	
Gamma	0.1400000D+01	0.1400000D+01	
Pressure	0.5402824D-01	0.7673787D-02	lbf/in^2
Pr. No.	0.7000000D+00	0.7000000D+00	
RGAS	0.1716000D+04	0.1716000D+04	$ft^2/sec^2/R$
Reynolds No./ft	0.5779549D+06	0.7156659D+05	ft^{-1}
Density	0.1021374D-04	0.1323831D-05	$slugs/ft^3$
Temp.	0.4427263D+03	0.4851506D+03	deg. R
Velocity	0.2240000D+05	0.2240000D+05	ft/sec
Mach No.	0.2171990D+02	0.2074852D+02	

DIMENSIONAL REFERENCE CONDITIONS ;

μ_{ref}	0.1864270D-04	0.6545608D-05	(lb-sec)/ft^2
P_{ref}	0.3558920D+02	0.4612814D+01	lbf/ft^2
ρ_{ref}	0.1021374D-04	0.1323831D-05	$slugs/ft^3$
T_{ref}	0.8313219D+05	0.8354307D+05	deg.R
H_{ref}	0.5017600D+09	0.5017600D+09	ft^2/sec^2
U_{ref}	0.2240000D+05	0.2240000D+05	ft/sec
k_{ref}	0.1125216D+00	0.3931295D-01	Btu/R-ft-sec
Cp_{ref}	0.6035689D+04	0.6006004D+04	$ft^2/sec^2/R$
W_{ref}	0.2688000D+06	0.1343997D+06	sec^{-1}

Table 2. Curve-fit coefficients of carbon and carbon dioxide

Curve-fit relations for enthalpy and specific heat

$$\frac{H}{RT} = A_1 + \frac{A_2}{2}T + \frac{A_3}{3}T^2 + \frac{A_4}{4}T^3 + \frac{A_5}{5}T^4 + \frac{A_6}{T}$$

$$\frac{Cp}{RT} = A_1 + A_2T + A_3T^2 + A_4T^3 + A_5T^4$$

Carbon

Temperature 300-1000 K from Gordon and Mcbride (1976)

0.253287E+01 -0.158876E-03 0.306821E-06
-0.267701E-09 0.874888E-13 0.852404E+05

Temperature 1000-6000 K from Gordon and Mcbride (1976)
0.258107E+01 -0.146962E-03 0.743881E-07
-0.794811E-11 0.589010E-16 0.852163E+05

Temperature 6000 K - from Esch et al.(1970)
0.2141E+01 0.3219E-03 -0.5498E-07
0.3604E-11 -0.5564E-06 0.8542E+05

Carbon dioxide

Temperature 300-1000 K from Gordon and Mcbride (1976)

0.446080E+01 0.309817E-02 -0.123926E-05
0.227413E-09 -0.155260E-13 -0.489614E+05

Temperature 1000-6000 K from Gordon and Mcbride (1976)
0.240078E+01 0.873510E-02 -0.660709E-05
0.200219E-08 0.632740E-15 -0.483775E+05

Table 3. Table of heat of formations and molecular weights of species i

Species	Heat of Formation	Molecular Weight
O	0.1661E + 09	16.0
O_2	0.0	32.0
NO	0.3225E + 08	30.008
N	0.3619E + 09	14.008
NO^+	0.35403E + 09	30.008
C	0.6378E + 09	12.011
CO	-0.4376E + 08	28.011
CO_2	-0.96214E + 08	44.011
Na	0.50600E + 08	22.991
Na^+	0.28291E + 09	22.991
O^-	0.70978E + 08	15.99995
O_2^-	-0.32391E + 08	32.0
CF_4	-0.11217E + 09	88.011
CF_2	-0.35864E + 08	50.011
F_2	0.0	38.00
F	0.43540E + 08	19.00
F^-	-0.14507E + 09	19.00
COF_2	-0.10306E + 09	66.011
C_2F_4	-0.69466E + 08	100.022
N_2	0.0	28.04

Table 4. Viscosity curve-fit coefficients for species i

NS	A_i	B_i	C_i
1	0.2002200D-01	0.4309400D+00	-0.1124600D+02
2	0.3827100D-01	0.2107600D-01	-0.9598600D+01
3	0.4250100D-01	-0.1887400D-01	-0.9619700D+01
4	0.8586300D-02	0.6463000D+00	-0.1258100D+02
5	0.4250100D-01	-0.1887400D-01	-0.9619700D+01
6	0.9251900D-01	-0.9085950D+00	-0.5627831D+01
7	0.1198880D+00	-0.1153705D+01	-0.5226518D+01
8	-0.1160800D-01	0.8719430D+00	-0.1337832D+02
9	-0.3734700D-01	0.1399119D+01	-0.1648567D+02
10	0.1454700D-01	0.2795462D+01	-0.3751667D+02
11	-0.1480900D-01	0.3304603D+01	-0.3990132D+02
12	0.4187900D-01	0.2335612D+01	-0.3542736D+02
13	-0.7675000D-02	0.7958750D+00	-0.1294743D+02
14	-0.5810000D-02	0.7599890D+00	-0.1270910D+02
15	-0.6147000D-02	0.7664700D+00	-0.1254452D+02
16	-0.6147000D-02	0.7664700D+00	-0.1264478D+02
17	0.6806600D-01	0.1848825D+01	-0.3343001D+02
18	0.5780000D-02	0.4740460D+00	-0.1124661D+02
19	-0.1483600D-01	0.9347720D+00	-0.1363985D+02
20	0.4834900D-01	-0.2248500D-01	-0.9982700D+01

where

$$\mu_i = e^{C_i T_k^{A_i} \ln T_k + B_i} \quad \left(\frac{gm}{cm - \sec}\right)$$

Table 5. Viscosity curve-fit coefficients for carbon and carbon monoxide

Viscosity Curve-fit coefficients for C, and CO were obtained from Moss (1984) in the following form:

$$\mu = a_i + b_i T_k + c_i T_k^2 \quad (lbm/ft/\text{ sec})$$

	a_i	b_i	c_i
C	0.2000E-04	0.1772E-07	0.3378E-12
CO	0.2404E-04	0.1363E-07	-0.2184E-12

Table 6. Reaction rate data for 28 chemical reactions

From Blottner, Langen, Appleton, Cresswell et al.
Reaction Rate Constant

$$K_{fr} = T_k^{C_{2r}} e^{(C_{0r} - \frac{C_{1r}}{T_k})}$$

$$K_{br} = T_k^{D_{2r}} e^{(D_{0r} - \frac{D_{1r}}{T_k})}$$

NR	EXP(C0r)	C1r	C2r	EXP(D0r)	D1r	D2r
1	0.3610D+19	59400.0	-1.000	0.3010D+16	0.0	-0.500
2	0.1920D+18	113100.0	-0.500	0.1090D+17	0.0	-0.500
3	0.4150D+23	113100.0	-1.500	0.2320D+22	0.0	-1.500
4	0.3970D+21	75600.0	-1.500	0.1010D+21	0.0	-1.500
5	0.3180D+10	19700.0	1.000	0.9630D+12	3600.0	0.500
6	0.6750D+14	37500.0	0.000	0.1500D+14	0.0	0.000
7	0.9030D+10	32400.0	0.500	0.1800D+20	0.0	-1.000
8	0.6690D+10	64638.7	-2.540	0.2400D+24	43024.0	-2.500
9	0.1000D+17	1761.2	0.000	0.1090D+21	65032.0	-0.580
10	0.1690D+28	129000.0	-2.860	0.6340D+24	-2116.0	-2.420
11	0.4130D+16	98025.0	0.000	0.1550D+13	-33091.0	0.440
12	0.2000D+07	1610.3	0.000	0.0000D+00	0.0	0.000
13	0.1070D+18	54105.1	0.070	0.2000D+18	0.0	0.000
14	0.1460D+20	42189.7	-0.700	0.2000D+20	0.0	-0.600
15	0.1620D+13	59187.5	1.460	0.3000D+21	0.0	0.000
16	0.2160D+32	59187.5	-3.040	0.4000D+40	0.0	-4.500
17	0.1200D+15	0.0	-0.750	0.0000D+00	0.0	0.000
18	0.2000D+20	0.0	-0.500	0.1480D+12	16997.8	1.050
19	0.2000D+19	0.0	-0.500	0.1870D+11	5082.4	0.900
20	0.7820D+16	28023.5	0.500	0.0000D+00	0.0	0.000
21	0.6000D+12	0.0	0.000	0.0000D+00	0.0	0.000
22	0.2920D+11	6682.6	0.500	0.0000D+00	0.0	0.000
23	0.9240D+15	48130.6	0.500	0.0000D+00	0.0	0.000
24	0.4290D+12	48130.6	0.500	0.0000D+00	0.0	0.000
25	0.7900D+13	18474.7	0.200	0.3290D+13	0.0	0.000
26	0.3300D+16	0.0	0.000	0.3000D+08	21540.7	1.400
27	0.3000D+12	40015.4	0.700	0.1360D+20	0.0	-0.900
28	0.2000D+10	0.0	0.000	0.0000D+00	0.0	0.000

Table 7. Viscosity data for some species

σ and $\frac{\varepsilon}{k}$ of some speccis

Species	σ	Method for σ	$\frac{\varepsilon}{k}$	Method for $\frac{\varepsilon}{k}$	
CF_2	3.977	1	108.0	1	
CF_4	4.662	2	134.0	2	McCoubrey(1957)
CO_2	3.941	2	195.2	2	Kiyama (1952)
F	2.968	3	112.6	4	
F_2	3.357	2	112.6	2	
Na	3.567	5	1375.0	6	

1. Linear relations used between diatomic and highest polyatomic in the series
2. Least-square fit of experimental viscosity data
3. $\sigma_{monatomic} = \frac{3}{4}\sigma_{diatomic} + 0.45$
4. Molar volume at the melting point, $b_0 = \frac{2}{3}\pi N\sigma^3 = 2.3V_m$
5. Boiling point temperature, $\frac{\varepsilon}{k} = 1.18T_b$ (or $1.18T_{sub}$ if T_b is not available)

ALPHSB(28,28)

NR	ALSUB	NR	O	O2	NO	N	NOP	C	CO	CO2	NA	NAP	OM	O2M	CF4	CF2	F2	F	FM	COF2	C2F4	N2	M1	M2	M3	M4	M5	M6	M7	EL
1	1.0	1	0.	1.	0.	0.	0.	0.	0.	0.	0.	0.	0.	0.	0.	0.	0.	0.	0.	0.	0.	0.	1.	0.	0.	0.	0.	0.	0.	0.
2	1.0	2	0.	0.	0.	0.	0.	0.	0.	0.	0.	0.	0.	0.	0.	0.	0.	0.	0.	0.	0.	1.	0.	1.	0.	0.	0.	0.	0.	0.
3	1.0	3	0.	0.	0.	1.	0.	0.	0.	0.	0.	0.	0.	0.	0.	0.	0.	0.	0.	0.	0.	1.	0.	0.	0.	0.	0.	0.	0.	0.
4	1.0	4	0.	0.	1.	0.	0.	0.	0.	0.	0.	0.	0.	0.	0.	0.	0.	0.	0.	0.	0.	0.	0.	1.	0.	0.	0.	0.	0.	0.
5	1.0	5	1.	0.	1.	0.	0.	0.	0.	0.	0.	0.	0.	0.	0.	0.	0.	0.	0.	0.	0.	0.	0.	0.	0.	0.	0.	0.	0.	0.
6	1.0	6	1.	0.	0.	0.	0.	0.	0.	0.	0.	0.	0.	0.	0.	0.	0.	0.	0.	0.	0.	1.	0.	0.	0.	0.	0.	0.	0.	0.
7	1.0	7	1.	0.	0.	1.	0.	0.	0.	0.	0.	0.	0.	0.	0.	0.	0.	0.	0.	0.	0.	0.	0.	0.	0.	0.	0.	0.	0.	0.
8	1.0	8	0.	1.	0.	0.	0.	0.	0.	0.	0.	0.	0.	0.	0.	0.	0.	0.	0.	0.	0.	1.	0.	0.	0.	0.	0.	0.	0.	0.
9	2.0	9	1.	0.	0.	0.	0.	1.	0.	0.	0.	0.	0.	0.	0.	0.	0.	0.	0.	0.	0.	0.	0.	0.	0.	1.	0.	0.	0.	0.
10	1.0	10	0.	0.	0.	0.	0.	0.	1.	0.	0.	0.	0.	0.	0.	0.	0.	0.	0.	0.	0.	0.	0.	0.	0.	0.	1.	0.	0.	0.
11	1.0	11	1.	0.	0.	0.	0.	0.	1.	0.	0.	0.	0.	0.	0.	0.	0.	0.	0.	0.	0.	0.	0.	0.	0.	0.	0.	0.	0.	0.
12	1.0	12	1.	0.	0.	0.	0.	0.	1.	0.	0.	0.	0.	0.	0.	0.	0.	0.	0.	0.	0.	0.	0.	0.	0.	0.	0.	0.	0.	0.
13	1.0	13	0.	1.	0.	0.	0.	0.	0.	1.	0.	0.	0.	0.	0.	0.	0.	0.	0.	0.	0.	0.	0.	0.	0.	0.	0.	0.	0.	0.
14	1.0	14	1.	0.	0.	0.	0.	0.	0.	0.	1.	0.	0.	0.	0.	0.	0.	0.	0.	0.	0.	0.	0.	0.	0.	0.	0.	0.	0.	0.
15	1.0	15	0.	0.	0.	0.	0.	0.	0.	0.	1.	0.	0.	0.	0.	0.	0.	0.	0.	0.	0.	0.	0.	0.	0.	0.	0.	1.	0.	0.
16	1.0	16	0.	0.	0.	0.	0.	0.	0.	0.	1.	0.	0.	0.	0.	0.	0.	0.	0.	0.	0.	0.	0.	0.	0.	0.	0.	0.	0.	1.
17	1.0	17	0.	0.	0.	0.	0.	0.	0.	0.	0.	1.	0.	0.	0.	0.	0.	0.	0.	0.	0.	0.	0.	0.	0.	0.	0.	0.	0.	1.
18	2.0	18	1.	0.	0.	0.	0.	0.	0.	0.	0.	0.	0.	0.	0.	0.	0.	0.	0.	0.	0.	0.	0.	0.	0.	0.	0.	0.	1.	1.
19	2.0	19	0.	1.	0.	0.	0.	0.	0.	0.	0.	0.	0.	0.	0.	0.	0.	0.	0.	0.	0.	0.	0.	0.	0.	0.	0.	0.	1.	1.
20	1.0	20	0.	0.	0.	0.	0.	0.	0.	0.	0.	0.	0.	0.	0.	0.	0.	0.	0.	0.	1.	0.	0.	0.	0.	0.	0.	1.	0.	0.
21	1.0	21	1.	0.	0.	0.	0.	0.	0.	0.	0.	0.	0.	0.	0.	0.	0.	0.	0.	0.	1.	0.	0.	0.	0.	0.	0.	0.	0.	0.
22	1.0	22	0.	1.	0.	0.	0.	0.	0.	0.	0.	0.	0.	0.	1.	0.	0.	0.	0.	0.	0.	0.	0.	0.	0.	0.	0.	0.	0.	0.
23	1.0	23	0.	0.	0.	0.	0.	0.	0.	0.	0.	0.	0.	1.	0.	0.	0.	0.	0.	0.	0.	0.	0.	0.	0.	0.	0.	1.	0.	0.
24	1.0	24	0.	0.	0.	0.	0.	0.	0.	0.	0.	0.	0.	0.	0.	0.	0.	0.	0.	1.	0.	0.	0.	0.	0.	0.	0.	1.	0.	0.
25	1.0	25	0.	0.	0.	0.	0.	0.	0.	0.	0.	0.	0.	0.	0.	1.	0.	0.	0.	0.	0.	0.	0.	0.	0.	0.	0.	1.	0.	0.
26	1.0	26	0.	0.	0.	0.	0.	0.	0.	0.	0.	0.	0.	0.	0.	0.	1.	0.	0.	0.	0.	0.	0.	0.	0.	0.	0.	0.	0.	1.
27	1.0	27	0.	0.	0.	0.	0.	0.	0.	0.	0.	0.	0.	0.	0.	0.	0.	1.	0.	0.	0.	0.	0.	0.	0.	0.	0.	1.	0.	0.
28	1.0	28	0.	0.	0.	0.	0.	0.	0.	0.	0.	0.	0.	0.	0.	0.	0.	1.	0.	0.	0.	0.	0.	0.	0.	0.	0.	0.	0.	1.

BETASB(28,28)

NR	BETSUB	NR	O	O2	NO	N	NOP	C	CO	CO2	NA	NAP	OM	O2M	CF4	CF2	F2	F	FM	COF2	C2F4	N2	M1	M2	M3	M4	M5	M6	M7	EL
1	2.0	1	2.	0.	0.	0.	0.	0.	0.	0.	0.	0.	0.	0.	0.	0.	0.	0.	0.	0.	0.	0.	1.	0.	0.	0.	0.	0.	0.	0.
2	2.0	2	0.	0.	0.	2.	0.	0.	0.	0.	0.	0.	0.	0.	0.	0.	0.	0.	0.	0.	0.	0.	0.	1.	0.	0.	0.	0.	0.	0.
3	2.0	3	0.	0.	0.	3.	0.	0.	0.	0.	0.	0.	0.	0.	0.	0.	0.	0.	0.	0.	0.	0.	0.	0.	0.	0.	0.	0.	0.	0.
4	2.0	4	1.	0.	0.	1.	0.	0.	0.	0.	0.	0.	0.	0.	0.	0.	0.	0.	0.	0.	0.	0.	0.	1.	0.	0.	0.	0.	0.	0.
5	1.0	5	0.	1.	0.	1.	0.	0.	0.	0.	0.	0.	0.	0.	0.	0.	0.	0.	0.	0.	0.	0.	0.	0.	0.	0.	0.	0.	0.	0.
6	1.0	6	0.	0.	1.	1.	0.	0.	0.	0.	0.	0.	0.	0.	0.	0.	0.	0.	0.	0.	0.	0.	0.	0.	0.	0.	0.	0.	0.	0.
7	1.0	7	0.	0.	0.	0.	1.	0.	0.	0.	0.	0.	0.	0.	0.	0.	0.	0.	0.	0.	0.	0.	0.	0.	0.	0.	0.	0.	0.	1.
8	1.0	8	0.	0.	2.	0.	0.	0.	0.	0.	0.	0.	0.	0.	0.	0.	0.	0.	0.	0.	0.	0.	0.	0.	0.	0.	0.	0.	0.	0.
9	1.0	9	0.	0.	0.	0.	0.	0.	1.	0.	0.	0.	0.	0.	0.	0.	0.	0.	0.	0.	0.	0.	0.	0.	0.	1.	0.	0.	0.	0.
10	2.0	10	1.	0.	0.	0.	0.	1.	0.	0.	0.	0.	0.	0.	0.	0.	0.	0.	0.	0.	0.	0.	0.	0.	0.	0.	1.	0.	0.	0.
11	2.0	11	2.	0.	0.	0.	0.	1.	0.	0.	0.	0.	0.	0.	0.	0.	0.	0.	0.	0.	0.	0.	0.	0.	0.	0.	0.	1.	0.	0.
12	-0.0	12	0.	0.	0.	0.	0.	0.	0.	1.	0.	0.	0.	0.	0.	0.	0.	0.	0.	0.	0.	0.	0.	0.	0.	0.	0.	0.	0.	0.
13	1.0	13	0.	0.	0.	0.	0.	0.	0.	0.	1.	0.	1.	0.	0.	0.	0.	0.	0.	0.	0.	0.	0.	0.	0.	0.	0.	0.	0.	0.

Table 8. Gammri+, Gammri- and the catalytic third body efficiency for the 28 reactions and 20 species

14	1.0	14	0.	0.	0.	0.	0.	0.	0.	0.	0.	1.	1.	0.	0.	0.	0.	0.	0.	0.	0.	0.	0.	0.	0.	0.	0.	0.	0.	0.
15	2.0	15	0.	0.	0.	0.	0.	0.	0.	0.	0.	1.	0.	0.	0.	0.	0.	0.	0.	0.	0.	0.	0.	0.	0.	0.	0.	1.	0.	1.
16	2.0	16	0.	0.	0.	0.	0.	0.	0.	0.	0.	1.	0.	0.	0.	0.	0.	0.	0.	0.	0.	0.	0.	0.	0.	0.	0.	0.	0.	2.
17	-0.0	17	0.	0.	0.	0.	0.	0.	0.	0.	1.	0.	0.	0.	0.	0.	0.	0.	0.	0.	0.	0.	0.	0.	0.	0.	0.	0.	0.	0.
18	1.0	18	0.	0.	0.	0.	0.	0.	0.	0.	0.	0.	1.	0.	0.	0.	0.	0.	0.	0.	0.	0.	0.	0.	0.	0.	0.	0.	1.	0.
19	1.0	19	0.	0.	0.	0.	0.	0.	0.	0.	0.	0.	0.	1.	0.	0.	0.	0.	0.	0.	0.	0.	0.	0.	0.	0.	0.	1.	0.	0.
20	2.0	20	0.	0.	0.	0.	0.	0.	0.	0.	0.	0.	0.	0.	0.	2.	0.	0.	0.	0.	0.	0.	0.	0.	0.	0.	0.	1.	0.	0.
21	1.0	21	0.	0.	0.	0.	0.	0.	0.	0.	0.	0.	0.	0.	0.	1.	0.	0.	0.	1.	0.	0.	0.	0.	0.	0.	0.	0.	0.	0.
22	3.0	22	1.	0.	0.	0.	0.	0.	1.	0.	0.	0.	0.	0.	0.	0.	0.	0.	2.	0.	0.	0.	0.	0.	0.	0.	0.	0.	0.	0.
23	3.0	23	0.	0.	0.	0.	0.	0.	0.	0.	0.	0.	0.	0.	0.	1.	0.	0.	2.	0.	0.	0.	0.	0.	0.	0.	0.	1.	0.	0.
24	3.0	24	0.	0.	0.	0.	0.	0.	1.	0.	0.	0.	0.	0.	0.	0.	0.	0.	2.	0.	0.	0.	0.	0.	0.	0.	0.	1.	0.	0.
25	2.0	25	0.	0.	0.	0.	0.	0.	0.	0.	0.	0.	0.	0.	0.	0.	0.	0.	2.	0.	0.	0.	0.	0.	0.	0.	0.	1.	0.	0.
26	1.0	26	0.	0.	0.	0.	0.	0.	0.	0.	0.	0.	0.	0.	0.	0.	0.	0.	1.	1.	0.	0.	0.	0.	0.	0.	0.	0.	0.	0.
27	2.0	27	0.	0.	0.	0.	0.	0.	0.	0.	0.	0.	0.	0.	0.	0.	0.	0.	1.	0.	0.	0.	0.	0.	0.	0.	0.	1.	0.	1.
28	-0.0	28	0.	0.	0.	0.	0.	0.	0.	0.	0.	0.	0.	0.	0.	0.	0.	0.	1.	0.	0.	0.	0.	0.	0.	0.	0.	0.	0.	0.

GAMMPL(28,20)

1	2.	0.	0.	0.	0.	0.	0.	0.	0.	0.	0.	0.	0.	0.	0.	0.	0.	0.	0.	0.
2	0.	0.	0.	2.	0.	0.	0.	0.	0.	0.	0.	0.	0.	0.	0.	0.	0.	0.	0.	0.
3	0.	0.	0.	2.	0.	0.	0.	0.	0.	0.	0.	0.	0.	0.	0.	0.	0.	0.	0.	0.
4	1.	0.	0.	1.	0.	0.	0.	0.	0.	0.	0.	0.	0.	0.	0.	0.	0.	0.	0.	0.
5	0.	1.	0.	1.	0.	0.	0.	0.	0.	0.	0.	0.	0.	0.	0.	0.	0.	0.	0.	0.
6	0.	0.	1.	1.	0.	0.	0.	0.	0.	0.	0.	0.	0.	0.	0.	0.	0.	0.	0.	0.
7	0.	0.	0.	0.	1.	0.	0.	0.	0.	0.	0.	0.	0.	0.	0.	0.	0.	0.	0.	0.
8	0.	0.	2.	0.	0.	0.	0.	0.	0.	0.	0.	0.	0.	0.	0.	0.	0.	0.	0.	0.
9	0.	0.	0.	0.	0.	0.	0.	1.	0.	0.	0.	0.	0.	0.	0.	0.	0.	0.	0.	0.
10	1.	0.	0.	0.	0.	1.	0.	0.	0.	0.	0.	0.	0.	0.	0.	0.	0.	0.	0.	0.
11	1.	0.	0.	0.	0.	1.	0.	0.	0.	0.	0.	0.	0.	0.	0.	0.	0.	0.	0.	0.
12	0.	0.	0.	0.	0.	0.	0.	1.	0.	0.	0.	0.	0.	0.	0.	0.	0.	0.	0.	0.
13	0.	0.	0.	0.	0.	0.	0.	0.	0.	1.	0.	1.	0.	0.	0.	0.	0.	0.	0.	0.
14	0.	0.	0.	0.	0.	0.	0.	0.	0.	1.	1.	0.	0.	0.	0.	0.	0.	0.	0.	0.
15	0.	0.	0.	0.	0.	0.	0.	0.	0.	1.	0.	0.	0.	0.	0.	0.	0.	0.	0.	0.
16	0.	0.	0.	0.	0.	0.	0.	0.	0.	1.	0.	0.	0.	0.	0.	0.	0.	0.	0.	0.
17	0.	0.	0.	0.	0.	0.	0.	0.	1.	0.	0.	0.	0.	0.	0.	0.	0.	0.	0.	0.
18	0.	0.	0.	0.	0.	0.	0.	0.	0.	0.	1.	0.	0.	0.	0.	0.	0.	0.	0.	0.
19	0.	0.	0.	0.	0.	0.	0.	0.	0.	0.	0.	1.	0.	0.	0.	0.	0.	0.	0.	0.
20	0.	0.	0.	0.	0.	0.	0.	0.	0.	0.	0.	0.	0.	2.	0.	0.	0.	0.	0.	0.
21	0.	0.	0.	0.	0.	0.	0.	0.	0.	0.	0.	0.	0.	1.	0.	0.	0.	1.	0.	0.
22	1.	0.	0.	0.	0.	0.	1.	0.	0.	0.	0.	0.	0.	0.	0.	2.	0.	0.	0.	0.
23	0.	0.	0.	0.	0.	0.	0.	0.	0.	0.	0.	0.	0.	1.	0.	2.	0.	0.	0.	0.
24	0.	0.	0.	0.	0.	0.	1.	0.	0.	0.	0.	0.	0.	0.	0.	2.	0.	0.	0.	0.
25	0.	0.	0.	0.	0.	0.	0.	0.	0.	0.	0.	0.	0.	0.	0.	2.	0.	0.	0.	0.
26	0.	0.	0.	0.	0.	0.	0.	0.	0.	0.	0.	0.	0.	0.	0.	1.	1.	0.	0.	0.
27	0.	0.	0.	0.	0.	0.	0.	0.	0.	0.	0.	0.	0.	0.	0.	1.	0.	0.	0.	0.
28	0.	0.	0.	0.	0.	0.	0.	0.	0.	0.	0.	0.	0.	0.	0.	1.	0.	0.	0.	0.

GAMMMI(28,20)

1	0.	1.	0.	0.	0.	0.	0.	0.	0.	0.	0.	0.	0.	0.	0.	0.	0.	0.	0.	0.
2	0.	0.	0.	0.	0.	0.	0.	0.	0.	0.	0.	0.	0.	0.	0.	0.	0.	0.	0.	1.
3	0.	0.	0.	0.	0.	0.	0.	0.	0.	0.	0.	0.	0.	0.	0.	0.	0.	0.	0.	1.
4	0.	0.	1.	0.	0.	0.	0.	0.	0.	0.	0.	0.	0.	0.	0.	0.	0.	0.	0.	0.

5	1.	0.	1.	0.	0.	0.	0.	0.	0.	0.	0.	0.	0.	0.	0.	0.	0.	0.	0.	0.
6	1.	0.	0.	0.	0.	0.	0.	0.	0.	0.	0.	0.	0.	0.	0.	0.	0.	0.	0.	1.
7	1.	0.	0.	1.	0.	0.	0.	0.	0.	0.	0.	0.	0.	0.	0.	0.	0.	0.	0.	0.
8	0.	1.	0.	0.	0.	0.	0.	0.	0.	0.	0.	0.	0.	0.	0.	0.	0.	0.	0.	1.
9	1.	0.	0.	0.	0.	0.	1.	0.	0.	0.	0.	0.	0.	0.	0.	0.	0.	0.	0.	0.
10	0.	0.	0.	0.	0.	0.	1.	0.	0.	0.	0.	0.	0.	0.	0.	0.	0.	0.	0.	0.
11	0.	0.	0.	0.	0.	0.	1.	0.	0.	0.	0.	0.	0.	0.	0.	0.	0.	0.	0.	0.
12	1.	0.	0.	0.	0.	0.	1.	0.	0.	0.	0.	0.	0.	0.	0.	0.	0.	0.	0.	0.
13	0.	1.	0.	0.	0.	0.	0.	0.	1.	0.	0.	0.	0.	0.	0.	0.	0.	0.	0.	0.
14	1.	0.	0.	0.	0.	0.	0.	0.	1.	0.	0.	0.	0.	0.	0.	0.	0.	0.	0.	0.
15	0.	0.	0.	0.	0.	0.	0.	0.	1.	0.	0.	0.	0.	0.	0.	0.	0.	0.	0.	0.
16	0.	0.	0.	0.	0.	0.	0.	0.	1.	0.	0.	0.	0.	0.	0.	0.	0.	0.	0.	0.
17	0.	0.	0.	0.	0.	0.	0.	0.	0.	1.	0.	0.	0.	0.	0.	0.	0.	0.	0.	0.
18	1.	0.	0.	0.	0.	0.	0.	0.	0.	0.	0.	0.	0.	0.	0.	0.	0.	0.	0.	0.
19	0.	1.	0.	0.	0.	0.	0.	0.	0.	0.	0.	0.	0.	0.	0.	0.	0.	0.	0.	0.
20	0.	0.	0.	0.	0.	0.	0.	0.	0.	0.	0.	0.	0.	0.	0.	0.	0.	0.	1.	0.
21	1.	0.	0.	0.	0.	0.	0.	0.	0.	0.	0.	0.	0.	0.	0.	0.	0.	0.	1.	0.
22	0.	1.	0.	0.	0.	0.	0.	0.	0.	0.	0.	0.	0.	1.	0.	0.	0.	0.	0.	0.
23	0.	0.	0.	0.	0.	0.	0.	0.	0.	0.	0.	0.	1.	0.	0.	0.	0.	0.	0.	0.
24	0.	0.	0.	0.	0.	0.	0.	0.	0.	0.	0.	0.	0.	0.	0.	0.	1.	0.	0.	0.
25	0.	0.	0.	0.	0.	0.	0.	0.	0.	0.	0.	0.	0.	0.	1.	0.	0.	0.	0.	0.
26	0.	0.	0.	0.	0.	0.	0.	0.	0.	0.	0.	0.	0.	0.	1.	0.	0.	0.	0.	0.
27	0.	0.	0.	0.	0.	0.	0.	0.	0.	0.	0.	0.	0.	0.	0.	1.	0.	0.	0.	0.
28	0.	0.	0.	0.	0.	0.	0.	0.	0.	0.	0.	0.	0.	0.	0.	1.	0.	0.	0.	0.

Catalytic Third Body Matrics Relative to Argon

ZSUB(8,20)

	O	O2	NO	N	NOP	C	CO	CO2	NA	NAP	OM	O2M	CF4	CF2	F2	F	FM	COF2	C2F4	N2
M1	25.0	9.0	1.0	1.0	0.0	0.0	2.0	5.0	0.0	0.0	0.0	0.0	5.0	5.0	5.0	2.0	0.0	1.0	5.0	2.0
M2	1.0	1.0	1.0	0.0	0.0	0.0	2.0	5.0	0.0	0.0	0.0	0.0	5.0	5.0	5.0	2.0	0.0	1.0	5.0	2.5
M3	20.0	1.0	20.0	20.0	0.0	0.0	2.0	5.0	0.0	0.0	0.0	0.0	5.0	5.0	5.0	2.0	0.0	1.0	5.0	1.0
M4	2.0	2.0	2.0	2.0	0.0	0.0	2.0	5.0	0.0	0.0	0.0	0.0	5.0	5.0	5.0	2.0	0.0	1.0	5.0	2.0
M5	0.0	0.0	0.0	0.0	0.0	0.0	2.0	0.0	0.0	0.0	0.0	0.0	0.0	0.0	0.0	0.0	0.0	0.0	0.0	0.0
M6	1.0	2.0	2.0	1.0	0.0	0.0	2.0	5.0	0.0	0.0	0.0	0.0	5.0	5.0	5.0	2.0	0.0	1.0	5.0	2.0
M7	0.0	25.0	0.0	0.0	0.0	0.0	0.0	0.0	0.0	0.0	0.0	0.0	5.0	5.0	5.0	2.0	0.0	1.0	5.0	1.0
EL	0.0	0.0	0.0	0.0	1.0	0.0	0.0	0.0	0.0	1.0	-1.0	-1.0	0.0	0.0	0.0	0.0	-1.0	0.0	0.0	0.0

Table 9. Axial force coefficient (CA) comparison

Case A	CAP	CAF	CA	Remarks
$\dot{m} = 0$	0.04158	0.00718	0.048763	
$\dot{m} \neq 0$	0.04242	0.00336	0.045784	air injection
	0.04178	0.00409	0.045875	teflon injection

Case B	CAP	CAF	CA	Remarks
$\dot{m} = 0$	0.10692	0.02320	0.130125	
$\dot{m} \neq 0$	0.10905	0.01118	0.120233	air injection
	0.10804	0.01272	0.126754	teflon injection

Table 10. Heat-transfer rate comparison at 125 kft altitude

125 kft altitude at s/Rn = 19.7 and 52.3

at s/Rn = 19.7

Case	QW_{con}	QW_{diff}	QW_{conv}	QW_{tot}
$\dot{m} = 0$	-28.7023	-19.3357	0.0	-48.0381
$\dot{m} \neq 0$				
air	-13.6868	-11.0614	0.0	-24.7482
teflon	-13.5047	-29.7088	+ 1.7879	-41.4256

at s/Rn = 52.3

Case	QW_{cond}	QW_{diff}	QW_{conv}	QW_{tot}
$\dot{m} = 0$	-27.9447	-12.2669	0.0	-40.2116
$\dot{m} \neq 0$				
air	-11.46	-6.9021	0.0	-18.3621
teflon	-12.0	-21.2829	+ 1.2573	-32.0256

Btu/ft²/ sec

Table 11. Concentration gradient and enthalpy of major species at the wall

Specie	$\frac{\partial C_i}{\partial \eta_w}$	$\frac{H_i}{H_{ref}}$	$\frac{\partial C_i}{\partial \eta_w}\frac{H_i}{H_{ref}}$
O	2.1369	0.36005	0.76939
N_2	42.3168	0.023160	0.98006
CO	-34.257	-0.06389	2.1887
CO_2	-0.92	-0.17106	0.15737
CF_4	-30.99	-0.20597	6.3830
COF_2	-1.0495	-0.18721	0.19648

where $H_{ref} = 0.50176 \times 10^9 \ (\frac{ft^2}{sec^2})$

Table 12. Computing times

Case A

Method	CPU time	time ratio	per grid point
$\dot{m} = 0$	1:35	1.0	0.0380 sec
$\dot{m} \neq 0$			
air	2:02	1.28	0.0488 sec
teflon	33:53	21.4	0.8135 sec

Case B

Method	CPU time	time ratio	per grid point
$\dot{m} = 0$	0:53	1.0	0.0306 sec
$\dot{m} \neq 0$			
air	1:18	1.47	0.0450 sec
teflon	9:44	11.0	0.3368 sec

Appendix A. Derivation of the Species Boundary Conditions

The wall species boundary conditions can be obtained by solving the binary mixture species conservation equations. Since we do not know the exact equilibrium wall species concentration a priori, the freestream species concentration at the wall which can be used as an initial composition at the wall would be very important. Once we know the freestream species concentration at the wall, the equilibrium species concentration can be obtained from the Gibbs free energy minimization technique, to which we provide the fuel-air weight ratio.

Adams et al. (1970), who treated the injection of a foreign gas into the boundary layer, used the fact that in a steady state the net mass flux of the freestream species must be zero at the porous body surface rather than the boundary conditions that Jaffe et al.(1967) used in their study, where Jaffe et al. (1967) used the assumption that the concentration of the freestream species should be zero.

Since teflon and air (we will call air freestream species hereafter) are considered as two binary species in equilibrium in deriving the surface boundary conditions, we can obtain the concentration of air at the wall by solving the species conservation equation with proper boundary conditions. The proper boundary condition, as discussed by Baron (1960), may be expressed as

$$\dot{m}_{fw} = -\rho_w D_w (\frac{\partial C_f}{\partial y})_w + \rho_w v_w C_{fw} = 0 \qquad (A.1)$$

or

$$C_{f_w} = (\frac{D}{\nu} \frac{\partial C_f}{\partial y})_w \qquad (A.2)$$

A schematic drawing of the surface mass transfer and diffusion phenomena is shown in Fig. 5a.

Consider the boundary conditions for the species equations at the gas-solid interface. The freestream species f are transported away from the surface at the rate $\overline{\rho v} C_f$ by convection and J_f by diffusion. At the same time, the species f are being convected into the surface at the rate $(\overline{\rho v} C_f)_-$ This flux may be considered from an ablating surface or the injectant from a porous surface. The surface freestream species concentrations are given by

$$\overline{\rho v} C_f + \varepsilon^2 J_i = (\overline{\rho v} C_f)_- \qquad (A.3)$$

Since

$$\overline{\rho v} = (\overline{\rho v})_- = \dot{m}. \qquad (A.4)$$

Equation (A.3) can be written as

$$(C_f - C_{f-})\dot{m} = -\varepsilon^2 J_f \qquad (A.5)$$

However, from the body to the surface there is no initial injection of freestream air, thus C_{f-} should be zero.

Nondimensionalizing by reference variables and normalizing by the quantities behind the shock except for the normal velocity and temperature, we obtain the following equation as a boundary condition for a binary mixture consisting of freestream and injectant.

$$\frac{\partial C_f}{\partial \eta} + \frac{\dot{m} n_{sh} \mathrm{Pr}}{\varepsilon^2 \mu_{sh} \overline{\mu} \mathrm{Le}} C_f = 0 \qquad (A.6)$$

For the binary mixture, the freestream species concentration can be obtained by solving the species conservation equation, which is different from other species concentration equations in the sense that there is no production term. Therefore, the species conservation equation for binary species can be written as

$$\frac{DC_f}{Dt} = -\nabla \cdot J_f \tag{A.7}$$

which can be rewritten in body normal coordinates and nondimensionalized by the reference quantities

$$\frac{\rho u}{h_1}\frac{\partial C_f}{\partial s} + \rho v\frac{\partial C_f}{\partial n} + \frac{\rho w}{h_3}\frac{\partial C_f}{\partial \varphi} = \frac{\varepsilon^2}{h_1 h_3}\frac{\partial}{\partial n}\left[\frac{\mu \mathrm{Le}_f h_1 h_3}{\mathrm{Pr}}\frac{\partial C_f}{\partial n}\right] \tag{A.8}$$

normalizing Equation (A.8) by the quantities behind the bow shock such as, $\xi = s, \eta = \frac{n}{n_{sh}}, \zeta = \varphi, \bar{u} = \frac{u}{u_{sh}}, \bar{\rho} = \frac{\rho}{\rho_{sh}}, \bar{p} = \frac{p}{p_{sh}}, \bar{\mu} = \frac{\mu}{\mu_{sh}}, \bar{k} = \frac{k}{k_{sh}}$, etc. Then the species conservation equation for the binary species becomes, without production term in standard parabolic partial differential equation,

$$A_0\frac{\partial^2 W}{\partial \eta^2} + A_1\frac{\partial W}{\partial \eta} + A_2 W + A_3 + A_4\frac{\partial W}{\partial \xi} + A_5\frac{\partial W}{\partial \zeta} = 0 \tag{A.9}$$

where

$$A_0 = \frac{\varepsilon^2}{n_{sh}^2}\frac{\mu_{sh}\bar{\mu}\mathrm{Le}}{\mathrm{Pr}} \tag{A.10}$$

$$A_1 = \frac{\varepsilon^2}{n_{sh}^2}\frac{\partial}{\partial \eta}\left(\frac{\mu_{sh}\bar{\mu}\mathrm{Le}}{\mathrm{Pr}}\right) + \frac{\varepsilon^2}{n_{sh}^2}\frac{\mu_{sh}\bar{\mu}\mathrm{Le}}{h_1\mathrm{Pr}}\frac{\partial h_1}{\partial \eta} + \frac{\varepsilon^2}{n_{sh}^2}\frac{\mu_{sh}\bar{\mu}}{h_3}\frac{\mathrm{Le}}{\mathrm{Pr}}\frac{\partial h_3}{\partial \eta}$$

$$+ \frac{\bar{\rho}\rho_{sh}\bar{u}u_{sh}}{h_1}\frac{\eta}{n_{sh}}\frac{\partial n_{sh}}{\partial \xi} + \frac{\bar{\rho}\rho_{sh}}{h_3}\frac{\eta}{n_{sh}}\frac{\partial n_{sh}}{\partial \zeta} - \frac{\bar{\rho}\rho_{sh}v}{n_{sh}}$$

$$A_2 = 0.0$$

$$A_3 = 0.0$$

$$A_4 = -\frac{\bar{\rho}\rho_{sh}\bar{u}u_{sh}}{h_1}$$

$$A_5 = -\frac{\bar{\rho}\rho_{sh}w}{h_3}$$

where

$$W = C_f$$

By substituting the following finite-difference expressions

$$\frac{\partial^2 W}{\partial \eta^2} = \frac{2\left[W_{2,j+1} - (1+k)W_{2,j} + kW_{2,j-1}\right]}{(\eta_{j+1} - \eta_j)^2 + k(\eta_j - \eta_{j-1})^2} \qquad (A.11)$$

$$\frac{\partial W}{\partial \eta} = \frac{W_{2,j+1} - (1-k)^2 W_{2,j} - k^2 W_{2,j-1}}{(\eta_{j+1} - \eta_j) + k^2(\eta_j - \eta_{j-1})}$$

$$W = W_{2,j}$$

$$\frac{\partial W}{\partial \xi} = \frac{W_{2,j} - W_{3,j}}{\Delta \xi}$$

$$\frac{\partial W}{\partial \zeta} = \frac{(W_{4,j} - W_{3,j}) + (W_{2,j} - W_{1,j})}{2\Delta \xi}$$

where

$$k = \frac{(\eta_{j+1} - \eta_j)}{(\eta_j - \eta_{j-1})}$$

First subscript 2 of $W_{2,j}$ denotes the current ξ -station and 3 of $W_{3,j}$ denotes the previous ξ -station.

A finite-difference form is obtained from the substitution of above expressions into the parabolic partial difference equation.

$$\bar{A}_j W_{2,j-1} + \bar{B}_j W_{2,j} + \bar{C}_j W_{2,j+1} = \bar{D}_j \qquad (A.12)$$

And the general solution of this tridigonal equation can be expressed as

$$W_{2,j} = E_j W_{2,j+1} + F_j \qquad (A.13)$$

where

$$E_j = \frac{\bar{C}_j}{(\bar{A}_j E_{j-1} + \bar{B}_j)}$$

$$F_j = \frac{(\bar{D}_j - \bar{A}_j F_{j-1})}{(\bar{A}_j E_{j-1} + \bar{B}_j)}$$

The binary species wall boundary condition can be written in the finite-difference form to second-order accuracy with nonconstant(variable) mesh as follows:

$$(\frac{\partial C_f}{\partial \eta})_w = \frac{\Delta\eta_1}{\Delta\eta_2(\Delta\eta_2 - \Delta\eta_1)}\{(\frac{\Delta\eta_2}{\Delta\eta_1})^2 C_{f,2} - C_{f,3} - ((\frac{\Delta\eta_2}{\Delta\eta_1})^2 - 1)C_{f,1}\} \qquad (A.14)$$

$$- \frac{\bar{\rho}\rho_{sh} v n_{sh} \mathrm{Pr}}{\varepsilon^2 \mu_{sh} \bar{\mu} \mathrm{Le}} C_{f,1} = 0$$

where

$$\Delta\eta_2 = \eta_3 - \eta_1$$

and

$$\Delta\eta_1 = \eta_2 - \eta_1$$

By rearrangement, the boundary condition can be written as

$$C_{f,1} = GC_{f,2} + HC_{f,3} \tag{A.15}$$

where

$$G = \frac{(\frac{\Delta\eta_2}{\Delta\eta_1})^2}{\{\frac{\Delta\eta_2(\Delta\eta_2 - \Delta\eta_1)}{\varepsilon^2\Delta\eta_1}\frac{\bar{\rho}\rho_{sh}\nu n_{sh}\mathrm{Pr}}{\mu_{sh}\bar{\mu}\mathrm{Le}} + (\frac{\Delta\eta_2}{\Delta\eta_1})^2 - 1\}}$$

and

$$H = -\frac{1}{\{\frac{\Delta\eta_2(\Delta\eta_2 - \Delta\eta_1)}{\varepsilon^2\Delta\eta_1}\frac{\bar{\rho}\rho_{sh}\nu n_{sh}\mathrm{Pr}}{\mu_{sh}\bar{\mu}\mathrm{Le}} + (\frac{\Delta\eta_2}{\Delta\eta_1})^2 - 1\}}$$

Then the first set of Eq.(A.12) including the binary mixture boundary condition that no net freestream mass flux through the surface becomes (From now on W_1 represents $W_{2,1}$, W_2 does $W_{2,2}$,etc.),

$$\tilde{A}_2 W_1 + \tilde{B}_2 W_2 + \tilde{C}_2 W_3 = \tilde{D}_2 \tag{A.16}$$

When we substitute Eq. (A.15) into Eq.(A.16), Eq.(A.16) becomes

$$\bar{B}_2 W_2 + \bar{C}_2 W_3 = \tilde{D}_2 \tag{A.17}$$

where

$$\bar{B}_2 = \tilde{A}_2 G + \tilde{B}_2,$$

$$\bar{C}_2 = \tilde{A}_2 H + \tilde{C}_2.$$

Then again the above equation gives a tridigonal system written as

$$\begin{bmatrix} \bar{B}_2 & \bar{C}_2 & 0 & 0 & 0 \\ \tilde{A}_3 & \tilde{B}_3 & \tilde{C}_3 & 0 & 0 \\ 0 & \tilde{A}_4 & \tilde{B}_4 & \tilde{C}_4 & 0 \\ \cdot & \cdot & \cdot & \cdot & \cdot \\ 0 & 0 & 0 & \tilde{A}_{nj-1} & \tilde{B}_{nj-1} \end{bmatrix} \begin{Bmatrix} W_2 \\ W_3 \\ W_4 \\ \cdot \\ W_{nj-1} \end{Bmatrix} = \begin{Bmatrix} \tilde{D}_2 \\ \tilde{D}_3 \\ \tilde{D}_4 \\ \cdot \\ \bar{D}_{nj-1} \end{Bmatrix} \tag{A.18}$$

where $\bar{D}_{nj-1} = D_{nj-1} - C_{nj-1}W_{nj}$

And W_2 may be expressed by using W_3

$$W_2 = E_2 W_3 + F_2 \tag{A.19}$$

where

$$E_2 = -\frac{\bar{C}_2}{\bar{B}_2},$$

$$F_2 = \frac{\tilde{D}_2}{\bar{B}_2}.$$

From the shock boundary condition, the freestream species concentration is one, which can be expressed as $W_{nj} = 1.0$. By back substitution we can obtain $W_{nj-1}, \ldots, W_2$.

Then W_1 can be obtained from Eq.(A.15). By using the C_{fw}, we can obtain the fuel-air mixture weight ratio as follows:

$$\begin{aligned} C_{C_2F_4} &= \frac{\text{Weight of fuel}}{\text{Weight of fuel and air}} \\ &= (1.0 - C_{fw}) \end{aligned} \tag{A.20}$$

With $C_{C_2F_4}$ and P_w known, the equilibrium species concentration can be interpolated from the table obtained from the Gordon and McBride code.

Appendix B. Transport Property Calculations

The transport property data of CF_2, CF_4, CO_2, F, F_2, *and* Na have been obtained from the theory of Chapman (1939) and Enskog. The important assumptions in the development are

1. the gas is sufficiently dilute so that only binary collisions occur,

2. the motion of the molecules during a collision can be described by classical mechanics,

3. only elastic collisions occur, and

4. the intermolecular forces act only between fixed centers of the molecules, i.e., the intermolecular potential function is spherically symmetric.

With these restrictions, it would appear that the theory should be applicable to low-pressure, high temperature nonatomic gases. But it is often applied to polyatomic gases under the pressure and temperature restrictions, since no alternative models are known to exist.

The Chapman-Enskog theory considers the interaction between colliding molecules with a potential energy $\psi(r)$ in detail. The equations are well known, but their solution is often very difficult. In general the viscosity can be written as

$$\eta = \frac{\frac{5}{16}(\pi MRT)^{\frac{1}{2}}}{(\pi\sigma^2)\Omega_v} = 26.69\frac{\sqrt{MT}}{(\sigma^2\Omega_v)}\mu P \qquad (B.1)$$

while the viscosity expression for a rigid, noninteracting sphere model is $\eta = 26.69\frac{\sqrt{MT}}{\sigma^2}$ where σ is a mean diameter of non-interacting rigid spheres. Given a potential energy of interaction, $\psi(r)$, Ω_v can be calculated by using the results, for example, from the Lennard-Jones or Stockmayer potential functions.

Nonpolar gases

The Lennard-Jones 12-6 potential is

$$\psi(r) = 4\varepsilon\left[\left(\frac{\sigma}{r}\right)^{12} - \left(\frac{\sigma}{r}\right)^{6}\right] \qquad (B.2)$$

Figure 19 shows the schematic drawing for Lennard-Jones 12-6 potential, which chiefly assumes the following

First, a spherically symmetric potential is assumed, but this is strictly true only for the atoms.

Second, the repulsive term in the potential is assigned an exponent of 12. This is only an approximation used for mathematical simplicity. (Actual range from about to 15 for many molecules). The harder the molecule, the larger the exponent.

Third, only a single potential energy curve is assumed for a given interaction.

The effect of excited states was not considered, and this is a possible source of error in very high temperature.

Such a relation is based on a rather tenuous theoretical background and has been widely criticized. However, it is probably one of the more tractable relations for $\psi(r)$, since Ω_v is relatively insensitive to the exact form of the $\psi(r)$ expression.

Neufeld et al. (1970) proposed an empirical relation which can be convenient for computer application:

$$\Omega_v = \left(\frac{A}{T^{*B}}\right) + \frac{C}{\exp(DT^*)} + \frac{E}{\exp(FT^*)} \qquad (B.3)$$

where

$$T^* = \frac{kT}{\varepsilon},\ A = 1.16145,\ B = 0.14874,\ C = 0.52487,$$

$$D = 0.77320,\ E = 2.16178,\ F = 2.43787$$

The above equation is applicable from $0.3 \leq T^* \leq 100$. Relevant constants for CF_2, CF_4, CO_2, F, F_2, and Na can be found in Table 7. The constants for C_2F_4 can be obtained from the following expression,

$$\sigma\left(\frac{P_c}{T_c}\right)^{\frac{1}{3}} = 2.3551 - 0.087\omega \qquad (B.4)$$

and

$$\frac{\varepsilon}{kT_c} = 0.7915 + 0.1693\omega \qquad (B.5)$$

where ω = accentric factor,

σ = potential length constant in Å,

P_c = critical pressure in atm.,

T_c = critical temperature in degree K,

ε = potential energy constant, ergs,

k = Boltzmann's constant = 1.3805 ergs / K

For C_2F_4, T_c = 306.4 K , P_c = 38.9, ω = 0.226, M = 100.016. Thus σ = 4.64656Å, $\frac{\varepsilon}{k}$ = 254.239K. By using these values in Eq. (B.3) we can obtain Ω_v , finally we can obtain viscosity from equation (B.1).

Appendix C. Mass-Transfer Distributions Calculation

C.1 Cold Wall Heat Transfer

The cold wall heat-transfer rate is required for the solution to the steady-state iteration for T_w and $\dot{m}_T$ for surface material ablation. The heat-transfer coefficient with no blowing (C_{H_0}) can be obtained from the cold wall heat-transfer rate. Currently the Fay-Riddell (1958) method is used to compute the stagnation heat-transfer rate for laminar boundary layer flow, and Lee's theory (1958) has been used to compute downstream of the stagnation point.

The Fay-Riddell equation for stagnation point heat-transfer rate calculation can be expressed as

$$\dot{q}_w = 0.763Pr^{-0.6}(\rho_e\mu_e\frac{dU_e}{ds}|_0)^{0.5}\left[\frac{\rho_w\mu_w}{\rho_e\mu_e}\right]^{0.1}(h_e - h_w) \qquad (C.1)$$

The stagnation properties are calculated by using simple normal shock crossing conditions as follows where we denote 1 as condition before the shock, 2 as condition after the shock and 0 as stagnation property.

$$T_{01} = T_1(1 + \frac{\gamma - 1}{2} M_\infty^2) \tag{C.2}$$

$$P_{01} = P_1(1 + \frac{\gamma - 1}{2} M_\infty^2)^{\frac{\gamma}{\gamma - 1}}$$

$$T_{01} = T_{02}$$

$$P_{02} = P_1(\frac{\gamma + 1}{2}) M_\infty^2 (\frac{\frac{\gamma + 1}{2} M_\infty^2}{\frac{2\gamma}{\gamma + 1} M_\infty^2 - \frac{\gamma - 1}{\gamma + 1}})^{\frac{1}{\gamma - 1}}$$

The edge properties of the boundary-layer can be obtained as follows. An inviscid finite-difference solution(NOL3D)(Solomon, 1977) which provides the inviscid wall pressure along the body axis is obtained initially for the body geometry and freestream conditions externally from the NOL3D code. The inviscid wall pressure from the inviscid code is used as the boundary layer edge pressure and is assumed constant through the layer. Using the normal shock entropy, the conditions at the boundary-layer edge can be easily obtained through isentropic expansion to the local pressure by using following relations

$$\rho_e = \rho_{02}(\frac{P_e}{P_{02}})^{\frac{1}{\gamma}} \tag{C.3}$$

$$h_e = \frac{\gamma}{\gamma - 1} \frac{P_e}{\rho_e}$$

$$T_e = T_{02}(\frac{P_e}{P_{02}})^{\frac{\gamma - 1}{\gamma}}$$

Cold wall heat-transfer coefficient C_{H_0} can be expressed as $\frac{q_{\dot{w}}}{H_{e_{stag}}}$ which varies along the body. Lees' method has been used downstream of the stagnation point, which can be written as

$$\frac{\dot{q}_w}{\dot{q}_{w_{s=0}}} = \frac{F(s)}{\left[\frac{2}{U_\infty}\frac{dU_e}{ds}|_0\right]^{0.5}} \tag{C.4}$$

where

$$F(s) = \frac{\frac{P_e}{P_0}\frac{\omega_e}{(\omega_e)_0}\frac{r}{\sqrt{2}}\frac{U_e}{U_\infty}}{\left[\int_0^s \frac{P_e}{P_0}\frac{U_e}{U_\infty}\frac{\omega_e}{(\omega_e)_0}r^2 ds\right]^{0.5}}$$

and

$$\omega_e = \frac{\mu_e}{R_e T_e}$$

For the nose ablation material(usually carbon), the wall temperature and mass-transfer distributions can be obtained from the correlation between the convective heat-transfer coefficient and the mass-transfer rate. The details of the relation can be found in the work of Thompson (1983).

The surface ablation model for teflon is empirical, based on the heat of ablation concept as given by Brant (1970) has the form

$$\dot{m}_T = \frac{C_{H_0}}{0.4594 - 0.0027P_e} \tag{C.5}$$

where the ablation temperature of teflon is set to 1800 R, and units of P_e are atmospheres.

Appendix D. Treatment of Production Terms in Species and Energy Equations

The stoichiometric relations for a multicomponent gas with NS distinct chemical species and NR simultaneous chemical reactions can be expressed as

$$\sum_{i=1}^{NJ} \alpha_{ri} X_i \underset{k_{br}}{\overset{k_{fr}}{=}} \sum_{i=1}^{NJ} \beta_{ri} X_i \quad r = 1, \ldots, NR \tag{D.1}$$

The quantities X_i represent the chemical species and catalytic bodies and α_{ri}, β_{ri} are the stoichiometric coefficients of the reaction r. Thus the summation limit NJ is equal to the number of species NS plus the number of catalytic bodies NZ.

The rates at which the forward and backward reactions occur are specified by the forward and backward rate constants which can be expressed by the equations

$$k_{f_r} = T_k^{C_{2_r}} \, e^{(C_{0_r} - \frac{C_{1_r}}{T_k})} \tag{D.2}$$

and

$$k_{b_r} = T_k^{D_{2_r}} \, e^{(D_{0_r} - \frac{D_{1_r}}{T_k})}$$

The net mass rate of production of species i during chemical reaction per unit volume $\dot{w}_i$ is written as

$$\frac{\dot{w}_i}{\rho} = M_i \sum_{r=1}^{NJ} (\beta_{ri} - \alpha_{ri})(L_{f_r} - L_{b_r}) \qquad (D.3)$$

where

$$\alpha_r = \sum_{j=1}^{NJ} \alpha_{rj} - 1$$

$$\beta_r = \sum_{j=1}^{NJ} \beta_{rj} - 1$$

$$L_{f_r} = k_{f_r} \overline{\rho}^{\alpha_r} \prod_{j=1}^{NJ} (\gamma_j)^{\alpha_{rj}}$$

$$L_{b_r} = k_{b_r} \overline{\rho}^{\beta_r} \prod_{j=1}^{NJ} (\gamma_j)^{\beta_{rj}}$$

$$\overline{\rho}(gm/cm^3) = 0.51536\rho(slug/ft^3)$$

For the NS species, the molar concentrations γ_j, are given by the expressions $\gamma_j = \frac{C_j}{M_j}$, for the catalytic third bodies the γ_j are given by the following expression

$$\gamma_j = \sum_{i=1}^{NS} Z_{(j-NS),i} \, \gamma_i, \qquad j = (NS + 1, \ldots, NJ) \qquad (D.4)$$

where $Z_{(j-NS),i}$ is the catalytic third body efficiency relative to argon and determined from the reaction being considered.

Since we are not solving the conservation equation for the electron, the molar amount of electrons is determined from the last catalytic third body efficiency matrix.

The production term can be rewritten so that the species concentration appears as one of the unknowns, and the rate of production terms are given by the expression

$$\frac{\dot{w}_i}{\rho} = \dot{w}_i^0 - \dot{w}_i^1 C_i \qquad (D.5)$$

where

$$\dot{w}_i^0 = M_i \sum_{r=1}^{NR} (\Gamma_{ri}^+ L_{f_r} + \Gamma_{ri}^- L_{b_r})$$

$$\dot{w}_i^1 = \sum_{r=1}^{NR} [\Gamma_{ri}^+ (\frac{L_{b_r}}{\gamma_i}) + \Gamma_{ri}^- (\frac{L_{b_r}}{\gamma_i})]$$

$$\Gamma_{ri}^+ = (\beta_{ri} - \alpha_{ri}) \quad if(\beta_{ri} - \alpha_{ri}) > 0$$
$$= 0 \quad if(\beta_{ri} - \alpha_{ri}) \leq 0$$

$$\Gamma_{ri}^- = (\beta_{ri} - \alpha_{ri}) \quad if(\beta_{ri} - \alpha_{ri}) < 0$$
$$= 0 \quad if(\beta_{ri} - \alpha_{ri}) \geq 0$$

Γ_{ri}^+ and Γ_{ri}^- for the whole reactions and the species are provided in Table 8. It should be mentioned that $\dot{w}_i^0$ and $\dot{w}_i^1$ are positive quantities, and $\dot{w}_i^0$ is not a function of the mass fraction C_i; however $\dot{w}_i^1$ can be a function of C_i.

For the energy equation, the production term is written so that the temperature appears as an unknown as given by Davis (1970a) as

$$\left(\frac{\dot{w}_i}{\rho}\right)_{k+1} = \left(\frac{\dot{w}_i}{\rho}\right)_k + \left[\frac{\partial}{\partial T}\left(\frac{\dot{w}_i}{\rho}\right)\right]_k [T_{k+1} - T_k] \qquad (D.6)$$

where k denotes the iteration for which the solution is known and $k + 1$ the iteration for which the solution is sought. Accordingly the production term in the energy equation was rewritten as

$$\sum_{i=1}^{NS} h_i \dot{w}_i = \dot{w}_1 + T\dot{w}_2 \qquad (D.7)$$

and the terms $\dot{w}_1$ and $\dot{w}_2$ appear in the energy equation coefficients.

In the above equation, form for the rate of production term was a function of the derivative of $\frac{\dot{w}_i}{\rho}$ with respect to T. With temperature in degrees Kelvin T_k the expression for the derivative is

$$\frac{\partial}{\partial T_k}\left(\frac{\dot{w}_i}{\rho}\right) = \frac{M_i}{T_k}\sum_{r=1}^{NR}(\beta_{ri} - \alpha_{ri})[(C_{2_r} + \frac{C_{1_r}}{T_k} - \alpha_r)L_{f_r} - (D_{2_r} + \frac{D_{1_r}}{T_k} - \beta_r)L_{b_r}] \quad (D.8)$$

This equation is solved at each iteration rather than for the whole production term. This process has been known to reduce the stability problem in solving the production terms.

The vita has been removed from the scanned document